MODELING SYSTEMATIC ERRORS AND IMPROVING COMPUTATION EFFICIENCY IN GNSS POSITIONING

YU WENKUN

PhD

The Hong Kong Polytechnic University

2019

The Hong Kong Polytechnic University

Department of Land Surveying & Geo-informatics

Modeling Systematic Errors and Improving Computation Efficiency in GNSS Positioning

YU Wenkun

A thesis submitted in partial fulfillment of the requirements for the degree of Doctor of Philosophy

January 2019

CERTIFICATE OF ORIGINALITY

I hereby declare that this thesis is my own work and that, to the best of my knowledge and belief, it reproduces no material previously published or written, nor material that has been accepted for the award of any other degree or diploma, except where due acknowledgement has been made in the text.

_____ (Signed)

YU Wenkun (Name of student)

Abstract

The emergence of multiple Global Navigation Satellite Systems (GNSSs) improves the observation redundancy and positioning accuracy, especially in areas where sky views are restricted. However, joint use of multi-GNSS observations also brings challenges to data processing due to the extra biases, systematic errors, heteroscedastic error structures, more frequent multiple-outliers and higher computational resources required. This study focuses on four aspects of multi-GNSS positioning. First, the advantages of using multi-GNSS observations in positioning are investigated. It is shown that compared with GPS-only solutions the total number of satellites in the case of the current multiple GNSS constellations increases by 280% and the position dilution of precision (PDOP) reduces by 52.4%. The improvements of the satellite number and PDOP will further rise to 340% and 57.1% respectively when all the satellite systems reach their full constellations. It is especially advantageous to use multiple GNSSs for positioning in difficult observational environments with significant blockage of satellite signals. The real-data static relative positioning test shows that the positioning error decreases by up to 52.4% when using the current quad-constellations (i.e. GPS, GLONASS, BeiDou, and Galileo). Simulation experiments show that when all four systems reach their full constellations the positioning accuracy can improve by 48.5–69.0%.

Second, a new positioning model is developed to account for systematic errors in multi-GNSS positioning. Unmodeled systematic errors, such as multipath effects and residual atmospheric delays, can impact on the estimated positions and the variance components. A semiparametric estimation model is developed for better mitigation of the systematic errors. Test results with simulated systematic errors show that systematic errors can be accurately estimated with the proposed approach. A test with three-day real GNSS observations from a short baseline demonstrates that, compared with standard least-squares estimation, when combined with variance component estimation the proposed method can improve the accuracy of the estimated static baseline by 35.6%. A simplified procedure based on least-squares residuals is

proposed to enhance the determination of smoothing parameters, which has been proved practical and effective. Experimental results indicate that the proposed approach is about 100 times faster than the traditional generalized cross-validation-based method.

Third, a new model based on the mixed use of time-differenced and undifferenced carrier phase observations is developed for kinematic multi-GNSS precise point positioning (PPP). The approach can reduce the number of constant parameters to be estimated and effectively mitigates systematic errors. Test results show that when an accurate initial position is available the proposed approach can attain up to 71% improvement in positioning accuracy compared to the traditional PPP.

Four, a two-step positioning approach is proposed whereby a subset of observations considered to be of high quality is first selected to estimate an initial position. The derived initial position is then used to remove outliers and ambiguities in the rest of the observations. All the available observations can be processed together after the removal of outliers and ambiguities to strengthen and refine the positioning. Experimental results show that the new approach outperforms the traditional multiple GNSSs approach by 4.8% and 21.4% in standard point positioning and static relative positioning respectively. The two-step method has a higher efficiency compared with the traditional method, the computation time can be reduced by 40.4% and 27.7% respectively in standard point positioning and static relative positioning.

The research results contribute to an improved understanding of the impacts of systematic errors in multi-GNSS positioning, and enhancing the accuracy, reliability, and efficiency in such positioning applications. The study can be extended to long-term and high-rate positioning applications, such as deformation monitoring and un-manned aerial vehicle navigation.

Publications arising from the thesis

This thesis comprises contents from the following papers (published or under review):

Yu W, Ding X, Chen W, Dai W, Yi Z, Zhang B. (2019). Precise point positioning with mixed use of time-differenced and undifferenced carrier phase from multiple GNSS. Journal of Geodesy, 93, 809-818. doi: 10.1007/s00190-018-1201-8.

Yu W, Ding X, Dai W, Chen W. (2017). Systematic error mitigation in multi-GNSS positioning based on semiparametric estimation. Journal of Geodesy, 91, 1491-1502. doi: 10.1007/s00190-017-1038-6.

Yu W, et al. (2019) Two-step robust multi-GNSS positioning (under review)

Yu W, et al. (2019) Deformation monitoring using multi-GNSS observations. (under review)

Acknowledgements

I enjoyed the freedom of research during the seven years of working and studying at the Hong Kong Polytechnic University. So many people need thanking for their help in making this work a success.

At first, I would like to sincerely thank my supervisor, Prof. Xiaoli Ding, for his excellent guidance and complete support. The insightful comments from my co-supervisor, Prof. Wu Chen, are kindly appreciated. A special thank should also go to Prof. Wujiao Dai at the Central South University, Changsha, for his valuable suggestions and constant encouragements. The constructive comments from Prof. Chia-Chyang Chang at the Chien Hsin Usiversity of Science and Technology, Taiwan, Prof. Linyuan Xia from the Sun Yat-Sen University, Guangzhou, are gratefully acknowledged.

The time studying with so many brilliant groupmates at PolyU is a precious memory. They are Lei Zhang, Wenbin Xu, Mi Jiang, Wu Zhu, Chisheng Wang, Linghong Ke, Bochen Zhang, Jittin Chaitamart, Songbo Wu, Kai Tan, Hungyu Liang, Xiao Tang, Hongyu Liu, Jianwei Cai, Qifan Wan, Jia Li, Meng Duan, Zefa Yang, Zeyu Zhang, Jingwen Zhao, Bin Zhang, and Xuanyu Qu. The contribution from Wentao Yang and Zhian Huang are gratefully acknowledged, the teamwork in GNSS projects is wonderful.

I would also like to extend my gratitude to W.K. Ho, Biyan Chen, Qiliang Liu, Zhe Yang, Jing Qiao, Ying Xu, Miaomiao Cai, Jinxin Zhu, and other teachers and colleagues who helped me indirectly to complete this work.

This thesis is dedicated to my grandma, parents, and sisters for their unconditional love, understanding, and support.

Table of contents

List of figures

List of tables

Chapter 1 Introduction

1.1 Background

Efforts in integrating observations from multiple global navigation satellite systems (GNSSs) date back to the 1990s when GLONASS was developed as a competitor of the pioneer GPS (Vieweg and Lechner, 1994; Pratt et al., 1998; Zarraoa et al., 1998; Han et al., 1999). Since then some fundamental issues of multi-GNSS positioning, including mathematical modeling, ambiguity resolution (Wang, 2000; Wang et al., 2001; Dai et al., 2003; Banville et al., 2018) and ephemeris determination (Weber and Springer, 2001) have been extensively studied. To handle the new GNSS signals, relevant data-processing software packages have also been developed/upgraded (e.g., Takasu, 2012; Dach et al., 2015). In recent years, in addition to the modernizing GPS and GLONASS (re-achieving a full constellation in 2011), other systems, including BeiDou and Galileo, have been rapidly developed (Hofmann-Wellenhof et al., 2008; Revnivykh, 2012; Bartolomé et al., 2015; CSNO, 2019). Consequently, more than 120 satellites are anticipated to be available by 2020 (Dow et al., 2009; Montenbruck et al., 2013; Bock and Melgar, 2016).

The increasing number of available satellites enhances signal continuity, integrity and geometry (Hofmann-Wellenhof et al., 2008; Yang et al., 2011; Leick et al., 2015; Kaplan and Hegarty, 2017). Improvements in aspects such as estimation accuracy, convergence time, and elevation angles have been widely reported in literature (Teunissen et al., 2014b; Li et al., 2015a; Lou et al., 2015; Odolinski et al., 2015). Multi-GNSS positioning also enables a trend of high spatial/temporal-resolution geodetic/geophysical applications (Bock and Melgar, 2016). For example, Geng et al. (2016) showed that GPS/BeiDou combination achieves an improvement of approximately 20% in velocity estimation compared with GPS-only solutions and the combination is beneficial to real-time geodetic applications, such as earthquake warning and tsunami forecasting.

1.2 Problem statement

1.2.1 Mismodeling and estimability

Combining observations from different satellite systems sometimes may not necessarily be more advantageous if errors in the observations cannot be well modeled. For instance, BeiDou signals may be more susceptible to multipath effects compared with GPS due to a mixed constellation structure. As presented by Ye et al. (2015), the multipath mitigated positioning precision of BeiDou is lower than that of GPS. Shi et al. (2013) observed that biases of GPS-only solutions are normally smaller than those of BeiDou-only solutions, and in some cases, multi-system solutions even enlarge the biases compared with solutions using data from GPS only. Another example is the integration of pseudolite and GPS (Meng et al., 2004). It has been reported that the accuracy is significantly degraded when pseudolite observations with strong multipath signals are used.

Compared with the code-division multiple-access GNSSs, the frequency-division multiple-access GLONASS observations are more complicatedly affected by hardware delays that cause inter-frequency biases (IFBs) (Wanninger, 2012). Al-Shaery et al. (2013) estimated IFBs in zero-baselines and recommended using the derived biases in pre-calibration. Henkel et al. (2016) and Banville et al. (2018) proposed ambiguity transformation methods that use two reference satellites to retain the integer nature of GLONASS double-differenced ambiguities, while a careful selection of reference satellites is required to avoid small wavelengths of the transformed ambiguities. Wang (2000) suggested a search process to obtain the GLONASS reference satellite's single-differencing (SD) ambiguity and proposed to treat the SD ambiguity as a real-valued parameter in the final solution. Even for systems with overlapping frequencies (e.g. GPS/Galileo), hardware biases cannot be neglected when receivers of different types are involved (Paziewski and Wielgosz, 2015). Tian et al. (2015) suggested a particle filter to estimate the IFBs and further extended the method in estimation of inter-system biases (ISBs) (Tian et al., 2019). Nadarajah et al. (2013) observed hardware-induced biases in BeiDou observations

formed across different satellite types, which can cause failures in ambiguity resolution. Hewitson and Wang (2006) pointed out that ISBs can lead to unreliable estimation when insufficient satellites from the corresponding systems are tracked. Although applying external corrections can eliminate some of the biases, such as inter-system time offsets and hardware delays (Kouba, 2015; Teunissen and Khodabandeh, 2015), certain latencies in producing external corrections hinder their real-time applications. For observations from some of the new satellite systems and low-cost mass-market receivers, precise calibrations have often not been done properly (Lou et al., 2014; Banville et al., 2018). In addition, hardware delays are in general assumed stable and estimated as daily constants, a higher resolution of estimation is suggested to account for their time variations (Dach et al., 2010).

Multipath errors and unmodeled hardware delays can result in systematic errors that bias the least-squares estimation (Xu, 1991). Penalization estimation is widely employed to estimate the slowly varying or constant systematic errors. However, the penalization parameters are often inestimable due to their linear or near-linear dependence with other parameters. For instance, when introducing too many bias parameters to combine frequency division multiple access GLONASS signals, ill-posed or even rank deficiency problems may occur (Banville et al., 2018). Imposing constraints and reparameterization are frequently done to make the systematic errors estimable (Leick et al., 2015; Teunissen and Khodabandeh, 2015). However, prior knowledge of the penalization parameters is in general limited. Although reparameterization can avoid the linear dependence, the definition of the corresponding parameter varies accordingly, i.e., relative to the base station, satellite, frequency, or system (Leick et al., 2015). This complicates the GNSS data processing sometimes. For example, undifferenced ambiguities in precise point positioning (PPP) are lumped together by the between-satellite single-differencing operation (Li and Zhang, 2014), while they are also non-integers due to the existence of hardware-induced uncalibrated phase delays (Ge et al., 2008). Applying cross-system differencing can reduce the number of ISBs (Kubo et al., 2017; Li et al., 2017) whereas selecting a common reference satellite may lead to intersystem correlations that can considerably enlarge the minimal detectable biases (Yang et al., 2013).

1.2.2 Multiple outliers

Another challenging issue is that more frequent multiple outliers may occur in the growing amount of observations. Conventional gross error mitigation methods assume a single outlier which may be unrealistic when processing a multi-GNSS dataset (Pozo-Pérez et al., 2017). Moreover, in a high-dimensional ambiguity resolution a subset of ambiguities generally can be reliably resolved compared with the full set (Brack, 2017). The ambiguities incorrectly fixed can cause large positioning errors. Dealing with multiple simultaneous outliers is an intractable task (Knight et al., 2010), in which some traditional methods such as autonomous integrity monitoring can be deteriorated (Angus, 2006).

1.2.3 Computation complexity

The increased observation diversity and redundancy can dramatically complicate the computation of multi-GNSS positioning. Integration of multi-GNSS observations expands the functional model to account for extra ambiguities, hardware biases, and inter-system discrepancies (Leick et al., 2015). This inefficiency can be more evident when handling GLONASS data (Banville et al., 2018) or a network in which a large number of ambiguities need to be estimated (Chen et al., 2014). In addition, traditional outlier controlling can become time-consuming. Outliers are unknown in practice and an iterative process is typically used in outlier-testing (Knight et al., 2010) or in the alternative approach, i.e. robust estimation (Yang et al., 2002). Much attention has been given to reducing the computation complexity of GNSS positioning. For example, when processing a large network that involves massive matrix operations and a large amount of parameters, the calculation is simplified technically by applying block-partitioned algorithms (Gong et al., 2018) and ambiguity elimination (Ge et al., 2006). Another approach for reducing parameters is time-differing, which eliminates constant parameters such as ambiguity, intersystem time offsets, and hardware biases. The time-difference operation, however, enlarges the noise and requires an accurate initial position (Zhao, 2016).

1.3 Objectives and expected outcomes

The achieved results of multi-GNSS positioning hitherto are considered promising, whereas unmodeled errors therein and the increasing computation complexity have yet to receive enough attention. For high-performance multi-GNSS positioning, this study aims to achieve the following objectives:

- To mitigate the impacts of systematic errors on multi-GNSS positioning.
- To enhance the combined positioning models by accommodating the requirements of high accuracy and efficiency.

Special considerations will be given to designing practical procedures when implementing these objectives. The developed algorithms will be tested in positioning with simulated and real-world data.

1.4 Dissertation outline

The dissertation is composed of work shown in Figure 1-1. Chapter 2 investigates the benefits of using observations from multiple GNSSs, with current and future full operational constellations simulated. The benefits explain the necessity of multi-GNSS integration. Chapter 3 presents the use of semiparametric estimation (SPE) that expands the parameter list to absorb systematic errors in multi-GNSS static relative positioning. Chapter 4 proposes to shrink the parameter list in multi-GNSS PPP, which is implemented by the mixed use of time-differenced and undifferenced carrier phases. Chapter 5 shows a two-step combination procedure that separates positioning into subset and full-set estimations. Chapter 6 finally provides some concluding remarks and possible future work.

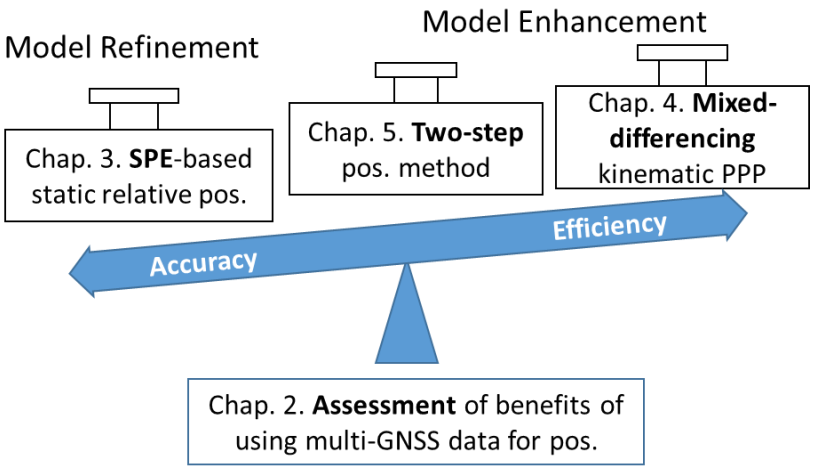

Figure 1-1 Main research contributions

Chapter 2 Enhancement of positioning in challenging environments using multi-GNSS observations

2.1 Motivation

In monitoring crustal motion, landslides, structural deformation, subsidence, and volcano eruptions, GPS is complementary or an alternative to robotic total stations, leveling, interferometric synthetic-aperture radar (InSAR) and in-situ sensors. Therefore, it has been widely used in such applications (Bock et al., 1993; Motagh et al., 2007; Berrocoso et al., 2012; Crosta et al., 2014). However, a high performance of positioning is unattainable in some cases due to limited satellite geometry. For instance, the positioning accuracy degrades in the vertical direction in deep-cut valley areas (Yin et al., 2010) and in the north component due to the observability hole of satellites (Parkinson and Spilker, 1996). In addition, the radio signals of GPS satellites are vulnerable to ambient disturbances. A long-standing issue is the multipath effect (roughly including here signals of non-line-of-sight, reflection, and diffraction) (Hannah, 2001; Leick et al., 2015). Considerable research effort has been devoted to overcoming these inherited bottlenecks of GPS positioning from three main aspects. The first aspect is enhancing the geometry by using ground-based signal sources, such as pseudolite (Dai et al., 2002; Meng et al., 2004). The second is integrating GPS with non-GPS technologies, such as accelerometers (Meng, 2002; Chan et al., 2006; Tu et al., 2013) and InSAR (Komac et al., 2015; Hu et al., 2018). The third is developing advanced data processing algorithms (Han and Rizos, 2000; Zheng et al., 2005; Zhong et al., 2010; Dai et al., 2014; Dong et al., 2016). These approaches benefit positioning to a certain degree, but they also have their own limitations. For example, accelerometers present drifting errors (Im et al., 2013) and InSAR is expected to make frequent observations. The location of pseudolite and multipath mitigation techniques must be carefully addressed (Yi et al., 2013). Sophisticated data processing methods can complicate the monitoring systems. A trade-off between accuracy and complexity is thus generally required.

In recent years several non-GPS satellite systems, including BeiDou, GLONASS, and Galileo, have been rapidly developed. More than 120 satellites can be available by 2020 (Bock and Melgar, 2016). Compared to GPS-only solutions, multi-GNSS integration has advantages such as higher positioning accuracy, larger cut-off angle, and faster convergence (Dai et al., 2003; Rizos, 2008; Cai and Gao, 2013; Chu and Yang, 2014; Teunissen et al., 2014a; Li et al., 2015b). GPS-only monitoring systems can be dramatically impacted by signal obstruction and the multipath effects that are often present in some challenging monitoring environments. Therefore, understanding the capabilities of the combination of multi-GNSS observations in monitoring applications is important, especially when the current four main satellite systems all run in full operational capacity. The impact of multipath effects on the applicability of multiple GNSSs is also worth investigation.

The next section presents the simulation of multiple constellation observations and several typical scenarios in deformation monitoring. Experimental results based on simulated and real datasets are then presented, followed by summarized remarks.

2.2 Constellations and observations

Dilution of precisions (DOPs) and observation accuracy critically determine the positioning accuracy (Leick et al., 2015). DOPs depend on the number and distribution of satellites observed. At present GPS and GLONASS have full deployment of 31 and 24 satellites respectively in their constellations (Table 2-1). The BeiDou system has a mixed constellation structure that consists of medium Earth orbits (MEO), geostationary Earth orbits (GEO), and inclined geosynchronous orbits (IGSO). BeiDou's initial service was declared on Dec. 27, 2012. Six years later (i.e., on Dec. 27, 2018), the preliminary system of 3rd generation of BeiDou was also announced (CSNO, 2019). At the time of writing, the BeiDou constellation consists of 33 operational satellites: 5 GEOs, 7 IGSOs and 21 MEOs, with 18 MEOs being BeiDou-3 satellites. BeiDou's 3rd generation system is expected to be completed by 2020. The

initial open service of Galileo was declared operational on Dec. 15, 2016, and the Galileo constellation is on track to reach completion in 2020.

To better understand the positioning performance with future full quad-GNSS constellations (i.e. GPS, BeiDou, GLONASS, and Galileo), observations are simulated. In addition, since the multipath effect is a major error source that affects the realistic observation accuracy, the geometric models are developed and then applied for multipath error simulation. Several typical signal-shadowing environments are also studied.

Table 2-1 GNSS constellations

	GPS	GLONASS	BeiDou	Galileo
Status* (04/14/2019)	31MEO	24MEO	21MEO+5GEO+7IGSO	22MEO
Nominal constell.	31MEO	27MEO	27MEO+5GEO+3IGSO	30MEO
MEO Model	Irregular, 27 +4 spares	Walker 24/3/1 +3 spares	Walker 24/3/1 +3 spares	Walker 24/3/1 +6 spares
Orbital planes	6	3	3	3
Inclination	55°	64.8°	55°	56°
Plane separation	60°	120°	120°	120°
Inter-plane phase	-	±45°	±45°	±45°
Attitude [km]	20200	19140	MEO:21528, GEO/IGSO:35786	23222
Period [h]	11.967	11.262	12.890 (MEO)	14.117
Coordinate frame	WGS84	PZ-90.11	CGCS2000	GTRF
Time frame	GPST	UTC (SU)	BDT	GST

*www.gps.gov; www.glonass-iac.ru; www.beidou.gov.cn; www.gsc-europa.eu

2.2.1 Simulation methods

Simulation of GNSS constellations is implemented on the basis of the simplified perturbation models (Vallado et al., 2006). Earth-centered inertial orbits are calculated using two-line element (TLE) files published by the North American Aerospace Defense Command (NORAD). TLEs store the Keplerian orbital parameters (i.e. right ascension of ascending node, argument of perigee, inclination, eccentricity, semi-major axis, and mean anomaly) of any known earth-orbiting object tracked (Kelso,

2015). To obtain the nominal full GNSS constellations (see Table 2-1 above), TLEs of those planned to launch are generated using the calculation method of Walker constellation (Kaplan and Hegarty, 2017, p.232) and corresponding Interface control documents (ICDs) (RISDE, 2008; GPS Directorate, 2013; EU, 2016; CSNO, 2019).

The simulated satellite orbits are stored in SP3 format (Hilla, 2010) and then used via interpolation. Coordinates and time frames are aligned to WGS84 and GPS time respectively. With the simulated constellations, the basic GNSS code (P) and phase (φ) measurements are generated based on the following formulae and then stored in the RINEX format (Gurtner and Estey, 2013).

$$\begin{cases} P = \rho + c(\tau - \tau^s + \tau_0) + m_{trp}T + m_{ion}I + s_P + \varepsilon \\ \dfrac{c}{f}\varphi = \rho + c(\tau - \tau^s + \tau_0) + m_{trp}T - m_{ion}I + s_\varphi + \epsilon \end{cases} \tag{2-1}$$

where $\rho = \|\boldsymbol{r} - \boldsymbol{r}^s + \Delta\boldsymbol{r}^s\|$ is the distance between receiver ($\boldsymbol{r}$) and satellite ($\boldsymbol{r}^s$), with orbit error ($\Delta\boldsymbol{r}^s$); c stands for the light speed in vacuum; τ, τ^s, and τ_0 are respectively the receiver clock error, satellite clock error and inter-system time-offset (GPS time is selected as reference); T and I are the zenith delays in troposphere and ionosphere respectively, they are mapped to the slant direction through mapping functions m_{trp} and m_{ion}; s_P and s_φ are the multipath errors on code and phase measurements respectively; ε and ϵ are the observation errors for code and phase; and f is the signal frequency. Table 2-2 shows the frequencies of the simulated carrier phase observations. Additional detailed descriptions about the measurement characteristics can be found in relevant ICDs.

Table 2-2 GNSS signals to simulate

	Carrier phase frequency (MHz)
GPS L1	1575.420
GLONASS G1	1602+1125/2*k (k= -7 to +6)
BeiDou B1	1561.098
Galileo E1	1575.420

For short baselines in deformation monitoring, the differencing operation can considerably eliminate/mitigate most errors except for those from multipath effects. Therefore, instead of very accurately modeling all these errors, approximations shown in Table 2-3 are adopted in this study. Strategies for precise simulations can be found in previous studies (e.g. Dolgansky, 2010; Shu et al., 2017). Stochastic errors are assumed white, and those of multipath effects are designed to be proportional to the total multipath delays. Measurement noise is also modeled, and the noise term is applied to avoid the cancelation of generated delays in data processing. The UNB3m model and Neill mapping functions (Leandro et al., 2008) are used to generate tropospheric delays. Ionospheric delays are produced using the single-layer model and global mapping function. Other satellite systems share the same features of GPS except for the frequency-division multiple-access GLONASS, in which the ionospheric delays are modeled for each satellite separately depending on their officially published frequency numbers (www.glonass-iac.ru). Multipath errors are simulated based on the developed reflection and diffraction geometric models (Section 2.2.2 provides additional details).

Table 2-3 Strategy for simulating GNSS errors

Error source	A priori value	Noise (1 sigma)
Orbit error	0	1.0 m
Satellite clock bias	0	0.3 m
Receiver clock bias	30 m	3.0 m
Inter-system time offsets	3 m	0
Tropospheric delay	UNB3m + Neill	0.003 m (zenith)
Ionospheric delay	Single-layer + GMF	0.005 m (zenith)
Code error	0	0.5 m
Carrier phase error	0	0.01*wavelength
Multipath delay	Geometric models	0.01*delay

2.2.2 Multipath geometric models

To approximate a realistic environment of deformation monitoring, this section reviews the multipath geometry model and scenarios of signal blockage. Figure 2-1 illustrates the ground bounce reflection model (Hofmann-Wellenhof et al., 2008) and the model with a vertical planar wall (Leick et al., 2015). Incident signals are assumed

as parallel due to the long satellite-receiver distance. Here, only the specular reflection is considered. A GNSS antenna receives reflected signals from the ground/wall in addition to a line-of-sight (LOS) signal.

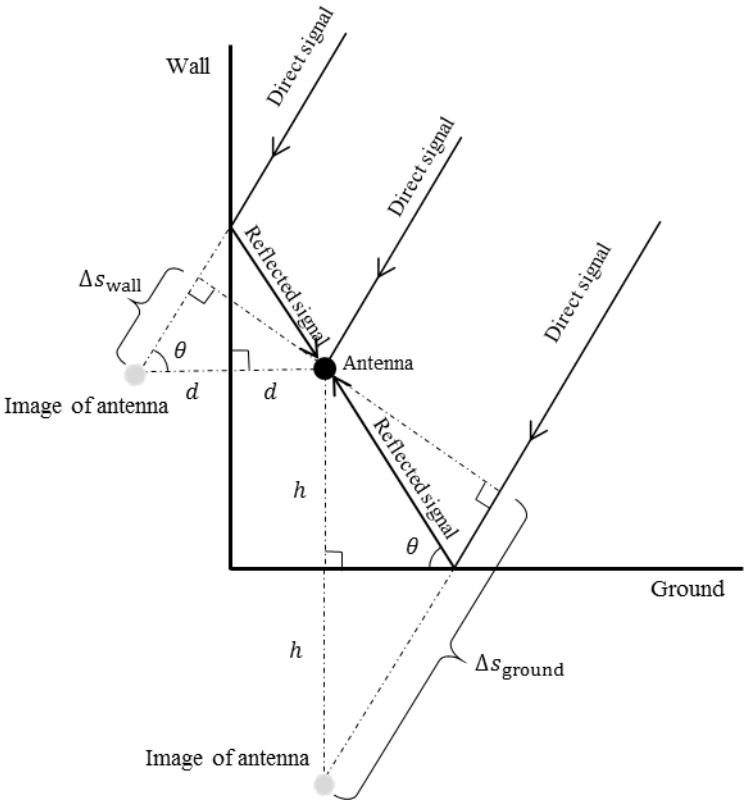

Figure 2-1 Traditional multipath reflection model

The reflected signal travels an additional distance (Δs), and it can be expressed as follows according to the geometric relationship.

$$\begin{cases} \Delta s_{\text{wall}} = 2d\cos(\theta) \\ \Delta s_{\text{ground}} = 2h\sin(\theta) \end{cases} \tag{2-2}$$

where h is the antenna height; θ is the satellite elevation angle; and d is the distance from the antenna to the vertical plane. For the impact from reflection on carrier phase, the interferential signal S_M comprises the direct signal $S_D = A\cos(\varphi)$ and reflected signal $S_R = \beta A\cos(\varphi + \Delta\varphi)$. Thus, they can be written as (Leick et al., 2015, p.287)

$$\begin{cases} S_M = S_D + S_R = \beta_M A\cos(\varphi + \Delta\varphi_M) \\ \beta_M = \sqrt{1 + \beta^2 + 2\beta\cos(\Delta\varphi)} \\ \Delta\varphi_M = \operatorname{atan}\left(\dfrac{\beta\sin(\Delta\varphi)}{1 + \beta\cos(\Delta\varphi)}\right) \\ \Delta\varphi = \dfrac{2\pi\Delta s}{\lambda} \end{cases} \tag{2-3}$$

where A is the amplitude of LOS signal; β_M and $\Delta\varphi_M$ are the damping factor and phase of the interferential signal respectively; $\Delta\varphi$ is a phase delay due to extra path Δs of the multipath signal relative to the LOS signal; and $\beta \in (0,1)$ is the reflected signal's damping factor, a function of geometric and physical factors (Lau and Cross, 2007). This study focuses on modeling the path delay Δs based on relevant geometry information, discussions of other factors that affect the multipath can be found in some classical references (Parkinson and Spilker, 1996; Hofmann-Wellenhof et al., 2008; Leick et al., 2015; Kaplan and Hegarty, 2017).

The reflector's azimuth and slope angles are further considered, as a result, the traditional 2D multipath reflection model is extended into:

$$\begin{cases} \Delta s = 2d\sin(\theta_e) \\ \theta_e = \operatorname{asin}\{\sin(\theta' + \theta_r)\cos\{\operatorname{atan}[\tan(\alpha - \alpha_r)\cos(\theta')]\}\} \\ \theta' = \operatorname{atan}_2(\tan(\theta), \cos(\alpha - \alpha_r)) \end{cases} \tag{2-4}$$

where θ_e is an equivalent satellite elevation; d is the perpendicular distance from the antenna to the reflector surface; α_r and θ_r are the slope aspect and slope angle of the reflector respectively; and α is the satellite azimuth angle (Appendix C provides details). The LOS signal will be either blocked or diffracted when θ_e is non-positive. The traditional ground bounce model ($\theta_r = 0$) and vertical plane model ($\theta_r = \frac{\pi}{2}$) are two special cases of the above-mentioned model without the azimuth parameter ($\alpha = \alpha_r$). A vector form of reflection model can be found in (Lau and Cross, 2007).

Another major interference is diffraction. It occurs when a signal is incompletely shadowed by an obstructing object that is bending the signal around its edges.

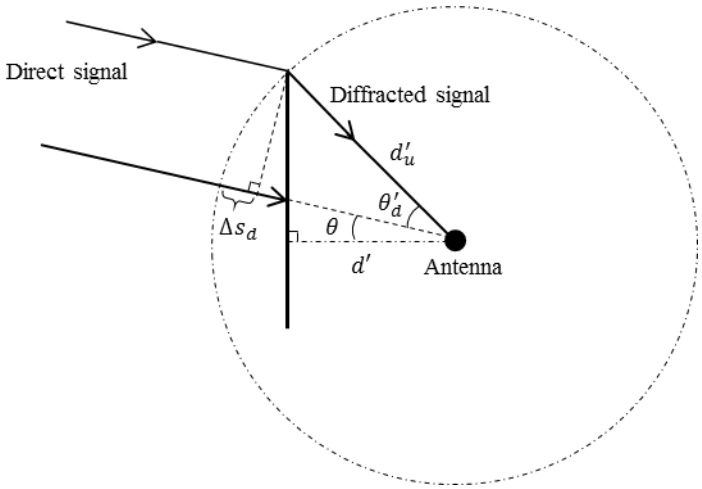

Figure 2-2 Traditional multipath diffraction model

The path delay Δs_d of a diffracted signal with respect to a direct signal blocked can be expressed as (Hannah, 2001, p.182)

$$\begin{cases} \Delta s_d = (1 - \cos(\theta'_d))d'_u \\ \theta'_d = \text{atan}\left(\dfrac{\sqrt{(d'_u)^2 - (d')^2}}{d'}\right) - \theta \end{cases} \tag{2-5}$$

where d'_u is the distance from the edge to the antenna; θ'_d is the included angle of the diffracted signal and LOS signal; and d' is the horizontal distance from the antenna to the location of the diffraction. Considering the azimuth and slope angles into the diffraction model yields (Appendix C provides details)

$$\begin{cases} \Delta s_d = (1 - \cos(\theta'_d))\sqrt{d_u^2 + (\sin(\alpha - \alpha_r)d')^2} \\ \theta'_d = \text{atan}\left(\dfrac{\sqrt{d_u^2 - (\cos(\alpha - \alpha_r)d')^2}}{d'}\right) - \theta \end{cases} \tag{2-6}$$

To restrict the diffraction delay within one phase cycle, the delay Δs_d is empirically multiplied by a scale factor $\frac{\text{wave length}}{d'_{u\_max}}$. Here, d'_{u_max} is the maximum path length from the edges to the antenna. This scaling operation will not affect the experimental results since the diffraction model is used only in identifying the diffracted signals, and no attempt is made to correct the diffraction errors.

2.2.3 Typical monitoring environments

Figure 2-3 shows three scenarios with signal blockages that are often encountered in deformation monitoring, namely slopes, canyons, and bridge-crossing. The simulation of these scenarios can be implemented using elevation masks. To describe the location and two boundaries of an obstruction, the mask is designed in the form of "azimuth, elevation of the lower boundary, elevation of the higher boundary". Data identified as being shadowed will be eliminated.

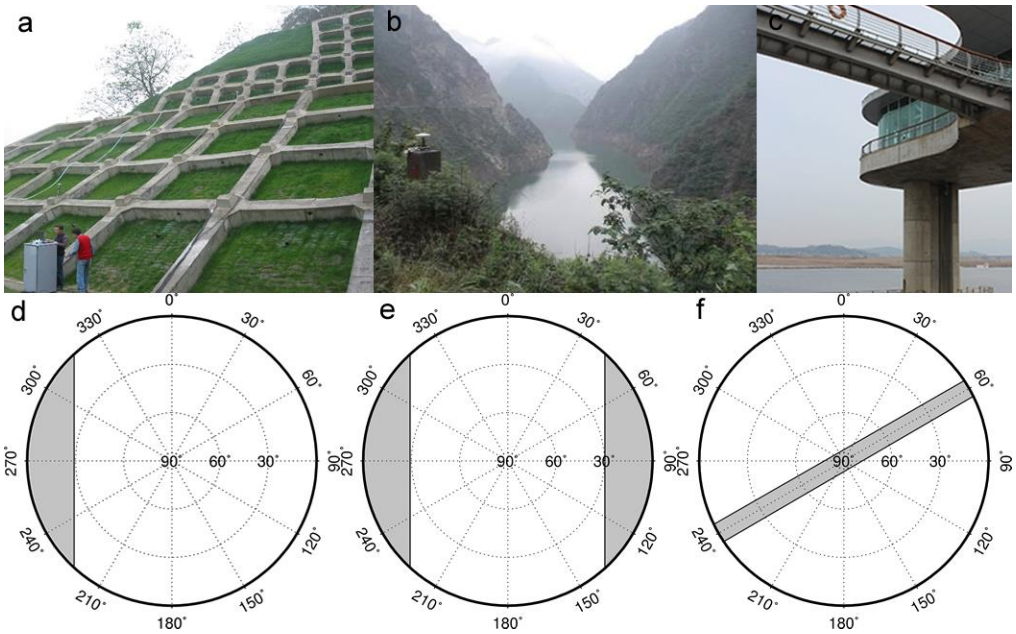

Figure 2-3 Typical environments in GNSS deformation monitoring: (a) slope, (b) canyon, and (c) bridge crossing; corresponding signal masks: (d) one-side shadowing, (e) two-sides shadowing, and (f) middle-belt shadowing.

2.3 Experiments and results

2.3.1 Constellation simulation

TLEs of 14 April 2019 were downloaded from NORAD to generate the current GNSS constellations (see Table 2-1 above). Simulation of the future full constellations is implemented by adding TLE records of nominal MEO vehicles to the current TLE set. The final satellite number may not precisely match what was designed (some current BeiDou GEO/IGSO satellites are not disabled. Spare satellites from non-GPS systems are also considered, they are nearly equally distributed to planes), while this condition

is considered acceptable for simulation. Figure 2-4 presents the distributions of simulated constellations. Figure 2-5 shows the global maps (1°×1° resolution, 5° cut-off angle, at altitude of 10 m) of the satellite ground trajectories (24 h commencing 00:00:00 04/14/2019 UTC), visible satellite number, and position DOP (PDOP) (at 04/14/2019 00:00:00 UTC). Compared with GPS, multiple GNSSs have a more dense and higher signal coverage, thereby leading to lower PDOP values. This situation is especially true in the Asia Pacific areas, due to the contribution of BeiDou GEO/IGSO satellites. As summarized in Table 2-4 (in which G, R, C, and E denote GPS, GLONASS, BeiDou, and Galileo respectively) the global mean of the satellite number of GPS is 10 and the mean PDOP is 2.1. Combining other GNSSs considerably improves the satellite number by 2.8 times and reduces the PDOP by 52.4%. The current constellations are approaching their full conditions. When all these GNSSs run at full status, approximately 44 satellites can be observed globally and the mean PDOP is 57.1% smaller than that based on GPS alone.

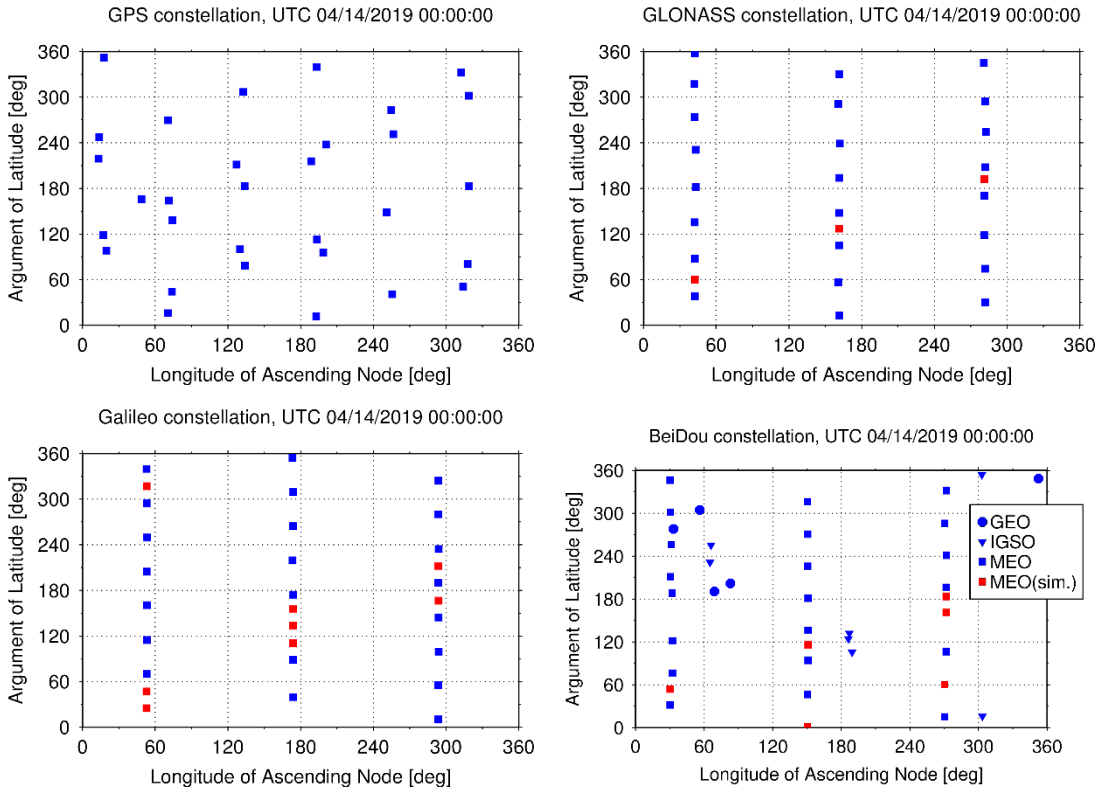

Figure 2-4 Current (04/14/2019) and simulated (red color) GNSS constellations

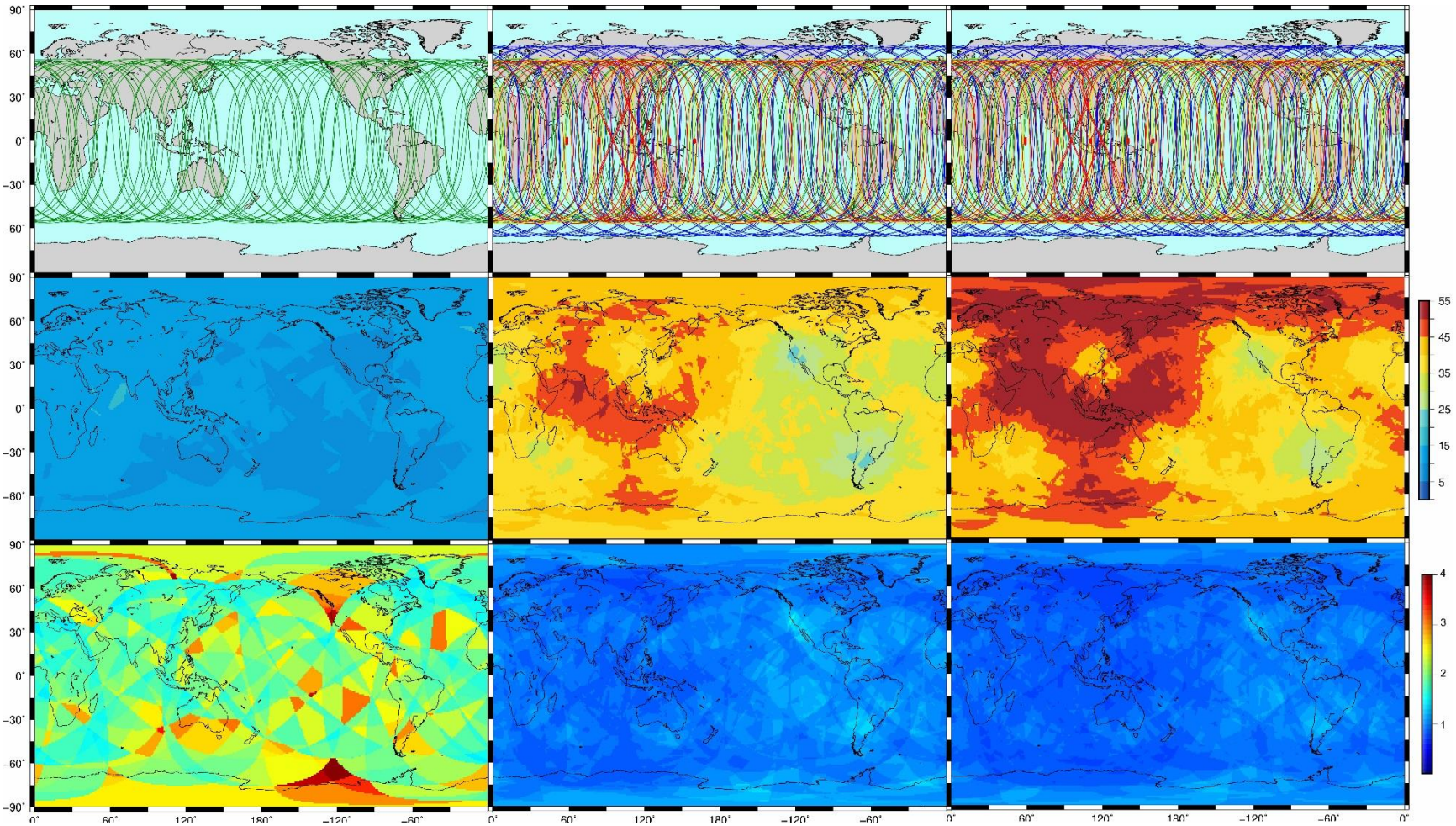

Figure 2-5 Satellite ground tracks (upper row, GPS in green, GLONASS in blue, BeiDou in red, and Galileo in yellow), visible satellite number (middle row) and PDOPs (bottom row) of GPS-only (left column), quad-GNSS (middle column), and full-constellation quad-GNSS (right column)

Table 2-4 Statistics of global constellation information

System	Mean sat. #	Mean PDOP	Impr. of sat. # [%]	Reduction of PDOP [%]
G	10	2.1	-	-
GRCE	38	1.0	280.0	52.4
GRCE (full)	44	0.9	340.0	57.1

2.3.2 Positioning tests

To compare the performance in using observations from multi-GNSS and GPS, 23 h 1-Hz multi-GNSS data from a baseline of approximately 4 m was collected from 07:00:00, 16 May 2018 (GPS time), at the campus of Central South University. Trimble NetR9 receivers were used, with a "Zephyr" antenna for the rover and a "Zephyr Geodetic" antenna for the base. As shown in Figure 2-6, a multipath-strong environment was established by placing a metal reflector to the north of the rover's antenna. The sizes and orientations of the reflector are provided in Table 2-5. These parameters are input to the empirical multipath geometric models. For simplicity, only single-reflection and single-edge (the upper edge within a bending angle of 40°) diffractions are considered. Note that the multipath models are used only to identify multipath events, although applying them as prior observation corrections is another useful and challenging topic.

Figure 2-6 Installation of (a) rover with an open sky, (b) a vertical reflector, and (c) a reference station with a distance of approximately 4 m

Table 2-5 Geometry of the reflector

θ_r [deg]	α_r [deg]	d [mm]	d_u [mm]
95	180	215	657

Figure 2-7 illustrates the sky plots of double-differenced (DD) L1/G1/B1/E1 residuals and the simulated multipath errors (the damping factor β is set to 0.15). In the DD residuals, major components of the multipath errors are reconstructed, and the diffraction effect is apparently dominant. Compared with the real DD residuals the simulation results have larger diffraction errors with more visible reflection Fresnel zones. Figure 2-8 shows DD residuals and simulated multipath errors from three satellites of different orbit types. A good agreement in the diffraction pattern can be observed between the measurements and simulation results although evident deviations exist, especially for the GEO C01, which may be caused by the adopted simplifications.

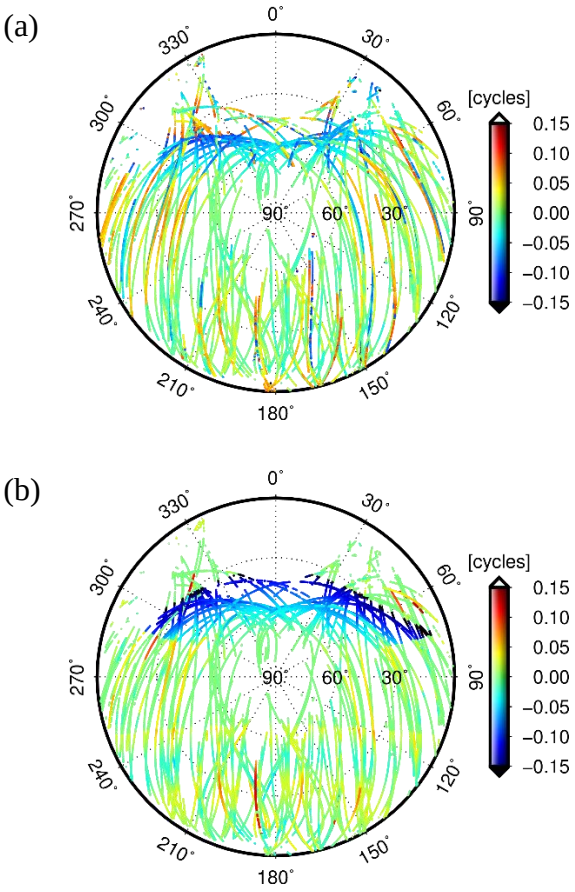

Figure 2-7 Sky plots of (a) DD residuals and (b) simulated multipath delays

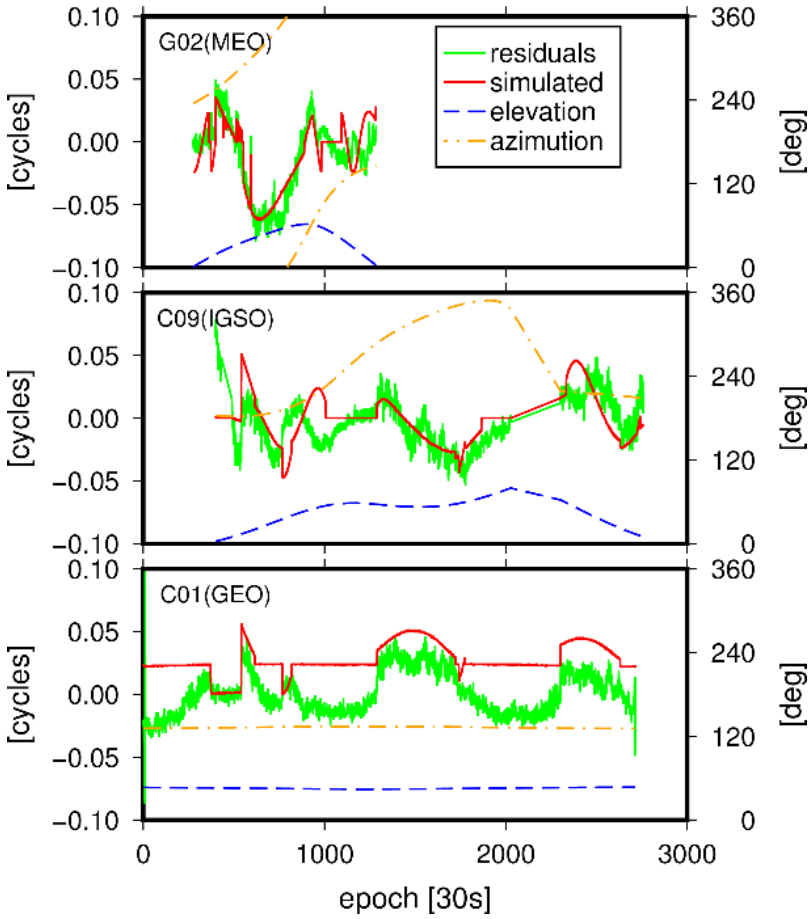

Figure 2-8 Examples of DD residuals (green) and simulated multipath delays (red) from satellites of different orbit types (a reference satellite is selected for each GNSS)

The real dataset is sampled at 30 s and then divided into 23 1-h sessions. They are processed in static relative positioning. The results are compared with true baseline values computed based on an open-sky 1-h dataset acquired beforehand (Figure 2-6a). Diffracted signals are eliminated due to their large error magnitudes (Dai et al., 2017).

Table 2-6 shows the baseline errors with different shadowing conditions controlled by signal masks (see Sect. 2.2.3). In the interference-rich environment, the results from all solutions show large errors in the north and up coordinate components. Compared with GPS-only solutions using quad-GNSS data remarkably reduces the 3D RMS errors by 44.5%. These improvement rates increase by 48.4–52.4% when signals are seriously shadowed.

Table 2-6 Baseline errors from different systems and masks

Mask	Systems	Mean [mm]			RMS [mm]			3D RMS	Impr.
		North	East	Up	North	East	Up	[mm]	[%]
Non	G	6.1	-0.5	0.1	11.8	4.2	11.3	16.9	
	GRCE	3.9	-1.4	0.8	5.8	2.9	6.8	9.4	44.5
One-side	G	6.4	-1.6	-1.5	12.3	5.8	15.5	20.6	
	GRCE	4.1	-1.8	0.7	6.6	3.2	7.7	10.6	48.4
Two-sides	G	6.3	-0.7	-0.5	14.3	6.2	23.8	28.4	
	GRCE	3.1	-2.0	2.7	7.1	3.6	11.0	13.5	52.4
Middle-belt	G	7.3	-2.7	-4.7	14.1	7.3	16.9	23.2	
	GRCE	3.7	-2.2	-3.0	6.1	4.0	9.2	11.8	49.3

Table 2-7 shows the baseline errors when observations identified as being contaminated by diffractions are retained in the dataset. The importance of eliminating the diffracted signals is evident. Compared with the results in Table 2-6 the positioning results are dramatically deteriorated without removal of the diffracted signals. Errors in the north and up components increase considerably, from the mm level to cm level. Using the multi-GNSS data is helpful in these adverse signal conditions. The position RMS errors are decreased by 8.1–42.4% compared with those of the GPS-only method.

Table 2-7 Baseline errors from different systems and masks without removal of diffracted signals

Mask	Sys.	Mean [mm]			RMS [mm]			3D RMS	Impr.
		North	East	Up	North	East	Up	[mm]	[%]
Non	G	-24.3	1.3	15.0	29.6	10.9	23.2	39.2	
	GRCE	-24.0	1.3	13.6	26.2	9.6	22.7	36.0	8.1
One-side	G	-25.0	1.6	16.5	30.5	12.8	27.8	43.2	
	GRCE	-24.7	2.3	16.2	27.0	10.4	24.8	38.2	11.6
Two-sides	G	-28.8	-2.7	33.5	35.1	13.2	55.5	67.0	
	GRCE	-26.7	-0.1	25.3	29.2	10.5	34.1	46.1	31.1
Middle-belt	G	-37.6	-7.4	26.9	47.4	23.6	58.1	78.6	
	GRCE	-28.8	-3.3	18.5	30.9	12.1	30.8	45.3	42.4

Simulation experiments are also conducted to understand the benefit of using quad-constellation data in deformation monitoring. The same setup of the baseline shown

in Figure 2-6 is applied. Twenty-four 1-h sessions are simulated. Table 2-8 summarizes the baseline errors, based on the simulated observations of current quad-constellation and future full quad-constellation. Compared with the results based on real data, the diffracted signals can be more accurately identified in the simulated observations. This accurate identification results in minimal influences of diffractions and considerable contributions from satellite DOPs to positioning solutions. As shown in Table 2-8 using the current quad-constellation reduces the positioning RMS errors by 39.4% when compared with the GPS-only solution, and the improvement remarkably increases to 48.6–63.8% in environments with severe signal blockages. When the four GNSSs are all completed, 48.5–69.0% improvements in positioning accuracy can be achieved.

Table 2-8 Baseline errors from different systems and masks based on simulated constellations

Mask	Sys.	Mean [mm]			RMS [mm]			3D RMS [mm]	Impr. [%]
		North	East	Up	North	East	Up		
Non	G	-0.3	0.1	-1.1	1.4	1.1	2.8	3.3	
	GRCE	-0.1	0.0	-0.8	0.7	0.6	1.7	2.0	39.4
	GRCE(full)	-0.2	0.0	-0.5	0.7	0.6	1.4	1.7	48.5
One-side	G	-0.1	0.1	-0.8	1.9	1.1	3.0	3.7	
	GRCE	-0.2	0.1	-0.7	0.7	0.7	1.6	1.9	48.6
	GRCE(full)	-0.4	0.1	-0.4	0.8	0.7	1.4	1.8	51.4
Two-sides	G	0.2	-0.4	-0.5	2.7	1.5	4.9	5.8	
	GRCE	-0.2	0.1	-0.8	0.8	0.7	1.8	2.1	63.8
	GRCE(full)	-0.3	0.1	-0.4	0.9	0.7	1.5	1.9	67.2
Middle-belt	G	-0.2	0.4	0.2	2.2	2.9	4.5	5.8	
	GRCE	-0.1	0.1	-1.1	0.7	0.8	2.2	2.5	56.9
	GRCE(full)	-0.3	0.0	-0.6	0.9	0.7	1.4	1.8	69.0

2.4 Summary

GNSS signals are vulnerable to ambient perturbations. For current GPS-only deformation monitoring systems, high-accuracy positioning results are unattainable in some cases due to harsh environments that are often present in monitoring practice.

Using additional satellites can enhance spatial geometry. Therefore, understanding the improvements that will be introduced by using multi-GNSS observations becomes necessary. This study uses deformation monitoring as an example and presents several comparison experiments of relative positioning in real and simulated datasets. Experimental results confirm the advantages of multi-GNSS integration. Compared with the GPS-only approach, using existing additional constellations (i.e., GLONASS, BeiDou, and Galileo) increases the satellite availability globally by 280% and the value can increase to 340% in the foreseeable future when the four systems all reach their full constellations. Quad-GNSS integration can result in 52.4% reduction in PDOP at present, and 57.1% in the future compared to GPS alone scenarios. Deformation monitoring benefits from multiple GNSS observations, especially in challenging monitoring environments. The relative positioning results of a 4 m baseline imply that using quad-constellation data can reduce positioning errors by up to 52.4%. Improvements in positioning accuracy are also demonstrated in simulation experiments, in which the positioning errors decrease by 39.4–63.8% with the current four constellations. These indices increase to 48.5–69.0% when the constellations operate in their full status.

Chapter 3 Mitigation of systematic errors in multi-GNSS positioning based on semiparametric estimation

3.1 Motivation

Much research efforts have been put into the various problems in positioning with data from multiple GNSSs (Wang et al., 2001; Shi et al., 2013; Cai et al., 2014; Teunissen et al., 2014b; Li et al., 2015a), including refining the weighting schemes. However, less attention has been given to the impacts of systematic errors that can come from unmodeled atmospheric refraction, multipath signals, orbit error, and hardware delay (Schüler, 2006; Hoque and Jakowski, 2007; Wanninger, 2012; Dong et al., 2016). The conventional parametric estimation and variance component estimation (VCE) based on the least squares (LS) principle require that the observations are free from systematic errors. Therefore, when systematic errors are present, the quality of the solutions will be deteriorated (Xu et al., 2006; Teunissen and Amiri-Simkooei, 2008).

In GNSS data processing, four approaches have been employed to mitigate the systematic errors,

(1) Differencing and linear combinations of observables (Hofmann-Wellenhof et al., 2008; Leick et al., 2015). The approach cancels out the effects of common errors (e.g. clock errors) and reduces the effects of correlated or frequency-sensitive errors (e.g. tropospheric and ionospheric errors);
(2) Applying corrections based on empirical models and precise products (Satirapod et al., 2003; Meng et al., 2004; Kouba, 2015; Dong et al., 2016);
(3) Parameterization in the functional model (Paziewski and Wielgosz, 2015; Tian et al., 2015). For example, when GNSS receivers of different types are involved, additional parameters can be used to estimate the biases. Penalization parameters can be added when different GNSSs are not compatible (Yang et al., 2011); and

(4) Stochastic modeling (Wang et al., 2001; Schüler, 2006). Once the major parts of systematic errors have been removed, the remaining parts can be treated by stochastic modeling. In practice, approaches (3) and (4) are often used after applying approaches (1) and (2).

The abovementioned methods all have their limitations in mitigating the systematic errors. In (1), errors such as the higher-order ionospheric effects cannot be mitigated using linear combinations of observables (Hoque and Jakowski, 2007). The differencing approach becomes ineffective in removing the orbit errors and atmospheric refraction when the baselines are long, and the multipath errors even in short baselines (Schüler, 2006; Dong et al., 2016). For (2), apart from the problem of time delay in producing precise products (Kouba, 2015), systematic errors cannot be modeled accurately, especially when over-relying on residuals. In (3), parameterization is not always effective in estimating and mitigating the systematic errors due to problems of estimability and mismodeling. For (4), knowledge about the remaining systematic errors is usually insufficient to stochastically model them well.

Semiparametric estimation (SPE) model requires almost no a-priori knowledge about the effects and the statistical properties of systematic errors (Green and Silverman, 1994). It was introduced by Jia (2000) for mitigating GPS multipath. Various other systematic errors including atmospheric delays have since then also been studied using SPE (Jia et al., 2001; Alves, 2004; Durmaz and Karslioglu, 2015).

This study proposes to extend the SPE approach to multi-GNSS positioning. The application of SPE in double difference (DD) GNSS positioning will be discussed first, followed by a simulated GPS/BeiDou/GLONASS zero-baseline experiment and an example using a real GPS/BeiDou dataset over a short baseline affected by strong multipath signals, to demonstrate the advantages of the proposed method.

3.2 Impacts of systematic errors on multi-GNSS positioning

The linearized observation equation with systematic errors can be written as

$$\mathbf{L} = \mathbf{AX} + \mathbf{S} + \boldsymbol{\epsilon}, \quad E(\boldsymbol{\epsilon}) = \mathbf{0}, \quad D(\boldsymbol{\epsilon}) = \sigma^2 \mathbf{P}^{-1}, \tag{3-1}$$

where $\mathbf{L} \in \mathbb{R}^m$, $\mathbf{A} \in \mathbb{R}^{m \times t}$, $\mathbf{X} \in \mathbb{R}^t$, $\mathbf{S} \in \mathbb{R}^m$, $\boldsymbol{\epsilon} \in \mathbb{R}^m$, σ^2, $\mathbf{P} \in \mathbb{R}^{m \times m}$ are the observations, design matrix, unknown parameters, systematic errors, observation errors, variance factor and weight matrix, respectively; m and t are the number of observations and the number of parameters to be estimated respectively, with $m > t$; $E(\cdot)$ and $D(\cdot)$ respectively denote the expectation and dispersion operators. When $\mathbf{S} = \mathbf{0}$, Eq. (3-1) becomes the conventional parametric estimation model and can be resolved based on LS principle

$$\hat{\boldsymbol{\epsilon}}^{\mathrm{T}} \mathbf{P} \hat{\boldsymbol{\epsilon}} = \min \tag{3-2}$$

where $\hat{\boldsymbol{\epsilon}}$ is the vector of residuals. The LS solution can be expressed as

$$\begin{cases} \widehat{\mathbf{X}}_{\mathrm{LS}} = \mathbf{Q}_{\widehat{\mathbf{X}}_{\mathrm{LS}}} \mathbf{A}^{\mathrm{T}} \mathbf{P} \mathbf{L}, \quad \mathbf{Q}_{\widehat{\mathbf{X}}_{\mathrm{LS}}}^{-1} = \mathbf{N} = \mathbf{A}^{\mathrm{T}} \mathbf{P} \mathbf{A} \\ \hat{\boldsymbol{\epsilon}}_{\mathrm{LS}} = \mathbf{G} \mathbf{L}, \quad \mathbf{G} = \mathbf{I} - \mathbf{A} \mathbf{N}^{-1} \mathbf{A}^{\mathrm{T}} \mathbf{P} \end{cases} \tag{3-3}$$

where $\widehat{\mathbf{X}}_{\mathrm{LS}}$ is the LS estimation of the parameters with cofactor matrix $\mathbf{Q}_{\widehat{\mathbf{X}}_{\mathrm{LS}}}$; $\hat{\boldsymbol{\epsilon}}_{\mathrm{LS}}$ denotes the LS residuals; $\mathbf{I}$ is an identity matrix. If $\mathbf{S} \neq \mathbf{0}$, the LS solution has the following biases

$$\begin{cases} \mathbf{b}_{\widehat{\mathbf{X}}_{\mathrm{LS}}} = \mathbf{N}^{-1} \mathbf{A}^{\mathrm{T}} \mathbf{P} \mathbf{S} \\ \mathbf{b}_{\hat{\boldsymbol{\epsilon}}_{\mathrm{LS}}} = \mathbf{G} \mathbf{S} \end{cases} \tag{3-4}$$

where $\mathbf{b}_{\{\cdot\}}$ represents the estimation biases. Thus, when systematic errors exist, the LS is biased, and the estimated residuals are not random with zero mean.

Systematic errors can also impact on VCE that is based on the posteriori residuals (Xu et al., 2006). Considering that there are h types of observations in Eq. (3-1), i.e.,

$$\begin{cases} \underset{m \times 1}{\mathbf{L}} = \begin{Bmatrix} \mathbf{L}_i \\ m_i \times 1 \end{Bmatrix}, \quad i \in \{1, 2, \ldots, h\}, \\ D(\boldsymbol{\epsilon}_i) = \sigma_i^2 \mathbf{P}_i^{-1}, \quad \mathrm{Cov}(\boldsymbol{\epsilon}_i, \boldsymbol{\epsilon}_j) = \mathbf{0}, \quad (i \neq j) \end{cases} \tag{3-5}$$

where $\mathbf{L}_i$ is the ith subset with m_i observations, with weight matrix $\mathbf{P}_i$; σ_i^2 is the ith variance component to be estimated; $\mathrm{Cov}(\cdot)$ stands for the covariance operator. Here the observations from different subsets are assumed to be uncorrelated, leading to a

block-diagonal weight matrix $\mathbf{P}$. The following Helmert VCE has been frequently used for weight determination in such cases (Xu et al., 2006; Cai et al., 2014),

$$\begin{cases} \widehat{\boldsymbol{\theta}} = \boldsymbol{\Phi}^{-1}\boldsymbol{\Omega}, \quad \boldsymbol{\theta} = [\sigma_1^2, \quad \sigma_2^2, \quad \dots, \quad \sigma_h^2]^{\mathrm{T}}, \\ \boldsymbol{\Phi}(i,i) = m_i - 2\,tr(\mathbf{N}^{-1}\mathbf{N}_i) + tr(\mathbf{N}^{-1}\mathbf{N}_i\mathbf{N}^{-1}\mathbf{N}_i), \\ \boldsymbol{\Phi}(i,j) = tr(\mathbf{N}^{-1}\mathbf{N}_i\mathbf{N}^{-1}\mathbf{N}_j), \quad (i \neq j) \\ \mathbf{N} = \sum_{i=1}^{h} \mathbf{N}_i\,, \quad \mathbf{N}_i = \mathbf{A}_i^{\mathrm{T}}\mathbf{P}_i\mathbf{A}_i, \\ \boldsymbol{\Omega}(i) = \hat{\boldsymbol{\epsilon}}_i^{\mathrm{T}}\mathbf{P}_i\hat{\boldsymbol{\epsilon}}_i, \end{cases} \tag{3-6}$$

where $\boldsymbol{\theta}$ denotes the vector of h variance components to be estimated; and $tr(\cdot)$ is the matrix trace operator. VCE is carried out iteratively until the estimated variance factors converge. When systematic errors are present in the observations, inserting Eq. (3-4) into Eq. (3-6), one gets

$$\begin{cases} \mathbf{b}_{\Omega}(i) = \mathbf{S}^{\mathrm{T}}\mathbf{G}_i^{\mathrm{T}}\mathbf{P}_i\mathbf{G}_i\mathbf{S} \\ \mathbf{b}_{\hat{\theta}} = \boldsymbol{\Phi}^{-1}\mathbf{b}_{\Omega} \end{cases} \tag{3-7}$$

where $\mathbf{b}_{\Omega}$ and $\mathbf{b}_{\hat{\theta}}$ represent the biases in $\boldsymbol{\Omega}$ and $\widehat{\boldsymbol{\theta}}$, respectively; $\mathbf{G}_i$ denotes the rows in $\mathbf{G}$ (Eq. 3-3) corresponding to the ith subset of the observations. Apparently, $\boldsymbol{\Omega}$ is biased when systematic errors appear in the observations, resulting in biased variance components.

3.3 Semiparametric estimation (SPE)

3.3.1 SPE model

In surveying data processing, Eq. (3-1) has been frequently used as the functional model in SPE (Fischer and Hegland, 1999; Jia, 2000; Ding et al., 2015). The flexibility of the SPE model is due to its nonparametric components $\mathbf{S}$. However, since of these m additional unknowns, the SPE model cannot be resolved by LS directly. Instead, it can either be regularized to obtain a sub-optimal solution (Xu, 1998; Hu, 2005; Xu et al., 2006), or add realistic prior information from a Bayesian viewpoint to generate an optimal solution (Fischer and Hegland, 1999; Koch and Kusche, 2002; Ding et al.,

2015). The latter approach is not preferred when the true values of **S** are significantly different from zero (Xu and Rummel, 1994), although this is not considered a significant issue in GNSS relative positioning as the remaining systematic errors are in general close to zero after data pre-processing (e.g., differencing and applying corrections). For simplicity, the estimation is reduced to a generalized LS (GLS) problem (Menke, 2015), by using the prior information as pseudo-observations (**S** is considered deterministic)

$$\mathbf{CS} + \boldsymbol{\epsilon}_{\mathrm{c}} = \mathbf{0}, E(\boldsymbol{\epsilon}_{\mathrm{c}}) = \mathbf{0}, D(\boldsymbol{\epsilon}_{\mathrm{c}}) = \sigma^2 \mathbf{P}_{\mathrm{c}}^{-1}, \mathrm{Cov}(\boldsymbol{\epsilon}, \boldsymbol{\epsilon}_{\mathrm{c}}) = \mathbf{0} \tag{3-8}$$

where $\mathbf{C} \in \mathbb{R}^{u \times m}$, $\boldsymbol{\epsilon}_{\mathrm{c}} \in \mathbb{R}^{u}$ and $\mathbf{P}_{\mathrm{c}} \in \mathbb{R}^{u \times u}$ are, respectively, the design matrix, observation errors and weight matrix of the pseudo-observations, with $u > t$. The systematic errors are also usually assumed to be smooth. The smoothness can be controlled by applying a discrete differentiation technique, e.g., making the second differences of **S** small (Green and Silverman, 1994, p.76).

Combining the prior information of both smoothness and magnitude of **S** gives

$$\mathbf{C} = \begin{bmatrix} \mathbf{F}_{\mathrm{d}} \\ \mathbf{I} \end{bmatrix}, \text{where } \underset{(m-2)\times m}{\mathbf{F}_{\mathrm{d}}} = \mathrm{tridiag}(-0.5, 1, -0.5), \mathbf{P}_{\mathrm{c}} = \begin{bmatrix} \alpha \mathbf{P}_{\mathrm{d}} & \mathbf{0} \\ \mathbf{0} & \dfrac{\sigma^2}{\sigma_s^2}\mathbf{I} \end{bmatrix} \tag{3-9}$$

where $\mathbf{F}_{\mathrm{d}}$ is a second difference operator; α is a positive scalar called smoothing parameter; $\mathbf{P}_{\mathrm{d}}$ is a pre-given symmetric positive definite matrix, which is empirically designed as $\mathbf{P}_{\mathrm{d}}(i,i) = \mathbf{P}(i+1, i+1), i \in \{1,2,\dots,m-2\}$; and σ_s represents the magnitude values of **S**. Systematic errors of satellites with high elevations may be negligibly small and the corresponding parameters can be removed from the model by adjusting their σ_s to very small values. The magnitude prior information of **S** is sometimes necessary since uniquely solving Eq. (3-1) requires (Fischer and Hegland, 1999)

$$\mathrm{rank}(\mathbf{C}^{\mathrm{T}} \mathbf{P}_{\mathrm{c}} \mathbf{CA}) = t \tag{3-10}$$

In addition, the SPE model can become ill-posed due to over-parameterization and highly-correlated parameters. Using the magnitude pseudo-observations is also more straightforward in preventing the ill-posedness compared with techniques such as

truncated singular value decomposition and ridge regression (Xu, 1998; Hu, 2005). According to the GLS principle (Menke, 2015)

$$\hat{\boldsymbol{\epsilon}}^{\mathrm{T}}\mathbf{P}\hat{\boldsymbol{\epsilon}} + \hat{\boldsymbol{\epsilon}}_{\mathrm{c}}^{\mathrm{T}}\mathbf{P}_{\mathrm{c}}\hat{\boldsymbol{\epsilon}}_{\mathrm{c}} = \min \tag{3-11}$$

the GLS solution can be expressed as (Fischer and Hegland, 1999)

$$\begin{cases} \widehat{\mathbf{X}} = (\mathbf{A}^{\mathrm{T}}\mathbf{P}(\mathbf{I} - \mathbf{N}_{\mathrm{S}}^{-1}\mathbf{P})\mathbf{A})^{-1}\mathbf{A}^{\mathrm{T}}\mathbf{P}(\mathbf{I} - \mathbf{N}_{\mathrm{S}}^{-1}\mathbf{P})\mathbf{L} \\ \widehat{\mathbf{S}} = \mathbf{N}_{\mathrm{S}}^{-1}\mathbf{P}\left(\mathbf{L} - \mathbf{A}\widehat{\mathbf{X}}\right), \mathbf{N}_{\mathrm{S}} = \mathbf{P} + \mathbf{C}^{\mathrm{T}}\mathbf{P}_{\mathrm{c}}\mathbf{C} \\ \mathbf{Q}_{\widehat{\mathbf{X}}\widehat{\mathbf{X}}} = \mathbf{N}^{-1} + \mathbf{N}^{-1}\mathbf{A}^{\mathrm{T}}\mathbf{P}\mathbf{Q}_{\widehat{\mathbf{S}}\widehat{\mathbf{S}}}\mathbf{P}\mathbf{A}\mathbf{N}^{-1} \\ \mathbf{Q}_{\widehat{\mathbf{S}}\widehat{\mathbf{S}}} = (\mathbf{N}_{\mathrm{s}} - \mathbf{P}\mathbf{A}\mathbf{N}^{-1}\mathbf{A}^{\mathrm{T}}\mathbf{P})^{-1} \end{cases} \tag{3-12}$$

In order to know the condition when SPE can improve the estimation accuracy, the mean square error (MSE) performances of LS and GLS are compared as follows, considering Eqs. (3-3), (3-4) and (3-12),

$$\begin{aligned} MSE\left(\widehat{\mathbf{X}}_{\mathrm{LS}}\right) &= \sigma^2\, tr\left(\mathbf{Q}_{\hat{\mathbf{X}}_{\mathrm{LS}}}\right) + \mathbf{b}_{\hat{\mathbf{X}}_{\mathrm{LS}}}^{\mathrm{T}}\mathbf{b}_{\hat{\mathbf{X}}_{\mathrm{LS}}} \\ &= \sigma^2\, tr(\mathbf{N}^{-1}) + tr(\mathbf{N}^{-1}\mathbf{A}^{\mathrm{T}}\mathbf{P}\mathbf{S}\mathbf{S}^{\mathrm{T}}\mathbf{P}\mathbf{A}\mathbf{N}^{-1}) \end{aligned} \tag{3-13}$$

$$MSE\left(\widehat{\mathbf{X}}\right) = \sigma^2\, tr(\mathbf{Q}_{\widehat{\mathbf{X}}\widehat{\mathbf{X}}}) = \sigma^2\, tr(\mathbf{N}^{-1} + \mathbf{N}^{-1}\mathbf{A}^{\mathrm{T}}\mathbf{P}\mathbf{Q}_{\widehat{\mathbf{S}}\widehat{\mathbf{S}}}\mathbf{P}\mathbf{A}\mathbf{N}^{-1}) \tag{3-14}$$

$$\begin{aligned} &\text{if } MSE\left(\widehat{\mathbf{X}}_{\mathrm{LS}}\right) - MSE\left(\widehat{\mathbf{X}}\right) > 0, \\ &\text{i.e., } tr(\mathbf{N}^{-1}\mathbf{A}^{\mathrm{T}}\mathbf{P}(\mathbf{S}\mathbf{S}^{\mathrm{T}} - \sigma^2\mathbf{Q}_{\hat{\mathbf{S}}\hat{\mathbf{S}}})\mathbf{P}\mathbf{A}\mathbf{N}^{-1}) > 0 \end{aligned} \tag{3-15}$$

we obtain

$$\mathbf{S}^{\mathrm{T}}\mathbf{S} > \sigma^2 tr(\mathbf{Q}_{\hat{\mathbf{S}}\hat{\mathbf{S}}}) \tag{3-16}$$

It reveals that the rationale behind the linear model expansion exists when significant systematic errors present in the data.

3.3.2 Determination of smoothing parameters

For the purpose of choosing the smoothing parameter α, numerical methods such as L-curve (Hansen, 1992) and generalized cross-validation (GCV) (Golub et al., 1979) are widely used. L-curve method chooses the closest point to the origin, or the corner of an L-shaped curve consisting of norms of residuals and signals. This method has been reported to produce an over-smoothed solution (Xu, 1998; Kusche and Klees, 2002). GCV is a criterion minimizing the norm of residuals (Green and Silverman, 1994, p.71)

$$\begin{cases} \mathrm{GCV}(\alpha) = \dfrac{\hat{\boldsymbol{\epsilon}}^{\mathrm{T}}\mathbf{P}\hat{\boldsymbol{\epsilon}}}{[tr(\mathbf{G}_{\mathrm{s}})/m]^2} = \dfrac{\mathbf{L}^{\mathrm{T}}\mathbf{G}_{\mathrm{s}}^{\mathrm{T}}\mathbf{P}\mathbf{G}_{\mathrm{s}}\mathbf{L}}{[tr(\mathbf{G}_{\mathrm{s}})/m]^2} \\ \mathbf{G}_{\mathrm{s}} = \mathbf{I} - (\mathbf{I} - \mathbf{N}_{\mathrm{s}}^{-1}\mathbf{P})\mathbf{A}(\mathbf{A}^{\mathrm{T}}\mathbf{P}_{\mathrm{r}}\mathbf{A})^{-1}\mathbf{A}^{\mathrm{T}}\mathbf{P}_{\mathrm{r}} - \mathbf{N}_{\mathrm{s}}^{-1}\mathbf{P} \\ \mathbf{P}_{\mathrm{r}} = \mathbf{P}(\mathbf{I} - \mathbf{N}_{\mathrm{s}}^{-1}\mathbf{P}) \end{cases} \tag{3-17}$$

However, the determination of the smoothing parameter using GCV and L-curve is time-consuming (Kusche and Klees, 2002; Satirapod et al., 2003).

The smoothing parameter α can also be interpreted as a weight ratio (Koch and Kusche, 2002) and estimated through the VCE. The following simplified procedure is proposed for enhancing the computation efficiency in determining the smoothing parameter based on the LS residuals (the conventional LS solution is derived beforehand):

Step (a). Estimate the approximate variances based on LS residuals (Appendix B provides more details, $\mathbf{P}_{\mathrm{d}}(i,i) = \mathbf{P}(i+1, i+1), i \in \{1,2,\dots,m-2\}$ is empirically adopted),

$$\begin{cases} \hat{\boldsymbol{\epsilon}}_{\mathrm{d}} = \mathbf{F}_{\mathrm{d}}\hat{\mathbf{S}} \approx \mathbf{F}_{\mathrm{d}}\mathbf{F}_{\mathrm{L}}\hat{\boldsymbol{\epsilon}}_{\mathrm{LS}}, \quad \hat{\boldsymbol{\epsilon}} \approx \mathbf{F}_{\mathrm{H}}\hat{\boldsymbol{\epsilon}}_{\mathrm{LS}} \\ \hat{\sigma}_{\mathrm{d}}^2 \approx \gamma_{\mathrm{d}}\dfrac{\hat{\boldsymbol{\epsilon}}_{\mathrm{d}}^{\mathrm{T}}\hat{\boldsymbol{\epsilon}}_{\mathrm{d}}}{m-2} \approx \gamma_{\mathrm{d}}\dfrac{\hat{\boldsymbol{\epsilon}}_{\mathrm{LS}}^{\mathrm{T}}\mathbf{F}_{\mathrm{L}}^{\mathrm{T}}\mathbf{F}_{\mathrm{d}}^{\mathrm{T}}\mathbf{F}_{\mathrm{d}}\ \mathbf{F}_{\mathrm{L}}\ \hat{\boldsymbol{\epsilon}}_{\mathrm{LS}}}{m-2} \\ \hat{\sigma}^2 \approx \gamma\dfrac{\hat{\boldsymbol{\epsilon}}^{\mathrm{T}}\hat{\boldsymbol{\epsilon}}}{m-1} \approx \gamma\dfrac{\hat{\boldsymbol{\epsilon}}_{\mathrm{LS}}^{\mathrm{T}}\mathbf{F}_{\mathrm{H}}^{\mathrm{T}}\mathbf{F}_{\mathrm{H}}\ \hat{\boldsymbol{\epsilon}}_{\mathrm{LS}}}{m-1} \end{cases} \tag{3-18}$$

where $\mathbf{F}_{\mathrm{L}} \in \mathbb{R}^{m\times m}$ and $\mathbf{F}_{\mathrm{H}} \in \mathbb{R}^{(m-1)\times m}$ are the low-pass and high-pass filter operation matrices given in (B-2) and (B-5) respectively; γ and γ_{d} are positive scalars that represent the errors in $\hat{\sigma}_{\mathrm{d}}$ and $\hat{\sigma}$ caused by the simplification of the weight matrix respectively.

Step (b). Finally, assuming $\gamma \approx \gamma_{\mathrm{d}}$, the approximate calculation formula of the smoothing parameter is

$$\hat{\alpha} = \frac{\hat{\sigma}^2}{\hat{\sigma}_{\mathrm{d}}^2} \approx \frac{m-2}{m-1}\frac{\hat{\boldsymbol{\epsilon}}_{\mathrm{LS}}^{\mathrm{T}}\mathbf{F}_{\mathrm{H}}^{\mathrm{T}}\mathbf{F}_{\mathrm{H}}\ \hat{\boldsymbol{\epsilon}}_{\mathrm{LS}}}{\hat{\boldsymbol{\epsilon}}_{\mathrm{LS}}^{\mathrm{T}}\mathbf{F}_{\mathrm{L}}^{\mathrm{T}}\mathbf{F}_{\mathrm{d}}^{\mathrm{T}}\mathbf{F}_{\mathrm{d}}\ \mathbf{F}_{\mathrm{L}}\ \hat{\boldsymbol{\epsilon}}_{\mathrm{LS}}} \tag{3-19}$$

3.3.3 Hypothesis test for systematic errors

In addition to applying pseudo-observations in tackling the problems of ill-posedness and rank-deficiency of the SPE, since a trade-off between the model expansion and estimation accuracy is required, fictitious parameters should be avoided (Kotsakis, 2005). This can be realized through hypothesis testing the significance of the systematic errors, using techniques such as model validations (Teunissen, 1998; Leick et al., 2015) and Durbin-Watson method (Jia et al., 2002). If no significant systematic error is detected, the corresponding nonparametric terms can be eliminated, or equivalently, fix s to zero and set α to a relatively large value (e.g. 10^{15} in our experiments). To simplify the computation required, the following procedure is adopted to directly detect systematic errors related to individual satellites based on LS residuals only (outliers have been pre-screened). The null and alternative hypotheses are given as

$$\mathbf{H}_0: E(\hat{\sigma}_{\mathrm{a}}^2) = E(\hat{\sigma}_{\mathrm{r}}^2) \quad \text{against} \quad \mathbf{H}_1: E(\hat{\sigma}_{\mathrm{a}}^2) < E(\hat{\sigma}_{\mathrm{r}}^2) \tag{3-20}$$

where $\hat{\sigma}_{\mathrm{a}}^2 = \frac{1}{2(m-1)}\sum_{i=1}^{m-1}(\epsilon_{i+1} - \epsilon_i)^2$, and $\hat{\sigma}_{\mathrm{r}}^2 = \frac{1}{m}\sum_{i=1}^{m}\epsilon_i^2$. The ratio between these two variables satisfies the following distribution when there are enough samples (e.g. $m > 20$) (Zar, 2010, p.601),

$$\frac{\hat{\sigma}_{\mathrm{a}}^2}{\hat{\sigma}_{\mathrm{r}}^2} \sim \mathrm{N}\left(1, \frac{1}{m+1}\right) \tag{3-21}$$

A Z-test statistic thus is formed as

$$z = \sqrt{m+1}\left(1 - \frac{\hat{\sigma}_{\mathrm{a}}^2}{\hat{\sigma}_{\mathrm{r}}^2}\right) \sim \mathrm{N}(0,1) \tag{3-22}$$

The rejection region is $z > z_{0.99}$ (a critical value of standard normal distribution with significance level 0.01). It helps to reduce the risk of introducing too many unknown parameters when modeling the systematic errors.

3.4 Processing multi-GNSS data with SPE

A multi-GNSS double-difference (DD) carrier phase observation can be expressed as (Wang et al., 2001)

$$L_{ab}^{ij}(k) = \rho_{ab}^{ij}(k) + \lambda^i N_{ab}^{ij} + (\lambda^i - \lambda^j) N_{ab}^{j} + \varepsilon_{ab}^{ij}(k) \tag{3-23}$$

where $L_{ab}^{ij}(k)$ is the DD carrier phase (scaled to meters) of site pair a-b and satellite pair i-j at epoch k; j indicates the reference satellite; ρ is the geometric distance; λ is the wavelength; N is the phase ambiguity, including DD ambiguity N_{ab}^{ij}, and single-difference (SD) ambiguity N_{ab}^{j} that cannot be canceled in multi-frequency case. In ambiguity resolution, pseudoranges are used to calculate the approximate SD ambiguities, which will be eventually determined when fixing the DD ambiguities; ε is the observation error.

A term of systematic errors will be added to the basic DD observation Eq. (3-23). Since model errors will be partially absorbed by the float ambiguities (Wang et al., 2001), it is necessary to remove the systematic errors before fixing the ambiguities to get float ambiguities closer to integers. The extended DD observation equation therefore becomes

$$L_{ab}^{ij}(k) = \rho_{ab}^{ij}(k) + \lambda^i N_{ab}^{ij} + (\lambda^i - \lambda^j) N_{ab}^{j} + s_{ab}^{ij}(k) + \varepsilon_{ab}^{ij}(k) \tag{3-24}$$

where s is the compensation parameter that depends on the satellite, site and time.

GNSS data processing requires vector semiparametric models (Fessler, 1991; Jia, 2000) since the observations contain a set of satellites. Assuming that n_{sat} satellites have been simultaneously tracked for m epochs, and denoting n_{ref} as the number of reference satellites and n as the number of smoothing parameters ($n = n_{\mathrm{sat}} - n_{\mathrm{ref}}$, a reference satellite is selected for each satellite system), additional $m \times n$ compensation parameters need to be estimated. The criterion in (3-8) is extended into

$$\begin{cases} \sum_{k=1}^{m} \underset{1\times n}{\hat{\boldsymbol{\epsilon}}_k^{\mathrm{T}}} \mathbf{P}_k \hat{\boldsymbol{\epsilon}}_k + \underset{1\times mn}{\hat{\overline{\mathbf{S}}}^{\mathrm{T}}} \overline{\mathbf{C}}^{\mathrm{T}} \overline{\mathbf{P}}_{\mathrm{c}} \overline{\mathbf{C}} \hat{\overline{\mathbf{S}}} = \min \\ \underset{mn\times 1}{\overline{\mathbf{S}}} = \left\{ \underset{n\times 1}{\mathbf{S}_k} \right\}, \quad k \in \{1,2,\dots,m\} \\ \underset{un\times mn}{\overline{\mathbf{C}}} = \underset{u\times m}{\mathbf{C}} \otimes \underset{n\times n}{\overline{\alpha}^{\frac{1}{2}}} \\ \overline{\mathbf{P}}_{\mathrm{c}} = \mathrm{blockdiag}(\mathbf{P}_{\mathrm{c},1}, \mathbf{P}_{\mathrm{c},2}, \cdots, \mathbf{P}_{\mathrm{c},m}) \\ \overline{\alpha} = \mathrm{diag}(\alpha_1, \alpha_2, \cdots, \alpha_n) \end{cases} \tag{3-25}$$

where m and n are the number of observation epochs and the number of smoothing parameters respectively; u, $\mathbf{C}$ and $\mathbf{P}_{c,k}$ are respectively the number, design matrix and weight matrix of the pseudo-observations defined in Eq. (3-9); k is the epoch index; $\otimes$ denotes the Kronecker operator.

3.5 Experiments and results

Two experiments (one with simulated and one with real multiple GNSS data) are carried out to investigate the performance of the proposed SPE approach when combined with VCE in processing the GNSS data. For simplicity, the combined use of SPE and VCE will be referred to hereafter as semiparameter and variance estimation (SVE). For comparison, conventional LS estimation and VCE based on results from the conventional LS are also carried out. In the conventional LS estimation, the inter-system weight ratios are set equal to 1. The SPE is carried out before the VCE. A smoothing parameter is added for each satellite pair and adjusted individually based on Eq. (3-19). SVE is applied in both float and ambiguity fixed solutions.

The results are evaluated with the aforementioned Z test and the following baseline quality indicators (Blewitt, 1989)

$$\text{Length error} = (\delta_N^2 + \delta_E^2 + \delta_U^2)^{1/2} \tag{3-26}$$

$$\text{Repeatability } (\delta) = \left(\frac{\sum_i^{n_s} \delta_i^2 / \sigma_{\delta_i}^2}{\sum_i^{n_s} 1/\sigma_{\delta_i}^2} \right)^{1/2} \tag{3-27}$$

where δ stands for baseline errors with respect to the truths, with subscripts *N*, *E* and *U* denoting the corresponding north, east and up coordinate components; i indicates the session number (n_s in total); and σ_δ is the standard deviation (STD) of δ.

LAMBDA (Teunissen, 1995) is used in all the above three methods for ambiguity resolution with R-ratio as the validation indicator (Euler and Schaffrin, 1991). The computer time is recorded to assess the computation efficiency. Different SVEs are carried out, including those based on the traditional iterative and search methods

discussed above, i.e., the VCE and GCV (with and without magnitude prior information where the latter is referred to as *GCV-free*). The Golden Section technique (Press et al., 2007) is applied in the search process of GCV (in the range from 10^{-15} to 10^{15}). Note that the GCV-free-based SVE is used only in the fixed-ambiguity solution, since criterion in Eq. (3-10) is violated when the design matrix $\mathbf{A}$ is based on (3-24), and (3-9) only contains the smoothness of $\mathbf{S}$ (i.e. $\mathbf{C} = \mathbf{F}_{\mathrm{d}}$ and $\mathbf{P}_{\mathrm{c}} = \alpha\mathbf{P}_{\mathrm{d}}$). Initial values of the smoothing parameters in the VCE-based SVE are specified by the approximate formula (3-19) to accelerate the convergence.

3.5.1 A simulated experiment

Sinusoidal systematic errors (in cycles) are simulated using Eq. (3-28) and added to the raw GNSS observations of a zero baseline. The session length is 3h with a data sampling interval of 90 s (a relatively large interval being used to reduce the computation load). A cut-off angle of 10 degree is used. The dataset contains L1/B1/G1 observations from 9/9/7 satellites of G/C/R (hereafter G, C, and R stand for GPS, BeiDou and GLONASS respectively). The systematic errors simulated have different periods (1.5h for G12, 2.5h for both G22 and C02) but the same amplitudes (0.05 cycles, considering the general phase noise (Leick et al., 2015, p. 420) and the error level of the zero-baseline used),

$$\begin{cases} \mathrm{G12}: 0.05\sin(\dfrac{tow}{1.5\times 3600}2\pi) \\ \mathrm{G22}: 0.05\sin(\dfrac{tow}{2.5\times 3600}2\pi) \\ \mathrm{C02}: 0.05\sin(\dfrac{tow}{2.5\times 3600}2\pi)+0.10 \end{cases} \tag{3-28}$$

where tow is time of week in seconds. A constant offset of 0.1 cycles is also added to C02. When applying the SPE in this experiment, the constraints for the systematic errors are set as 0.2 cycles (a relatively loose constraint to avoid possible distortion of the results), i.e., $\sigma_{\mathrm{s}} = 0.2 \times \mathrm{wavelength}$ in Eq. (3-21).

Figure 3-1 shows length errors of the baseline from the different estimators. The simulated systematic errors have introduced nearly up to 7 mm length error to the zero-baseline. The VCE method then reduces this discrepancy to 3 mm through raising

GLONASS's weight from 1.0 to 2.9 (see Table 3-1), while this improvement is achieved at the cost of roughly down-weighting the observations from all the other satellites, both GPS and BeiDou, including those without systematic errors. Compared with the results of VCE that based on raw data (see Table 3-2), apparently the weight ratios are seriously falsified as the Z test statistics are all increased. The SVE approach has significantly reduced the length error to about 0.5 mm (over 90% improvement compared with LS and over 80% compared with VCE) and improved the R-ratio from 16.4 to 58.5, indicating a much more reliable solution. The weight ratios obtained by SVE are closer to those obtained based on the raw data without systematic errors.

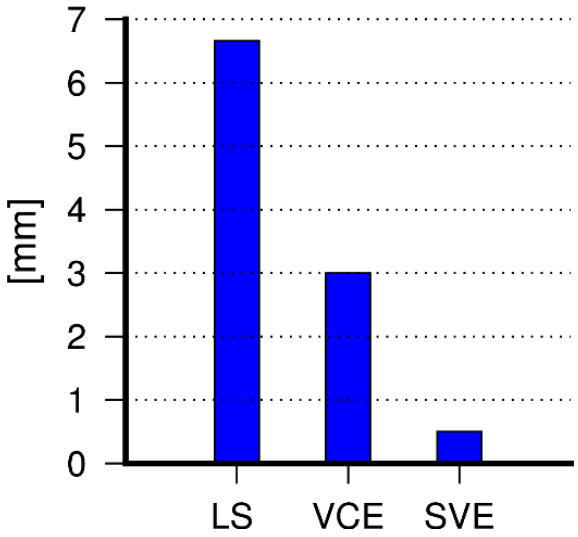

Figure 3-1 Baseline length errors from different estimators (session length: 3h)

Table 3-1 Solutions of zero baseline with simulated systematic errors from different estimators (session length: 3h)

	LS	VCE	SVE
Baseline bias (X/Y/Z) [mm]	-4.6/3.2/3.6	-1.8/1.8/1.6	-0.4/0.0/0.3
Weight ratio (G/C/R)	1.0/1.0/1.0	1.0/0.4/2.9	1.0/0.4/0.7
R-ratio	16.4	16.4	58.5
Z test : G12-G18	10.0	10.0	-0.4*
Z test : G22-G18	9.8	9.8	-2.2*
Z test : C02-C07	10.8	10.8	-1.0*

*Residuals that passed the Z test (significance level 0.01)

Table 3-2 Solutions of zero baseline without simulated systematic errors from traditional different estimators (session length: 3h)

	LS	VCE
Baseline bias (X/Y/Z) [mm]	-0.2/0.6/0.2	-0.1/0.4/-0.1
Weight ratio (G/C/R)	1.0/1.0/1.0	1.0/0.5/0.6
R-ratio	>1000.0	>1000.0
Z test : G12-G18	1.6*	1.6*
Z test : G22-G18	-0.3*	-0.3*
Z test : C02-C07	-0.1*	-0.1*

*Residuals that passed the Z test (significance level 0.01)

Figure 3-2 shows the residuals from the different solutions. LS and VCE do not cope with the systematic errors well. The SVE models much better the systematic errors and the residuals become more random, all the residuals have finally passed the Z test (see Table 3-1). According to the Z test results, SVE works better with low-frequency systematic errors than high-frequency errors. The LS residuals may appear very inconsistent, particularly in Figure 3-2c where an offset clearly exists between them.

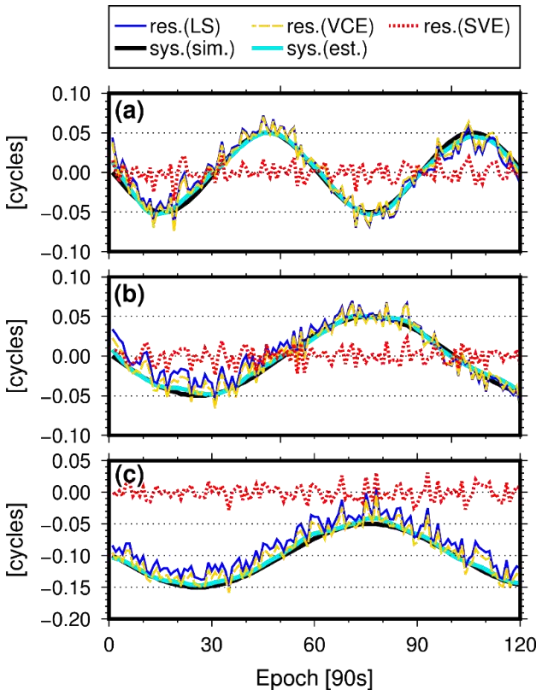

Figure 3-2 Residuals of (a) G12-G18, (b) G22-G18, (c) C02-C07 estimated by the different estimators, and systematic errors simulated and estimated by SVE (observation session length: 3h)

To understand the performance when using different SVEs, the results of different session lengths (from 0.5 h to 3.0 h, increasing 0.5 h gradually) are compared. As shown in Figure 3-3, the baseline accuracy obtained by the simplified approach is similar to those obtained based on VCE and GCV, and they are superior to those using the GCV-free method. The advantage of adding prior information on the magnitude of the systematic errors is more evident in sessions of shorter lengths (with weaker model strength), where the results based on GCV-free approach are dramatically deteriorated. The time consumption of the GCV-based SVEs raises exponentially as the session length increases. The VCE-based SVE reduces the mean calculation time from about 9 h to less than 3 h (see Table 3-3), while the simplified approach further shortens it by almost 30 times to about 0.1h. These results indicate that compared with conventional search and iterative algorithms, the simplified approach can achieve comparable baseline solutions with a considerably higher efficiency.

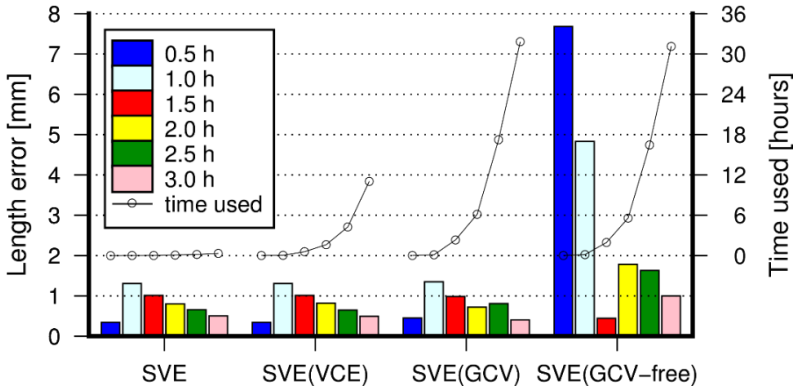

Figure 3-3 Baseline length errors from different semiparametric estimators and different observation session lengths

Table 3-3 Solutions of the simulated zero-baseline and systematic errors from different semiparametric estimators (session lengths: 0.5, 1.0, 1.5, ..., 3.0h)

Mean value	SVE	SVE (VCE)	SVE (GCV)	SVE (GCV-free)
Length error [mm]	0.8	0.8	0.8	2.9
R-ratio	36.3	36.2	23.3	9.4
Time used[a] [h]	0.1	2.9	9.6	9.2

[a] Configuration of PC: 64-bit Windows 7 with IntelXeon E5-1660v3 CPU of 3.0 GHz and memory of 16 GB

3.5.2 Experiments with real datasets

The multi-GNSS dataset consists of GPS/BeiDou single frequency (L1/B1) observations covering three consecutive days (DOYs 320–322 in 2014). It is from a baseline of about 10 m on the roof of Wenfa Building at The Central South University, China. The points are referred to as CSUA and CSUB, respectively. A reflective environment was created by placing tinfoil paper on the north wall near site CSUA, and therefore, the multipath signals are considered strong (Figure 3-4). The observations were divided equally into 24 sessions, and each session was sampled at 90 s to reduce the computation load. Observations below elevation angle of 10 degree were not used. The baseline components are estimated based on all the GPS data and used as the truths in evaluating the performances of the methods. In SPE, the systematic errors are empirically constrained to be within 0.15 cycles (three times as large as the normal amplitude of DD residuals in short baselines, i.e. 0.05 cycles).

Figure 3-4 Observation sites at CSUA (upper right diagram) and CSUB (lower right diagram); Tinfoil paper was placed on the north wall near site CSUA to enhance the signal reflection

Figure 3-5 shows the sky plots and signal strengths. The satellite signals (especially GPS) from the north direction were blocked significantly and have much lower signal

strength. BeiDou system contributes more to both the number of the satellites and the signal quality (Figure 3-5b).

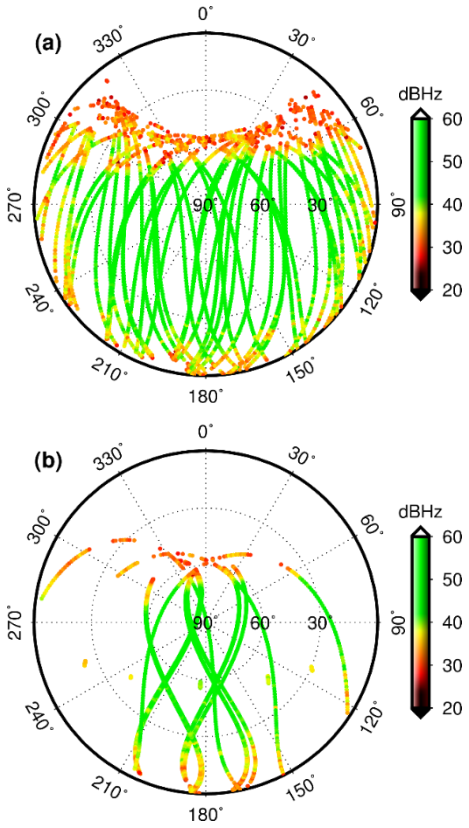

Figure 3-5 Sky plots and C/N_0 signal strengths of (a) GPS satellites and (b) BeiDou satellites at site CSUA on DOY 320, 2014

Figure 3-6 illustrates the time series of L1/B1 C/A code multipath combination (Shi et al., 2013) from data of different types of satellite. As the multipath signals increase with descending elevations, the Median Earth Orbit (MEO) G31 (Figure 3-6a) with a bell-shaped elevation pattern has larger multipath effect at the two ends. The effect becomes smaller at the two peak elevations of the camelback-shaped Inclined Geosynchronous Orbit (IGSO) C10 (Figure 3-6b). The elevation of the Geosynchronous Orbit (GEO) C05 (Figure 3-6c) varies slowly in a sinusoidal pattern and its multipath effects were more stable compared with those of the MEO and IGSO. Signals from GEO presented a higher continuity as it stayed on the southern sky, those from MEO and IGSO were partially shadowed by the northern wall (Figure 3-4) when they traveled to the back side (during the hours of about 14–17 for G31, and about

15–19 for C10 respectively). More frequent and larger multipath errors can be seen near about 60° elevation when the satellites were nearly blocked.

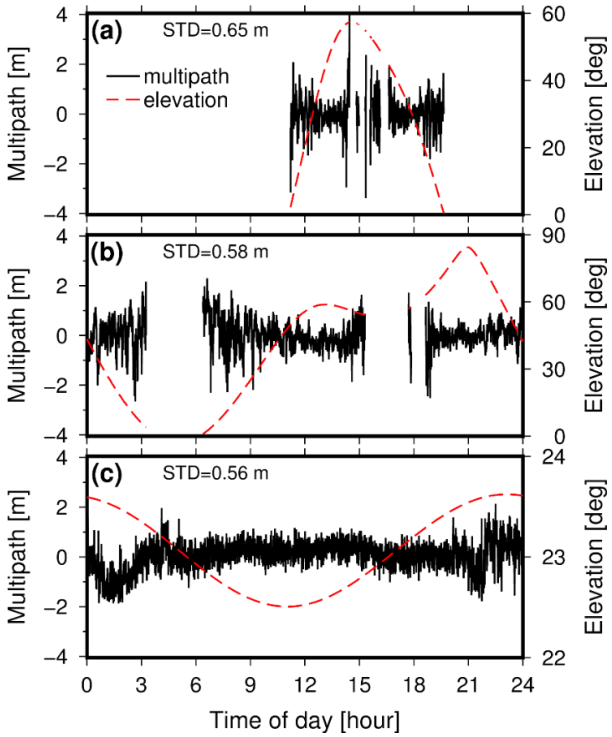

Figure 3-6 L1/B1 C/A code multipath vs. elevations of (a) MEO G31, (b) IGSO C10, (c) GEO C05 satellites at site CSUA on DOY 320, 2014; the signals of G31 and C10 were blocked by the north wall near the site during the hours of about 14-19

Figure 3-7 shows the length errors of the baseline from the different processing methods. It can be seen that compared with LS method, the VCE approach has produced lower baseline errors in 14 out of 24 of the observation sessions. As shown in Table 3-4, the length repeatability is improved by 19.4% by the VCE approach as BeiDou's mean weight is increased by 4.1 times. The SVE solution has further improved the length repeatability by 35.6% when adjusting BeiDou's mean weight to 1.8. For both VCE and SVE, significant improvements can be seen in the north and vertical directions, while the repeatability of the east component is lowered slightly by the SVE approach. The R-ratios are improved by using the SVE approach in the ambiguity resolution.

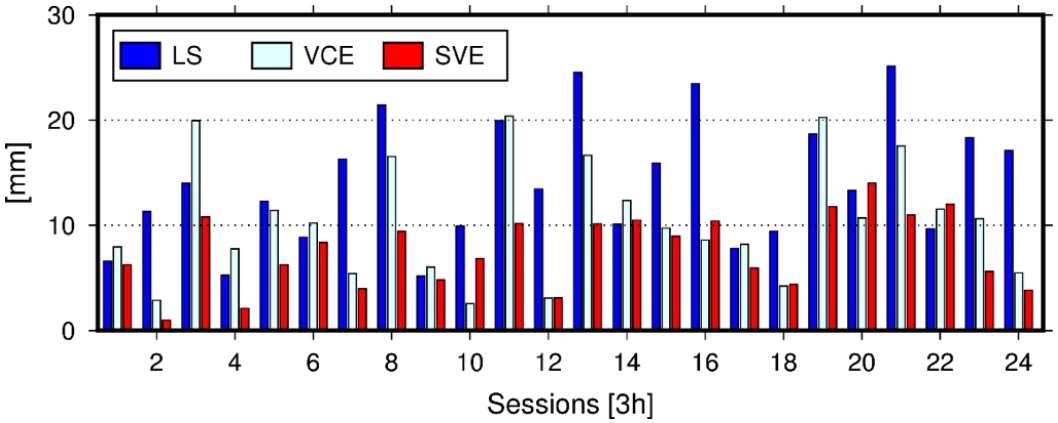

Figure 3-7 Baseline length errors of different observation sessions and from different estimators

The VCE-based SVE approach has produced similar baseline solutions as those of the simplified approach, with the differences between the baseline components being smaller than 0.1 mm. The results are superior to those produced by GCV-based SVE. Results from GCV-free SVE are not presented here due to its unsatisfactory performance (see Sect. 3.5.1). A great advantage of the proposed simplified approach is in its high computation efficiency. The average computation time (see Table 3-4 for the configuration of the PC used) used for a baseline solution (session length is 3h) is 0.1h, over 20 times faster than the VCE-based SVE, and over 100 times faster than the GCV-based SVE.

Table 3-4 Solutions of real GNSS dataset from different estimators (3 h×24 sessions)

	LS	VCE	SVE	SVE (VCE)	SVE (GCV)
Repeatability, North [mm]	9.6	7.1	5.5	5.5	5.7
Repeatability, East [mm]	1.2	0.9	1.4	1.4	1.4
Repeatability, Up [mm]	8.9	7.9	6.3	6.4	6.9
Repeatability, baseline length [mm]	12.9	10.4	8.3	8.3	8.8
Impr. over LS (baseline length) [%]	-	19.4	35.6	35.6	31.5
Mean weight ratio (BeiDou/GPS)	1.0	4.1	1.8	1.6	1.0
Mean R-ratio	12.1	12.1	20.1	20.1	17.4
Mean time used[a]	2.2 s	2.3 s	0.1 h	2.2 h	10.5 h

[a] Configuration of PC: 64-bit Windows 7 with IntelXeon E5-1660v3 CPU of 3.0 GHz and memory of 16 GB

The 5-th session is selected to show some further details of the results. The number of satellites in view is relatively less in this session, and there appear apparently some systematic errors in the GNSS observations. The DD residuals from the LS and the SVE solutions as well as the systematic errors estimated from the SVE solution are shown in Figure 3-8, and some statistics of the residuals are given in Figure 3-9. The residuals from standard LS and VCE approaches are not presented here as they cannot resist the systematic errors so that the results are not very satisfactory. From the residuals shown in Figure 3-8a, it is apparent that there exist some significant systematic errors varying over time. For example, residuals from G31-G22 and C10-C03 satellite pairs fluctuated obviously over time, and those from C05-C03 are fairly constant. After the SVE approach is applied, systematic errors in the LS residuals have been accurately estimated (Figure 3-8b) and removed. Therefore, residuals from the SVE solution appear much more random (Figure 3-8c), with both the biases and the STDs being significantly reduced (see Figure 3-9). The results clearly indicate that the proposed SPE approach is effective in mitigating the systematic errors and that the application of the approach can significantly improve the results of VCE.

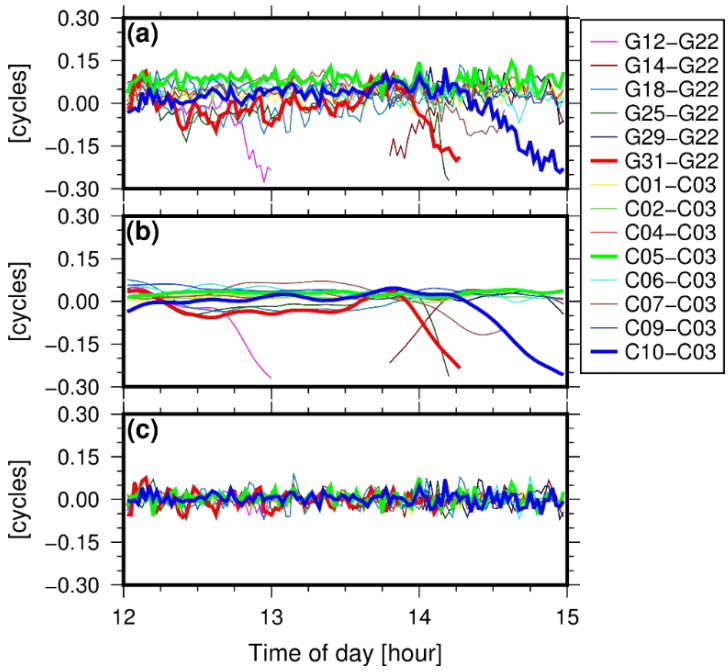

Figure 3-8 DD L1/B1, (a) Residuals from LS, (b) estimated systematic errors from SVE, (c) residuals from SVE of the 5-th session

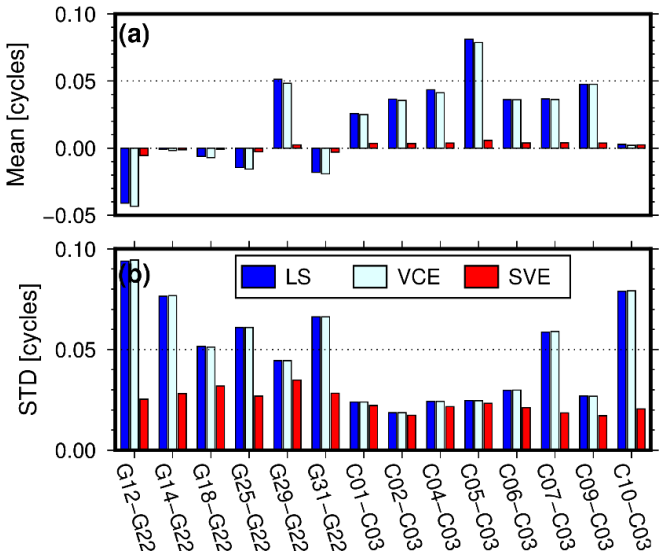

Figure 3-9 (a) Means, (b) STDs of DD L1/B1 residuals of the 5-th session

Three typical satellites of different orbits (i.e. MEO, IGSO, GEO) are selected to assess the performances of SVE and LS. The residuals from the experiments are given in Figure 3-10, and the corresponding Z test statistics and the smoothing parameters (both from float and fixed-ambiguity solutions) from the SVE are given in Table 3-5. By extracting the systematic errors, the mean of the residuals becomes much closer to zero and the histogram of the residuals is more concentrated around the center. Similar improvements can be seen in the results of the Z test where the test statistics decrease significantly and the residuals of most of the satellite pairs pass the test. In addition, systematic errors with larger magnitudes are generally penalized with smaller smoothing parameters (when using the z statistic as an indicator in the analysis, the numbers of the observations should be similar). The smoothing parameters of the float-ambiguity solution are similar to those from the fixed-ambiguity solution except those set to large values since their residuals from the float solution pass the Z test. For some satellite pairs (e.g. G31-G22 in Figure 3-10a), the high-frequency systematic errors remain although the magnitudes are small. There are apparent inconsistencies between the estimated systematic errors and the LS-derived residuals (e.g. C05-C03 in Figure 3-10c). This indicates that (see also Figure 3-2c), it is sometimes not appropriate to determine the systematic errors based on the residuals only.

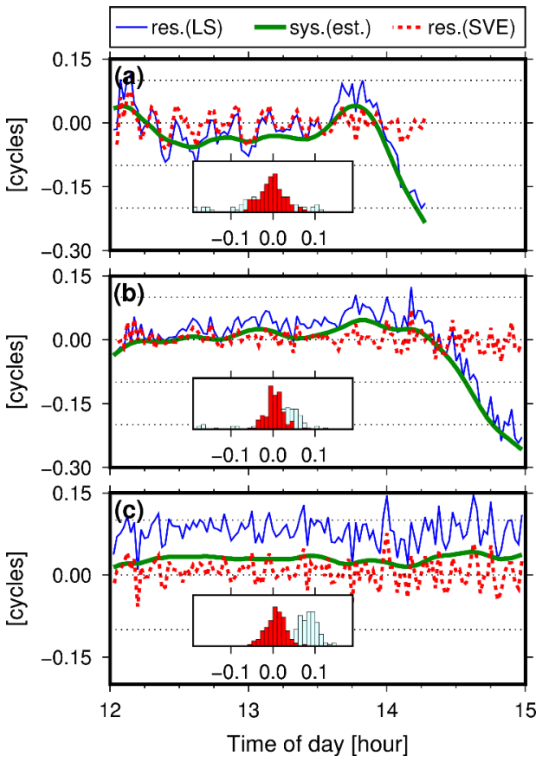

Figure 3-10. DD L1/B1 residuals of the 5-th session, satellite pairs (a) G31-G22, (b) C10-C03 and (c) C05-C03 before and after extraction of systematic errors

Table 3-5 Z test results and SPE-derived smoothing parameters (the 5th session)

Satellite pairs	# of epochs	Z test		$\hat{\alpha}$ (float solution)	$\hat{\alpha}$
		LS	SVE		
G12-G22	40	6.1	2.5	218.2	215.7
G14-G22	48	6.1	1.0*	373.8	374.2
G18-G22	99	7.2	3.0	215.1	214.7
G25-G22	88	7.9	2.6	179.8	179.3
G29-G22	40	4.9	1.0*	319.2	322.1
G31-G22	91	8.6	4.1	278.1	278.6
C01-C03	119	6.3	-0.3*	10^{15}	437.9
C02-C03	119	8.9	-0.1*	10^{15}	343.8
C04-C03	119	8.9	0.5*	10^{15}	269.7
C05-C03	119	10.1	0.3*	10^{15}	341.2
C06-C03	119	9.0	2.0*	230.5	230.2
C07-C03	103	9.5	1.0*	357.2	357.9
C09-C03	119	9.9	0.4*	397.1	396.7
C10-C03	119	10.1	-0.4*	335.8	335.8

*Residuals that passed the Z test (significance level 0.01)

To investigate the stability of the proposed method, the estimation results of the three satellite pairs in the same time period in the following two days, i.e. the 13-th and 31-th sessions, are also selected and presented in Figure 3-11. Evident sidereal repeatability of the multipath errors can be seen. The multipath patterns of the satellite pairs are similar with those presented in the first day (see the 5-th session in Figure 3-10).

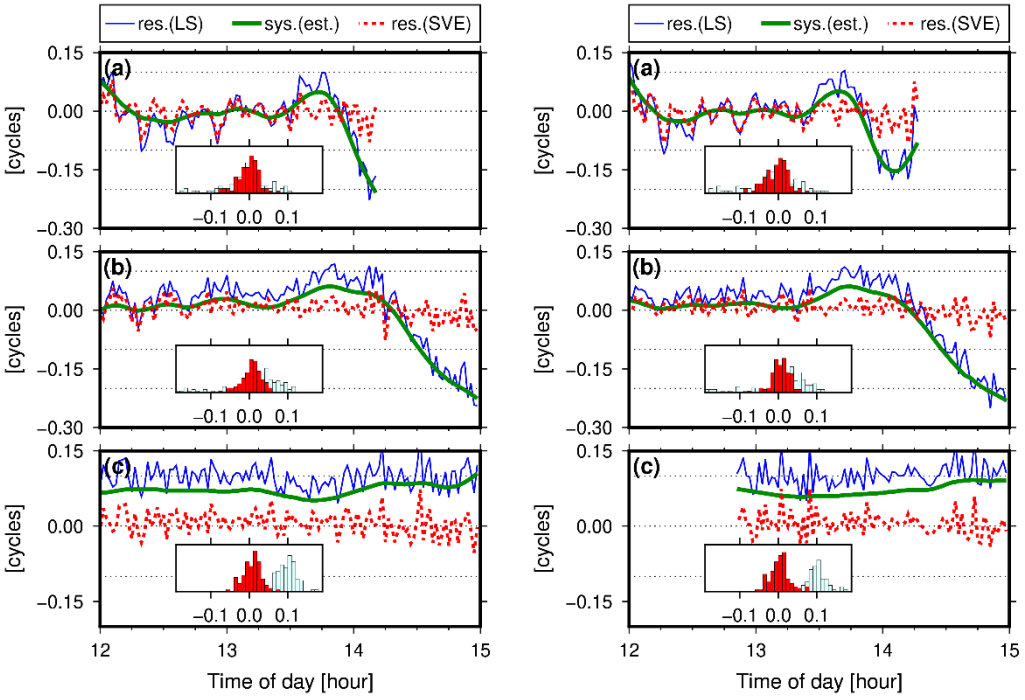

Figure 3-11 DD L1/B1 residuals of the 13-th session (left) and the 21-th session (right), satellite pairs (a) G31-G22, (b) C10-C03 and (c) C05-C03 before and after extraction of systematic errors

Figure 3-12 compares the estimated systematic errors from the three consecutive days. Estimation results of G31-G22 and C10-C03 show a good agreement between different days, while some small offsets exist in the results of the GEO satellite pair C05-C03, and obvious shifts present in the non-GEO satellite pairs G31-G22 and C10-C03. The differences may be caused by the between-day changes of the satellite geometry and inaccurate priori information used. Despite the small changes, the high repeatability of the estimated systematic errors confirms the stability of the proposed method in extracting the systematic errors. It is also encouraging to consider the

possibility of applying the derived systematic errors as corrections to the subsequent observations.

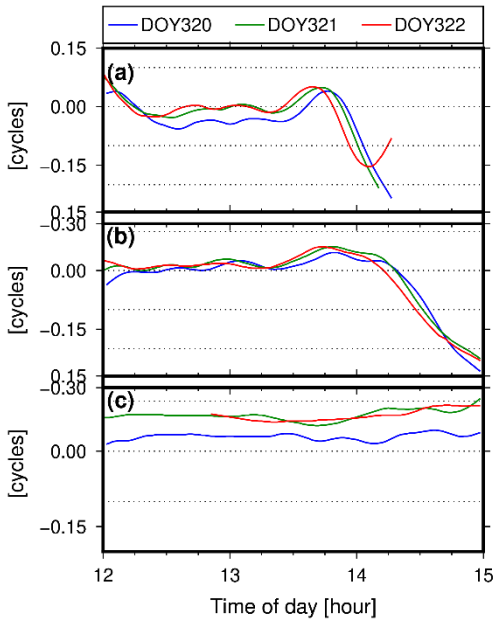

Figure 3-12 Systematic errors estimated over three consecutive days (i.e., the 5-th, 13-th and 21-th sessions), from satellite pairs (a) G31-G22, (b) C10-C03 and (c) C05-C03

3.6 Summary

A semiparametric estimation (SPE)-based approach has been proposed for processing observations from multiple GNSSs. Results from a zero-baseline experiment (with GPS/BeiDou/GLONASS data) with simulated systematic errors have shown that systematic errors can be accurately estimated based on the proposed approach. The approach when combined with VCE can significantly improve the accuracy of VCE and the accuracy of the baseline (over 80% improvement compared to results of VCE and over 90% improvement over the results of LS). Experiments using a real dataset gathered from a GPS/BeiDou baseline of about 10 m in a multipath dominant environment have shown a 35.6% improvement in accuracy when SPE was applied. The determination of the smoothing parameters used in the SPE based on search

algorithms like generalized cross-validation (GCV) is computationally intensive. A method based on LS residuals has been proposed for this purpose and has been proved practical and effective. Results of both simulation and real-data experiments show that the proposed approach is about 100 times faster than the traditional GCV-based methods.

Chapter 4 Multi-GNSS kinematic PPP with mixed use of time-differenced and undifferenced carrier phases

4.1 Motivation

Using observations from multiple GNSSs complicates the data processing models since extra ambiguities and various biases have to be considered (Zumberge et al., 1997; Ge et al., 2008; Dach et al., 2010; Cai and Gao, 2013; Teunissen and Khodabandeh, 2015; Håkansson et al., 2016). Moreover, an ill-posed problem due to poor satellite geometry in kinematic applications (Li et al., 2010) or correlations among parameters (Wang et al., 2016) can make the estimation more complicated than before.

Time-differenced carrier phase (TDCP) observations (Van Graas and Soloviev, 2004) can help to eliminate time-invariant parameters such as phase ambiguities and hardware biases. TDCP has been widely used to smooth noisy pseudoranges (Hofmann-Wellenhof et al., 2008) and to estimate velocities (Van Graas and Soloviev, 2004; Freda et al., 2015). A few mm/s velocity accuracy is achievable based on TDCP compared with cm/s and dm/s accuracies from Doppler measurements and differencing between positions (Soon et al., 2008; Traugott et al., 2008; Freda et al., 2015). TDCP approach has been used in both standalone GPS receivers (Bisnath and Langley, 2002; Serrano et al., 2004a; Serrano et al., 2004b; Van Graas and Soloviev, 2004; Traugott et al., 2008) and coupled GPS/INS (inertial navigation system) systems (Moafipoor et al., 2004; Wendel et al., 2006; Han and Wang, 2012; Zhao, 2016). Deploying TDCP in the single-receiver mode is especially useful for low-cost positioning systems where fixing the ambiguity is unrealistic (Serrano et al., 2004b; Traugott et al., 2008). Another advantage of applying TDCP is that the impacts of some systematic errors that are usually intractable can be reduced (Serrano et al., 2004b; Soon et al., 2008). This enhances the performance of GNSS positioning in adverse scenarios such as in environments with significant signal interference,

dominant multipath signals, or without differential GNSS. Improved positioning performance via exploiting TDCP has been reported in experiments conducted in urban canyons (Ford and Hamilton, 2003).

TDCP measurements lack absolute position information and are vulnerable to accumulative errors (Wendel et al., 2006; Traugott et al., 2008; Colosimo et al., 2011; Han and Wang, 2012). Absolute position information can be introduced by using a known starting point (Soon et al., 2008; Traugott et al., 2008; Zhao, 2016), or by incorporating pseudorange observations in the positioning calculation (Ding, 2007; Han and Wang, 2012). The pseudorange-aided approach may however only achieve standard point positioning accuracy (i.e., m-level), since the pseudorange observations can dominate the positioning process (Zhao, 2016). To reduce the accumulation of errors, TDCP observations need to be carefully corrected. For instance, the use of high-rate precise ephemeris is helpful (Traugott et al., 2008). The accumulated errors can also be linearly de-trended (Colosimo et al., 2011), while the linearity assumption is limited to a few minutes (Li et al., 2013). In addition, TDCP observations connect two state vectors. Therefore, the delayed state errors need to be accounted for in the Kalman filter model, or sequential least-squares model (Bisnath and Langley, 2002; Ford and Hamilton, 2003; Serrano et al., 2004a; Wendel et al., 2006).

In this Chapter, the TDCP is extended into multi-GNSS PPP. Next Section presents the mathematical models of TDCP-based PPP, including a mixed model where TDCP is aided with low-rate undifferenced carrier phase (UDCP) observations, followed by two tests with different kinematics and time lengths.

4.2 TDCP-based multi-GNSS PPP

For brevity, pseudorange is not discussed here since the carrier phase is in general dominant in PPP. The undifferenced ionosphere-free carrier phase observations in length units can be expressed as:

$$\boldsymbol{l} = \boldsymbol{A}\boldsymbol{x} + \boldsymbol{m}T + \boldsymbol{\tau}_0 + \boldsymbol{a} + \boldsymbol{\epsilon} \tag{4-1}$$

where $\boldsymbol{l}$ is the misclosure vector. Corrections projected to the line of sight are applied for satellite clock errors, Earth rotation, tidal loadings, relativistic effects, antenna phase center corrections, tropospheric delays, and wind-up effects (Kouba, 2015); $\boldsymbol{x}$ is the correction to the approximate state vector that comprises receiver position and clock errors; $\boldsymbol{A}$ is the partial derivative matrix of the observations with respect to $\boldsymbol{x}$, or the so-called design matrix; $\boldsymbol{m}$ and T are respectively the mapping function and residual zenith tropospheric delays that should be estimated even for PPP with short observation spans (Kjørsvik et al., 2006); $\boldsymbol{\tau}_0$ stands for ISBs in meters relative to a reference system, e.g., GPS. The intersystem time offsets are lumped to $\boldsymbol{\tau}_0$, if the time of ephemeris products used is not aligned to GPS time; $\boldsymbol{a}$ represents the float ambiguities scaled to meters, which are designed to absorb the various biases (including hardware delays of the satellites and receivers, and other unmodeled systematic biases) that need to be isolated when fixing the ambiguities, as daily-constant or slowly-varying parameters (Dach et al., 2010); and $\boldsymbol{\epsilon}$ indicates observation errors, assumed zero-mean and Gaussian unless contaminated by significant unmodeled errors (Yu et al., 2017).

Assuming T, $\boldsymbol{\tau}_0$ and $\boldsymbol{a}$ are invariant from epoch $t-1$ to epoch t, differencing the two consecutive epochs in kinematic PPP gives the TDCP,

$$\Delta \boldsymbol{l}_t = \boldsymbol{A}_t \boldsymbol{x}_t - \boldsymbol{A}_{t-1} \boldsymbol{x}_{t-1} + \Delta \boldsymbol{m}_t T_t + \Delta \boldsymbol{\epsilon}_t \tag{4-2}$$

where Δ is the time-difference operator. Constant values ($\boldsymbol{\tau}_0$ and $\boldsymbol{a}$) are eliminated in the TDCP observables and the effects of slowly varying systematic errors are reduced, although the observation covariance is amplified, e.g., $\boldsymbol{C}_{\Delta\epsilon_t} \approx \boldsymbol{C}_{\epsilon_t} + \boldsymbol{C}_{\epsilon_{t-1}}$ (Soon et al., 2008), where $\boldsymbol{C}$ represents an observation covariance matrix. TDCP connects two states therefore is related to the dynamic model of the Kalman filter (Bisnath and Langley, 2002; Ford and Hamilton, 2003) if Kalman filter is used to estimate the positions. The term $\boldsymbol{A}_t \boldsymbol{x}_t - \boldsymbol{A}_{t-1} \boldsymbol{x}_{t-1}$ is commonly approximated by $\boldsymbol{A}_t \Delta \boldsymbol{x}_t$ by neglecting $\Delta \boldsymbol{A}_t \boldsymbol{x}_{t-1}$ when the change of $\boldsymbol{A}$ from epoch $t-1$ to t is small (Van Graas and Soloviev, 2004; Ding and Wang, 2011; Freda et al., 2015). TDCP-based positioning can be affected by the quality of the initial state vector, and the positioning accuracy may degrade with time when the systematic errors cannot be mitigated well

(Colosimo et al., 2011; Li et al., 2013; Zhao, 2016). Obtaining an accurate prior state is often not difficult when a base station is near the starting point, or for some applications such as GNSS seismology, the receiver position before the earthquake is available (Li et al., 2013). In this case, the term $\boldsymbol{A}_t\boldsymbol{x}_t - \boldsymbol{A}_{t-1}\boldsymbol{x}_{t-1}$ can be directly reduced to $\boldsymbol{A}_t\boldsymbol{x}_t$ by using the state of epoch $t-1$ as the nominal values of epoch t (Soon et al., 2008). The TDCP thus is rewritten as

$$\begin{aligned} \Delta\boldsymbol{l}_t &= \boldsymbol{A}_t\boldsymbol{x}_t + \Delta\boldsymbol{m}_t T_t + \boldsymbol{\xi}_t \,, \\ \boldsymbol{\xi}_t &= -\boldsymbol{A}_{t-1}\boldsymbol{x}_{t-1} + \Delta\boldsymbol{\epsilon}_t \,, \\ \boldsymbol{C}_{\xi_t} &= \boldsymbol{A}_{t-1}\boldsymbol{C}_{\hat{x}_{t-1}}\boldsymbol{A}'_{t-1} + \boldsymbol{C}_{\Delta\epsilon_t} \end{aligned} \tag{4-3}$$

When there are significant biases in the previous state or inter-epoch systematic errors present, the observation quality estimated via Eq. (4-3) can be over-optimistic. Discussion of the effect of inaccurate prior information on the estimation can be found in (e.g., Xu, 1991). The temporal variability of the GNSS errors (Olynik et al., 2002) needs to be accounted for in either the stochastic model or the functional model (e.g., Yu et al., 2017).

It is proposed to aid the TDCP-based positioning with low-rate UDCP observations to prevent error accumulation. Figure 4-1 depicts the data processing chain that is based on Kalman filtering. 1-Hz multi-GNSS UDCP observations are time-differenced (Eq. 4-3), except those from GPS are mixed with non-GPS TDCPs every 60 s. Consequently, in the proposed approach multi-GNSS observations can be exploited without expanding the number of parameters in the traditional GPS-only PPP (i.e., coordinates, receiver clock error, residual tropospheric delays, and GPS phase ambiguities). The accuracy of the results from the simplified PPP model can be better maintained with fewer satellites, which is useful in urban areas in which multipath signals are abundant and signal blockage often occurs. Lower rate undifferenced observations are used to limit the impact of their systematic errors (Han and Wang, 2012).

The mixed PPP approach can at least be used in two scenarios. First, in applications that have a "static-start" process, such as drones, racing, sports, and seismology, an accurate initial position can be obtained by a nearby base station or historical

information. Second, for moving platforms such as cars, ships, and buoys, an accurate initial point can be obtained by traditional converged PPP or RTK. Once an accurate starting position becomes available, applying the mixed-PPP has some obvious advantages over the existing multi-GNSS PPP method. For instance, fewer parameters need to be estimated, leading to a simplified positioning model. The computation burden of high-rate kinematic positioning can also be reduced. In addition, the accuracy can be retained with fewer satellites, which is useful in urban areas where signal shadowing often occurs. Using the TDCP observations can also reduce the impacts of systematic errors such as multipath errors and residual atmospheric delays. This allows a simplified mitigation of systematic errors in the rapidly-changing environments encountered by moving platforms.

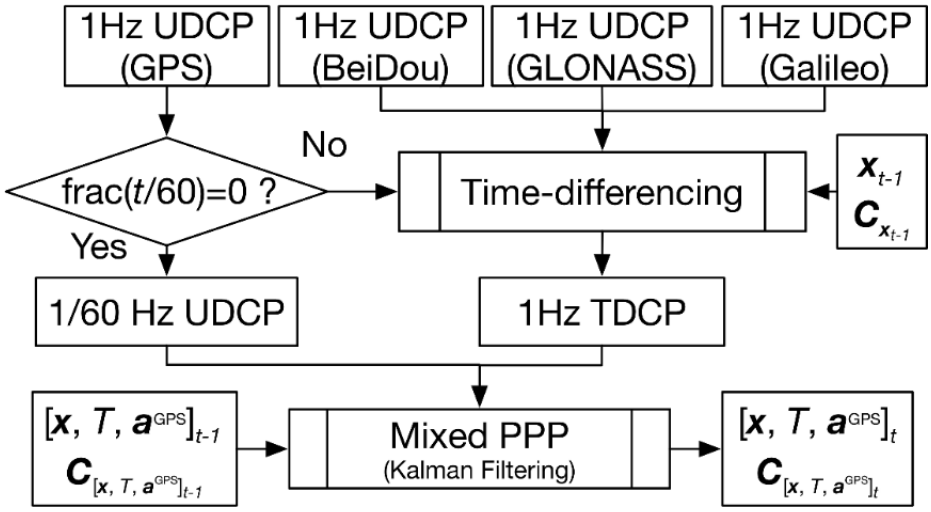

Figure 4-1 Processing chain of the Mixed PPP approach, function frac(·) returns the fractional part of a real number

4.3 Experiments and results

To investigate the performance of the proposed TDCP-based multi-GNSS positioning approach, two 1-Hz dual-frequency datasets collected with Trimble R10 receivers are analyzed. The first dataset has 34-min GPS/BeiDou/GLONASS observations. It was acquired with a vehicle at a site shown in Figure 4-2, where there are tall buildings

and trees along the road. The second dataset contains quad-GNSS (i.e. GPS, BeiDou, GLONASS and Galileo) observations acquired from an 83-min running exercise at a site as shown in Figure 4-3. There is a high slope to the north of the site. Both datasets are affected by interferences such as multipath errors (Leick et al., 2015) as shown in Figure 4-4. Atmospheric delays are considered another major error source as the sites are near the coast that is usually very humid. The dynamics of the two rovers are shown in Figure 4-5 by their velocities.

Figure 4-2 Driving trajectories in Shatin area of Hong Kong (denoted as PUST) on June 11, 2015, 08:00:00–08:33:59 (GPS time). The data is processed with HKSS as base station, about 7 km from PUST

Figure 4-3 Running trajectories near a high slope in Homantin area of Hong Kong (denoted as PUHM) on July 4, 2018, 12:50:00–14:13:00 (GPS time). The data is processed with HKPU as base station, which is about 0.7 km from PUHM

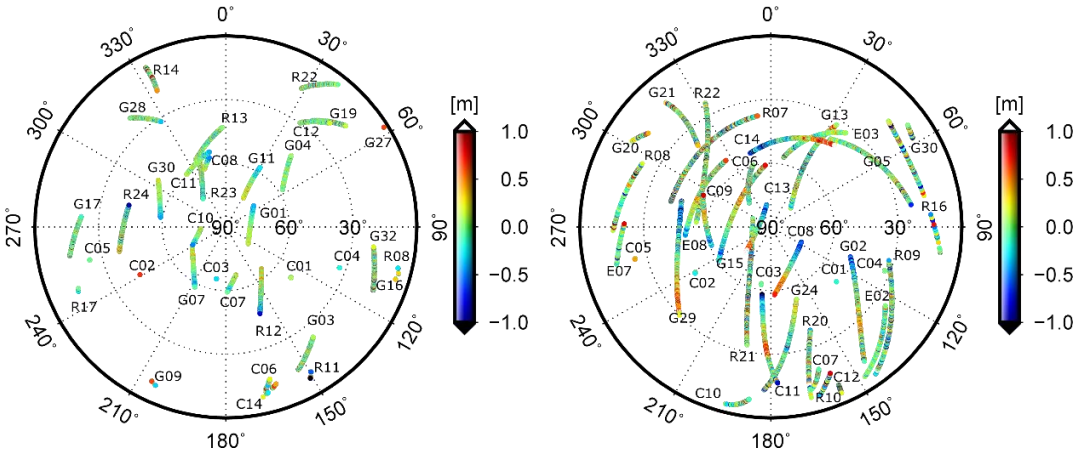

Figure 4-4 Pseudorange multipath combination (MPC1) of rovers at PUST (left) and at PUHM (right), respectively. Here G, C, R and E respectively stand for GPS, BeiDou, GLONASS and Galileo

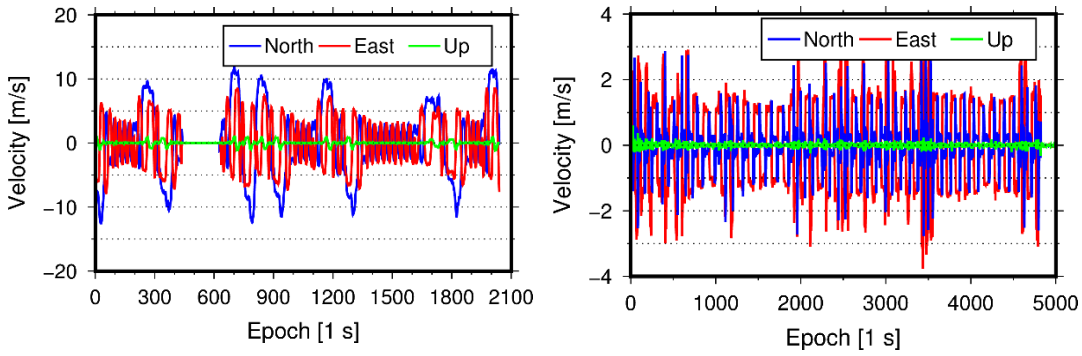

Figure 4-5 Velocity time series of rovers at PUST (up) and PUHM (bottom), respectively

Observations below 5 degrees of elevation angle and those identified containing cycle slips (Blewitt, 1990) are not used. GNSS error sources are carefully corrected (Kouba, 2015) to avoid error accumulation. The 5-min orbit and 30-s clock products provided by the German Research Centre for Geoscience (GFZ) are used. The predicted tropospheric delays are applied (Leandro et al., 2008) while the residual zenith delays are computed in the estimation process. The a priori variance-covariance matrix of the undifferenced observations is determined by the elevation-dependent model (Hofmann-Wellenhof et al., 2008). In setting up the parameters to be estimated, the coordinates and the clock errors in $\boldsymbol{x}$ are modeled as white noise with the variances being 10^6 m^2 and 10^{10} m^2 respectively. The residual zenith tropospheric delays T and the ISBs $\boldsymbol{\tau}_0$ are treated as random walk processes with the power spectral densities being 4 cm^2/h and 1 cm^2/h, respectively.

The results from three types of data processing strategies are compared. They are based on undifferenced observations, TDCP, and TDCP aided with low-rate (60 s) undifferenced GPS observations, as denoted by UnDiff, TDiff, and Mixed, respectively. Accurate initial positions obtained from relative positioning (1-cm uncertainty is assumed for each coordinate component) are input to all the three approaches. The data processing is carried out on a laptop (64-bit Windows 10 with Intel i7-3520M CPU of 2.9 GHz and memory of 8 GB), and the time consumed is recorded to understand the efficiency of each of the approaches.

Figure 4-6 shows the coordinate errors (with respect to the results of post-processed kinematic relative positioning) when applying the UnDiff PPP based on GNSS and GPS-only observations. It can be seen that UnDiff positioning errors fluctuate significantly, which is considered due to multipath signals and some inaccurate initial parameters (including phase ambiguities, residual zenith atmospheric delays, and ISBs). For the rover at PUST, the height errors are significantly larger than the horizontal errors, perhaps due to the significant atmospheric delays. For the rover at PUHM, although it moved much slower than that at PUST, the coordinate errors exhibit smaller fluctuations while the drift errors become dominant especially in the north and up components. This may be due to the larger multipath effects and the longer data length. It is clear that the GNSS solutions outperform those based on GPS-only data in almost all directions. Faster convergences can be seen in the GNSS coordinates compared with those of GPS-only in PUHM. Therefore, hereafter only GNSS solutions are discussed. Figure 4-7 further gives the coordinate errors from TDiff- and Mixed-PPP approaches. Figure 4-8 and Table 4-1 compare the position root-mean-square (RMS) errors. In the TDiff approach, the ambiguities and ISBs are eliminated and therefore there is no need to initialize them, and the effects of the atmospheric delays on the height coordinates are remarkably reduced. The TDiff approach suppresses the fluctuations while the results contain some apparent drifts in the east direction. The position RMS errors are reduced by 41.1%, from 25.0 cm to 14.7 cm compared to UnDiff. The Mixed approach can effectively reduce the drifts seen in the TDiff solution, although some small jumps appear occasionally in the north direction. These jumps are considered due to the introduction of the absolute position information from the undifferenced observations. The proposed approach achieved 52.8% improvements in the position accuracy over the UnDiff approach. For the rover at PUHM, the TDiff solution cannot resist the accumulative errors well and thus drifts significantly over time. The results are finally worse than those of the UnDiff solution. The Mixed approach effectively diminishes the drifts and the position RMS error is reduced by 28.3% compared to that of UnDiff.

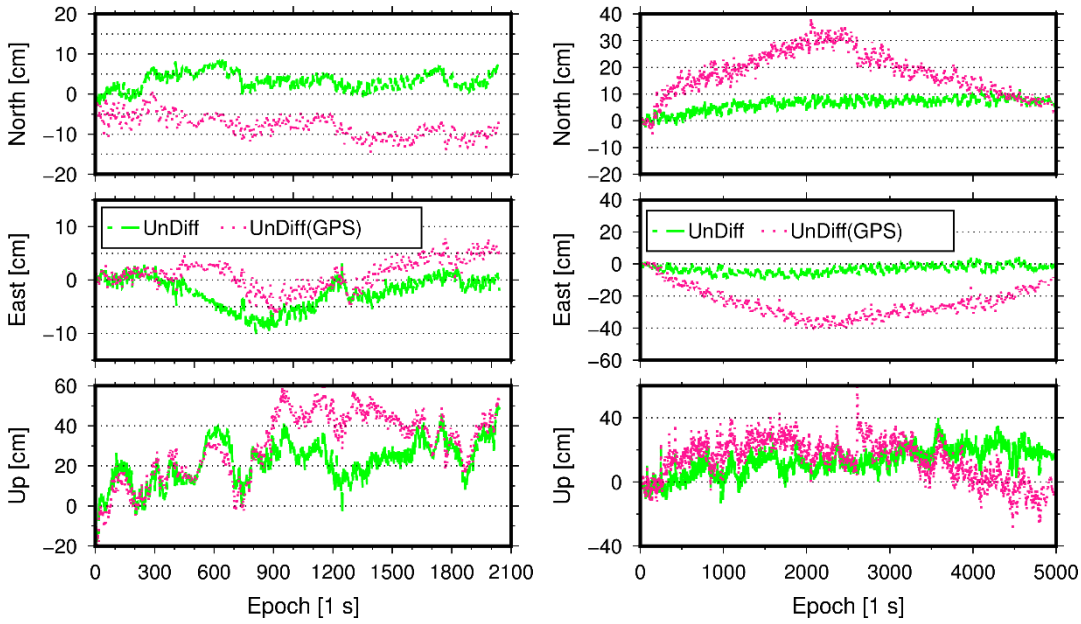

Figure 4-6 Coordinate errors of rovers at PUST (left) and PUHM (right) from UnDiff PPP based on GNSS and GPS-only data

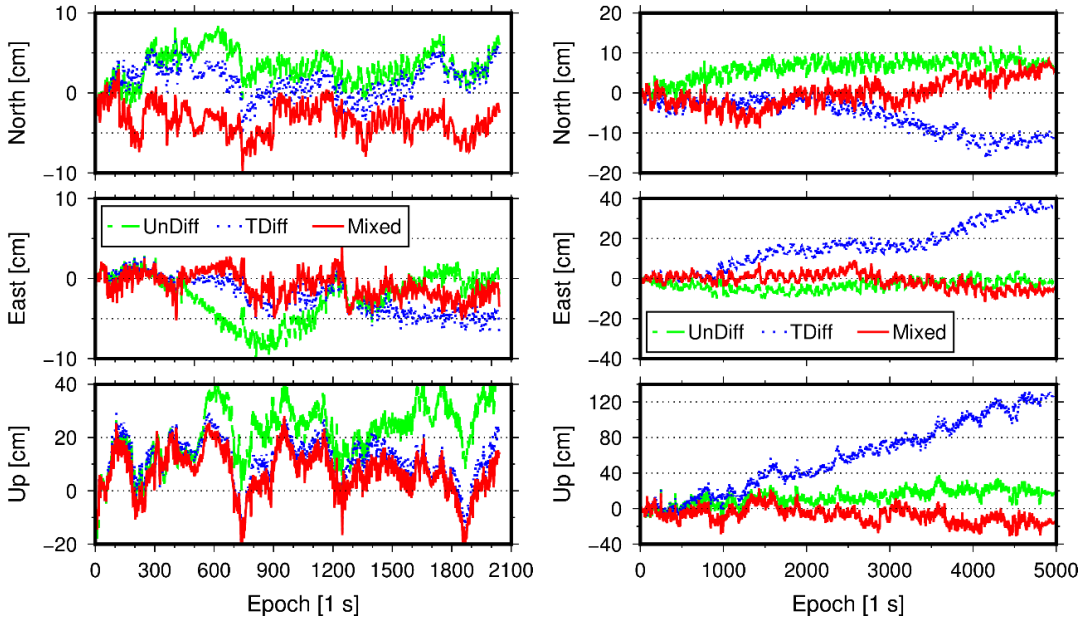

Figure 4-7 Coordinate errors of rovers at PUST (left) and PUHM (right) from different PPP approaches

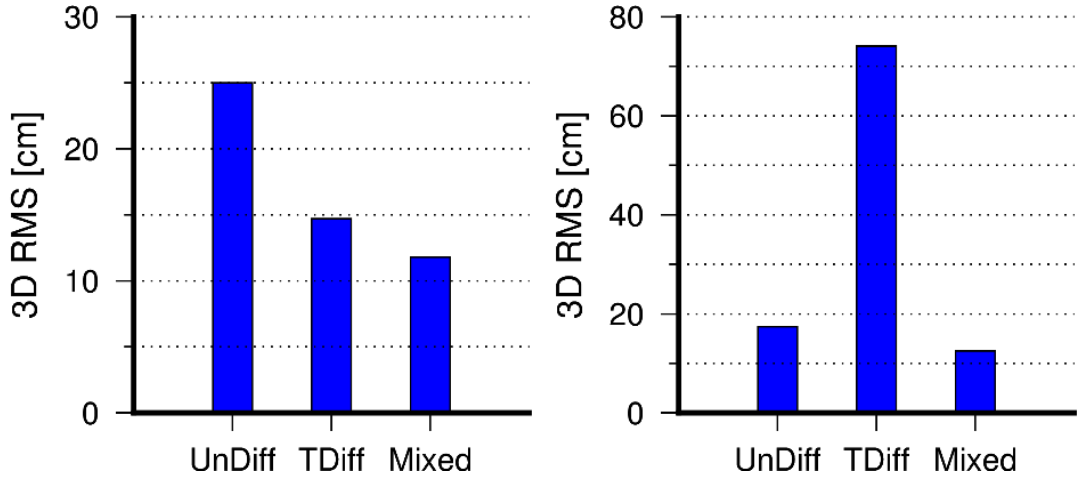

Figure 4-8 Position RMS errors of rovers at PUST (left) and PUHM (right) from different PPP approaches

Table 4-1 Statistics of kinematic PPP errors from different processing approaches

Rover	Method	Mean [cm]			RMS [cm]			3D RMS [cm]	Impr. [%]
		North	East	Up	North	East	Up		
PUST	UnDiff	3.3	-2.3	21.9	3.9	3.7	24.4	25.0	
	TDiff	1.5	-2.2	11.4	2.5	3.1	14.2	14.7	41.1
	Mixed	-3.4	-0.9	7.0	3.9	1.8	11.0	11.8	52.8
PUHM	UnDiff	6.3	-3.3	12.9	6.8	4.2	15.5	17.4	
	TDiff	-5.8	16.1	58.8	7.2	19.5	71.1	74.1	-325.3
	Mixed	-0.1	-1.1	-7.4	3.4	3.8	11.4	12.5	28.3

Figure 4-9 shows the ionosphere-free carrier phase residuals of the UnDiff and TDiff solutions. The residuals from the Mixed approach consist of both the TDCP and UDCP and therefore are not presented. The TDCP residuals appear more random as the observations contain much less systematic errors than the undifferenced observations. Therefore TDCP-based PPP can produce superior results in interference-rich areas over the traditional PPP approach.

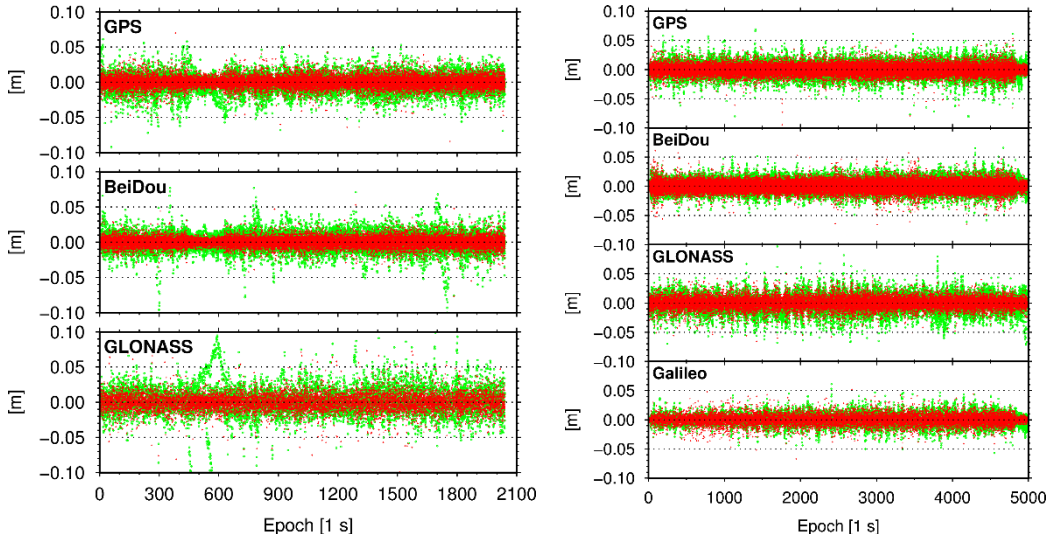

Figure 4-9 Ionosphere-free carrier phase residuals of observations from different satellite systems for rovers at PUST (left) and PUHM (right). The green and red colors represent the residuals of UDCP and TDCP, respectively

For the TDCP-based positioning, an accurate initial state vector is critical, especially the residual zenith tropospheric delays and the initial position. Table 4-2 shows the PPP RMS errors when tropospheric delays are corrected using only the a priori tropospheric model. The height RMS errors of the UnDiff solution increase significantly to 42.1 and 23.2 cm respectively for the rovers at PUST and PUHM, compared to 24.4 and 15.5 cm when the residual zenith delays are estimated (see Table 4-1). Comparing the height RMS errors in Table 4-1 and Table 4-2, it can also be seen that without parameterizing the residual zenith refraction, most of the height RMS errors increase slightly (sub-cm level) when the TDiff and Mixed methods are used. Results for PUHM are not satisfactory when TDiff method is used since they are affected by significant drift errors. This indicates that the TDCP can effectively mitigate the impacts of time-varying systematic errors in a short term (the data interval is 1 s in this experiment). It also confirms that estimating the residual tropospheric delays is necessary for the TDCP-based approaches to achieve a high positioning accuracy.

Table 4-2 Performances of different kinematic PPP approaches when the residual zenith tropospheric delays are not parameterized

Rover	Method	Mean [cm]			RMS [cm]			3D RMS	Impr.
		North	East	Up	North	East	Up	[cm]	[%]
PUST	UnDiff	4.2	-3.9	39.5	4.7	4.8	42.1	42.7	
	TDiff	1.5	-2.1	11.6	2.5	3.1	14.3	14.8	65.3
	Mixed	-3.4	-1.3	7.7	3.9	2.2	11.5	12.4	71.0
PUHM	UnDiff	4.8	-0.3	-20.1	5.2	2.2	23.2	23.8	
	TDiff	-5.8	16.3	57.4	7.1	19.7	69.2	72.3	-203.1
	Mixed	2.6	-5.7	-8.1	5.0	7.4	11.8	14.8	38.0

To investigate the impact of the initial position accuracy, the two datasets are tested with varying initial position errors (adding 5, 10, 30, 50, 100 and 200 cm errors respectively to each coordinate component). As shown in Figure 4-10, the position errors of the three processing approaches grow differently when the errors in the initial position are added. The undifferenced observations allow the solution to converge more rapidly. In contrary, TDiff-derived results are significantly affected by the initial position errors. The Mixed approach is more robust than TDiff. Figure 4-11 and Table 4-3 show the position RMS errors with respect to varying initial position errors. Except for the TDiff solution at PUHM where the drifting errors are dominant, the TDCP-based approaches can provide better positioning results than the UnDiff approach when the initial position errors are within about 1 m. The mixed use of UDCP and TDCP observations improves the positioning accuracy over the TDiff approach. When an accurate initial position is unavailable, undifferenced observations may be preferred. One can overcome the problem by starting the TDCP-based PPP once an accurate position is available, or empirically down-weight the TDCP in the Mixed approach until the solution converges.

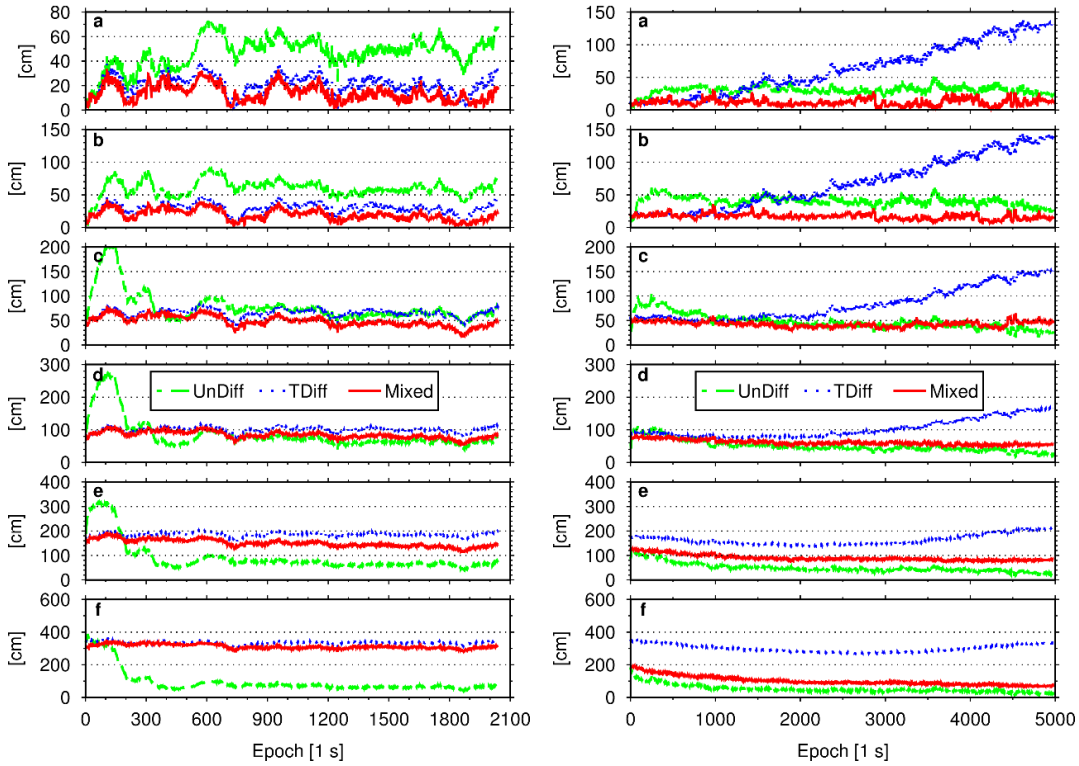

Figure 4-10 Position error time series of PUST (left) and PUHM (right) from different approaches and with varying initial position errors, from a to f, 8.6, 17.3, 51.9, 86.5, 173.2 and 346.4 cm position errors, respectively

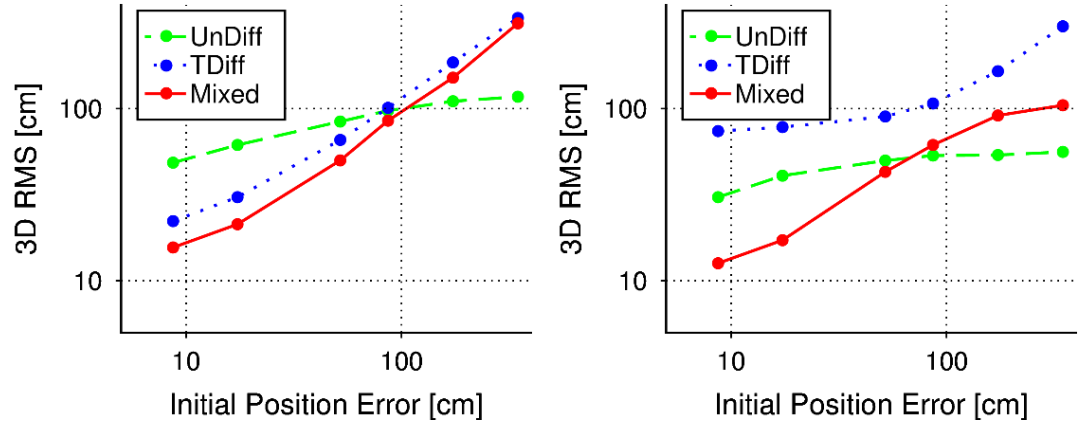

Figure 4-11 Initial position errors vs. position RMS errors of PUST (left) and PUHM (right)

Table 4-3 Position RMS errors from different processing approaches and with varying initial position errors

Initial position error [cm]	3D RMS [cm]					
	PUST			PUHM		
	UnDiff	TDiff	Mixed	UnDiff	TDiff	Mixed
8.6	48.5	22.2	15.6	30.6	74.0	12.6
17.3	61.4	30.6	21.3	40.8	78.0	17.2
51.9	84.1	65.8	50.1	49.9	89.9	42.9
86.5	97.3	100.9	84.9	53.4	107.1	61.4
173.2	110.2	185.4	151.3	53.7	164.8	91.3
346.4	117.0	335.4	312.1	56.1	300.3	104.4

Table 4-4 shows the time consumption of the different PPP processing approaches. The TDiff and the Mixed approaches consumed about 2.9 % to 6.3 % less time than the UnDiff approach. This advantage will be more obvious when handling a high-rate dataset, or in applications where the ambiguities are to be fixed.

Table 4-4 Average time consumed by different processing approaches

Rover	Method	Mean time used [ms]	Improvements [%]
PUST	UnDiff	50259.4	
	TDiff	47070.7	6.3
	Mixed	48033.7	4.4
PUHM	UnDiff	134114.7	
	TDiff	128180.6	4.4
	Mixed	130256.7	2.9

4.4 Summary

Precise point positioning (PPP) with observations from multiple GNSSs is both advantageous and challenging, considering the ample redundant observations available and the difficulties in optimally deriving the position solutions in the presence of various biases. This study has presented an approach that is based on the mixed use of time-differenced carrier phase (TDCP) and low-rate undifferenced

carrier phase observations. Test results have shown that when an accurate initial position is available, the approach can achieve 28–71 % improvement in positioning accuracy over the traditional PPP approach. The TDCP-based approaches are also efficient in computation, an advantage in high-rate positioning applications. A drawback of the TDCP-based approaches is the requirement for an accurate initial position. The issue can however be overcome by adopting various techniques such as using a lower weight for the TDCP observations until an accurate solution is achieved.

Chapter 5 Two-step robust multi-GNSS positioning

5.1 Motivation

Integrating multi-GNSS observations benefits positioning, while a growing number of parameters increase the computation complexity, and unmodeled errors (including outliers, residual systematic errors, and impropriate stochastic modeling) may sometimes degrade the solutions (Banville and Langley, 2013; El-Mowafy, 2014; Pozo-Pérez et al., 2017; Yang et al., 2017). Much research efforts have also given to subset-estimation. Observation geometry plays an important role in positioning applications (Meng et al., 2004) and it has been used as a criterion for selecting a subset of observations when sufficient satellites exist (Teng and Wang, 2016). Subset-estimation is also applied for ambiguity resolution. Ambiguities are often partially resolved (Teunissen et al., 1999; Brack, 2017) to reduce the calculation, although a fixed solution is preferred in terms of accuracy (Ge et al., 2008). Another example of subset-estimation is the robust estimation, which essentially attempts to separate data into a "clean" subset and a complementary subset that is discarded or down-weighted (Yang et al., 2002). However, these subset-estimation methods cannot fully exploit the observations offered by multiple GNSSs and achieve only suboptimal solutions.

Previous research has mainly focused on a suboptimal solution as a compromise to the computation complexity. Few studies have explored an optimal solution by substituting subset-estimation-derived results into the positioning. This chapter presents such a two-step strategy that attempts to fully use observations from multiple GNSSs. The next section addresses the implementations of the two-step strategy in both single-point positioning and static relative positioning. Evaluations are then performed, based on one-week multi-GNSS data in which the measurements present frequent interferences of multipath effects and blockages. Finally, concluding remarks are presented.

5.2 Traditional positioning method

5.2.1 Observation equations

The linearized pseudorange equation reads

$$l_p = \boldsymbol{u} \cdot \boldsymbol{r} + \tau + b + e_p \tag{5-1}$$

where l_p is the misclosure (i.e. observation-minus-computed value), where corrections of satellite clock error, Sagnac, and relativity effects are applied, and tropospheric and ionospheric delays are corrected using the UNB3m (Leandro et al., 2008) and single-layer model (Hofmann-Wellenhof et al., 2008) respectively; $\boldsymbol{u} \in \mathbb{R}^{1\times 3}$ is the unit LOS vector; $\boldsymbol{r} \in \mathbb{R}^3$ represents the increment in the nominal receiver position; τ stands for the receiver clock error in meters; b represents ISB relative to a reference system, e.g. GPS; and e_p contains pseudorange noise and other unmodeled errors, such as multipath effects.

For a short baseline with the base station fixed, the DD carrier phase observation in length units can be written as (Wang, 2000)

$$\begin{aligned} l_{\nabla\Delta\varphi}^{ij} &= \nabla \boldsymbol{u}^{ij} \cdot \boldsymbol{r} + \lambda_i \nabla\Delta N_F^{ij} + e_{\nabla\Delta\varphi}^{ij}\,, \\ \nabla\Delta N_F^{ij} &= \nabla\Delta N^{ij} + \left(1 - \frac{\lambda_j}{\lambda_i}\right)\Delta N^j \end{aligned} \tag{5-2}$$

where $l_{\nabla\Delta\varphi}^{ij}$ is the misclosure of DD carrier phase observation between the i-th and j-th satellites. Here, ∇ and Δ are cross-satellite and cross-receiver single-differencing (SD) operators respectively. A reference satellite is selected for each GNSS involved, except that double-differenced (DD) BeiDou observations are formed between either GEO-type or non-GEO-type satellites to avoid inter-satellite-type biases when using different receiver hardware (Nadarajah et al., 2013). λ denotes the wavelength, $\nabla\Delta N$ is the DD integer ambiguity, ΔN is the cross-receiver SD integer ambiguity, and $e_{\nabla\Delta\varphi}$ represents the DD observation errors. The frequency inconsistency of the satellite pair destroys the integer nature of DD ambiguities (i.e. $\nabla\Delta N_F^{ij}$ are float if $\lambda_i \neq \lambda_j$), which is the main obstacle faced by the GLONASS ambiguity resolution. To reduce the

impacts, pseudoranges are used to estimate the initial values of ambiguities. A search process is also applied to obtain the final GLONASS SD ambiguity ΔN^j when determining the DD ambiguities (Wang, 2000).

5.2.2 Outlier mitigation

Methods for outlier mitigation can be categorized as two types. The (co)variance-inflation method iteratively reduces the weights of observations that are contaminated by gross errors (Yang et al., 2002). Its alternative is based on the mean-shift model that exhaustively tests the significance of possible combinations of the outliers (Koch, 2015). The former is adopted in this study since the mean-shift model in general assumes a single outlier, whereas determining the number of outliers that exist in a dataset remains an open problem (Ding and Coleman, 1996; Knight et al., 2010).

The least-squares solution can be expressed as

$$\begin{cases} \hat{\boldsymbol{x}} = (\boldsymbol{A}'\boldsymbol{P}\boldsymbol{A})^{-1}\boldsymbol{A}'\boldsymbol{P}\boldsymbol{l}, \qquad \boldsymbol{Q}_{\hat{x}} = (\boldsymbol{A}'\boldsymbol{P}\boldsymbol{A})^{-1} \\ \hat{\boldsymbol{e}} = \boldsymbol{A}\hat{\boldsymbol{x}} - \boldsymbol{l}, \qquad \boldsymbol{Q}_{\hat{e}} = \boldsymbol{P}^{-1} - \boldsymbol{A}\boldsymbol{Q}_{\hat{x}}\boldsymbol{A}' \\ \hat{\sigma} = \sqrt{\hat{\boldsymbol{e}}'\boldsymbol{P}\hat{\boldsymbol{e}}/(n-t)} \end{cases} \tag{5-3}$$

where $\boldsymbol{A} \in \mathbb{R}^{n\times t}$, $\hat{\boldsymbol{x}} \in \mathbb{R}^t$, and $\boldsymbol{l} \in \mathbb{R}^n$ are the design matrix, unknown parameter vector, and misclosure vector, respectively, with $D(\boldsymbol{l}) = \sigma^2\boldsymbol{P}^{-1}$, where σ^2 and $\boldsymbol{P}$ are the variance factor and weight matrix respectively; $\hat{\boldsymbol{e}} \in \mathbb{R}^n$ is the residual vector with $E(\hat{\boldsymbol{e}}) = \boldsymbol{0}$ and $D(\hat{\boldsymbol{e}}) = \hat{\sigma}^2\boldsymbol{Q}_{\hat{e}}$; $\hat{\sigma}$ is the estimate of σ. The LS solution is considered being distorted at a preselected significance level α if

$$\chi^2_{(n-t)} = (n-t)\hat{\sigma}^2 > \chi^2_{(n-t),\alpha} \tag{5-4}$$

In the (co)variance inflation model, outliers are considered zero-mean and random, with large variances. The weight matrix is updated by reducing relevant elements (Yang et al., 2002)

$$p^+_{ij} = \gamma_{ij}p^-_{ij}\text{ , with }\gamma_{ij} = \sqrt{\gamma_{ii}\gamma_{jj}} \tag{5-5}$$

where p_{ij} is the element in weight matrix $\boldsymbol{P}$ at the ith row and jth column; γ corresponds to the reduction factors and can be empirically set as (Yang et al., 2002)

$$\gamma_{ii} = \begin{cases} 1 & |\tilde{e}_i| \le k_0 \\ \dfrac{k_0}{|\tilde{e}_i|}\left(\dfrac{k_1 - |\tilde{e}_i|}{k_1 - k_0}\right)^2 & k_0 < |\tilde{e}_i| \le k_1 \\ 0 & |\tilde{e}_i| > k_1 \end{cases} \quad (5\text{-}6)$$

where $\tilde{e}_i$ is the standardized residual, i.e. $\tilde{e}_i = \hat{e}_i / \left[\hat{\sigma}\sqrt{\boldsymbol{Q}_{\hat{e}}(i,i)}\right]$; the initial value of $\hat{\sigma}$ can be obtained through $\hat{\sigma} = 1.483\text{med}(|\tilde{\boldsymbol{e}}|)$, and then $\hat{\sigma} = \sqrt{\frac{\hat{\boldsymbol{e}}'\boldsymbol{P}\hat{\boldsymbol{e}}}{n-t}}$ in the iterations; k_0 and k_1 are two constants empirically set to 1.5 and 3.5 respectively. The process of (co)variance inflation is iterated until no change is required.

5.3 Two-step positioning method

A two-step strategy has been developed to enhance multi-GNSS positioning. Figure 5-2 depicts the processing chains of the traditional SPP and the proposed two-step SPP. χ^2 test is used to detect outliers. The first step of the new method is similar to the traditional SPP, while a more "exclusive" estimation in which only GPS observations considered to be of "high quality" is carried out. Stringent satellite selection is implemented through increasing data-masking thresholds and/or removing observations identified as outliers in the misclosure vector. Selecting high-quality observations can lead to a robust estimation of the initial solution. Only a limited number of outliers can be detected and identified based on the mean-shift model (Knight et al., 2010) or alternatively inflating the corresponding (co)variance elements of the stochastic model (Yang et al., 2002). Although involving more observations in general leads to a higher reliability of outlier detection, using observations from a single GNSS enables removing outliers directly from the misclosure vector. Prescreening observations before including them in an integrated adjustment has been reported to be useful (Banville and Langley, 2013) especially in the case of encountering extra-large outliers (Leick et al., 2015, p.70). In a single-GNSS pseudorange misclosure vector, a big outlier can be identified if the following condition is fulfilled,

$$\left|l_p - \bar{\boldsymbol{l}}_p\right| = \left|(\boldsymbol{u} - \bar{\boldsymbol{u}}) \cdot \boldsymbol{r} + e_p - \bar{e}_p\right| > 10 * \sigma_{l_p}$$
$$\sigma_{l_p} = 1.48 * \mathrm{Med}(\left|l_p - \mathrm{Med}(\boldsymbol{l}_p)\right|) \tag{5-7}$$

where function $\mathrm{Med}(\cdot)$ returns the median value of an input vector. A relatively large error threshold, i.e. 10, is used due to the geometric terms $\boldsymbol{u}$ and $\boldsymbol{r}$. Based on the initial position obtained in the first step, the second step first estimates non-position parameters, i.e. intersystem biases. This allows prescreening outliers in the misclosure vector for each non-GPS system. The second step then refines the results through an "inclusive" estimation that reduces the masking thresholds and includes the remaining observations, aiming at a high-accuracy solution. Small outliers can be removed since the redundant observations strengthen the model geometry and the resultant high reliability lead to more sensitive outlier detection.

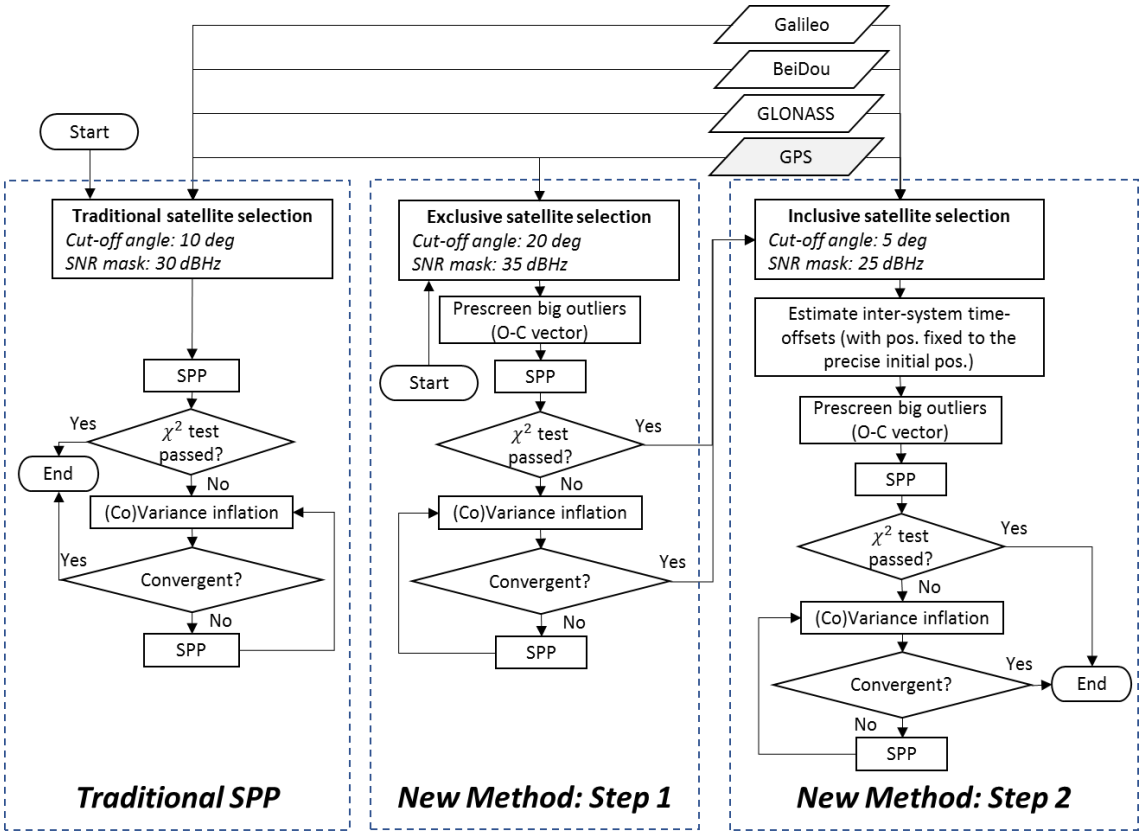

Figure 5-1 Processing chains of the traditional and proposed two-step standard point positioning methods

Compared to the traditional positioning method, the two-step method can preserve the observation redundancy and is computationally more efficient especially if multiple outliers present. The two-step method can prescreen some big outliers, and this reduces the number of iterations of the robust estimation required in the traditional positioning method.

Figure 5-2 shows the processing chains of traditional static DD positioning and the one realized based on the concept of the two-step method. The first step of the new method is the same as the traditional approach, while higher observation masking thresholds and only GPS data are used. In DD positioning, ambiguity resolution plays a critical role. Incorporating the initial baseline components derived from the first step allows the elimination of ambiguities in the second step. Assuming the position correction vector $\boldsymbol{r}$ in Eq. (5-2) is small enough we obtain,

$$\nabla\Delta\widehat{N}_F^{ij} \approx {\lambda_i}^{-1} l_{\nabla\Delta\varphi}^{ij},\ D_{\nabla\Delta\widehat{N}_F^{ij}} \approx \sigma^2 {\lambda_i}^{-2} \boldsymbol{P}^{-1}(i,i) + \hat{\sigma}^2 \nabla\boldsymbol{u}^{ij} \boldsymbol{Q}_{\hat{\boldsymbol{r}}} (\nabla\boldsymbol{u}^{ij})' \qquad (5\text{-}8)$$

where $D_{\nabla\Delta\widehat{N}_F^{ij}}$ is the approximate variance of the estimate $\nabla\Delta\widehat{N}_F^{ij}$. Ignoring the reference satellite's SD ambiguity considering the small coefficient (Wang, 2000), once the uncertainty of the estimated ambiguity has dropped below a certain fraction of a wavelength (e.g., 0.3 cycles in this study), the ambiguity can be fixed via rounding to its nearest integer,

$$\nabla\Delta\breve{N}^{ij} = \mathrm{ROUND}\left(\nabla\Delta\widehat{N}_F^{ij}\right), \qquad \text{when } \sqrt{D_{\nabla\Delta\widehat{N}_F^{ij}}} < 0.3 \qquad (5\text{-}9)$$

Observation with inaccurate estimated ambiguities (the fraction part is larger than 0.3 cycles of the wavelength) will be down-weighted or removed. For GLONASS observations, the fraction components of DD ambiguities induced by the reference satellites' SD ambiguity errors are considered as observation errors, therefore the noise level is empirically inflated by 1.5 times.

In the multi-GNSS DD carrier phase misclosure vector, once the ambiguities are fixed and removed, an outlier can be identified if

$$\left|\nabla\Delta l_{\varphi} - \nabla\Delta\bar{\boldsymbol{l}}_{\varphi}\right| = \left|(\nabla\boldsymbol{u} - \nabla\bar{\boldsymbol{u}}) \cdot \boldsymbol{r} + \nabla\Delta e_{\varphi} - \nabla\Delta\bar{e}_{\varphi}\right| > 10 * \sigma_{l_{\varphi}}$$
$$\sigma_{l_{\varphi}} = 1.48 * \mathrm{Med}(\left|\nabla\Delta l_{\varphi} - \mathrm{Med}(\nabla\Delta\boldsymbol{l}_{\varphi})\right|) \quad (5\text{-}10)$$

For some small outliers that remain in the measurements, their detection is applied in conjunction with adjustment based on the analysis of the residuals. This technique utilizes the total redundancy and strength provided by the overall geometry and is thus sensitive to small outliers (Leick et al., 2015, p. 70).

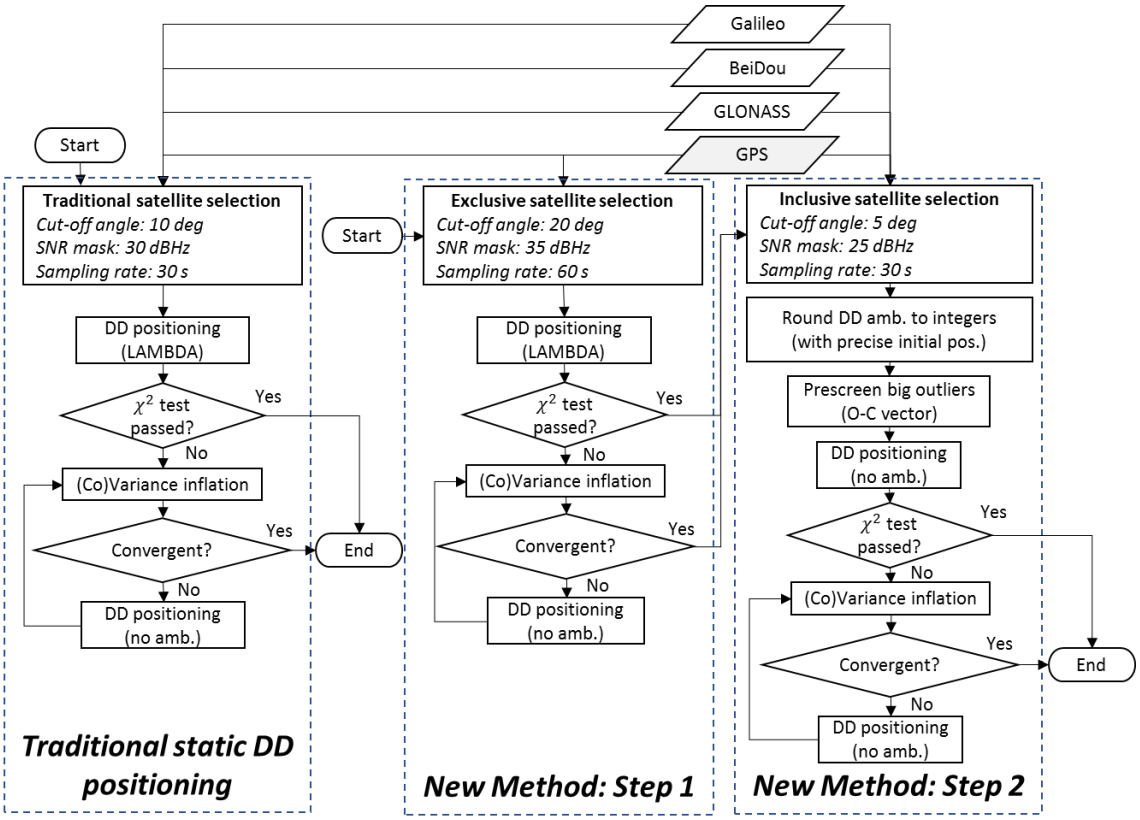

Figure 5-2 Processing chains of the traditional and proposed two-step double-difference positioning methods

5.4 Experiments and results

One-week quad-GNSS data (DOYs 157–163) was acquired at two stationary sites on the rooftop of Block Z of Hong Kong Polytechnic University to investigate the effectiveness of the proposed two-step algorithm. Trimble R9 receivers were deployed

with TRM59800.00 choke antenna for the PUZA and Zephyr Geodetic antenna for the base PUZB. As shown in Figure 5-3, high barriers exist in the south of the site PUZA, which result in an interference-rich environment. Figure 5-4 shows the signal strengths of the different satellite systems. The signals are highly impacted by ambient interferences, especially for those from low elevation angles and the southern sky. BeiDou contributes considerably in the median-high-elevation sky considering the developing MEO constellation.

Figure 5-3 Multi-GNSS sites PUZA (up left) and PUZB (up right) with a distance of approximately 50 m

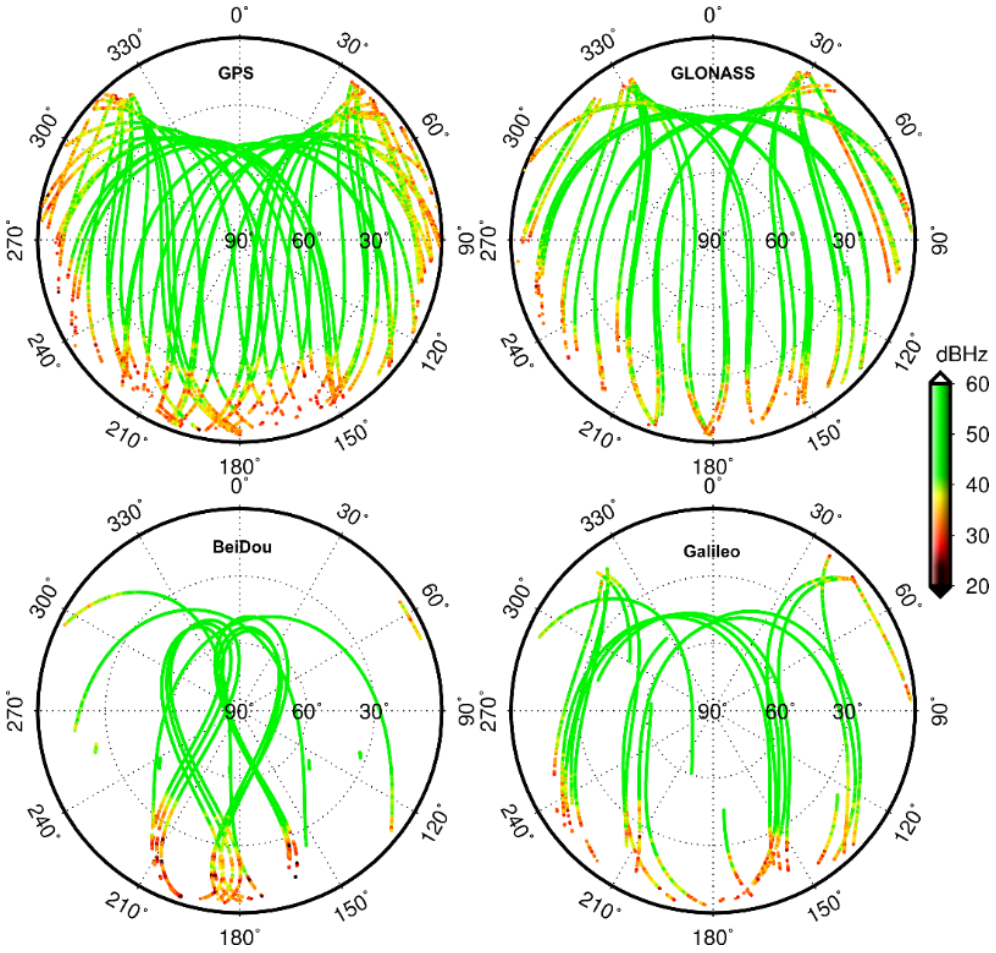

Figure 5-4 Sky plots of C/N_0 signal strengths at site PUZA on DOY 157, 2018

The data of PUZA was sampled at 30 s and processed in single-frequency SPP and static relative positioning. The corresponding processing configurations are given in Table 5-1 and Table 5-2. The "exclusive" positioning step uses higher cut-off angles and signal-to-noise ratio masks than those of the "inclusive" step. For the "exclusive" relative positioning, a data interval of 60 s is used to reduce the computation burden and the one of 30 s is used in the "inclusive" step for a strong model geometry. The ground-true position is estimated based on the entire datasets. Weights of the observations are determined by the elevation-based model, the zenith noise of the pseudorange is set to 0.5 m and the zenith noise of carrier phases is 1% of their wavelengths. Inter-system weight-ratios of GPS/BeiDou/GLONASS/Galileo systems are empirically set to 1.0/0.5/0.25/1.0. For the relative positioning, the data is divided into 3-h sessions. LAMBDA (Teunissen, 1995) is used for ambiguity resolution, and R-ratio is utilized as the validation indicator (Euler and Schaffrin, 1991).

Table 5-1 Processing configurations for single-frequency single-point positioning (data interval: 30 s, length: 7 days)

Settings	Exclusive	Inclusive	Traditional
Cut-off angle [deg]	20	5	10
SNR mask [dBHz]	35	25	30
Systems used	GPS	All	All

Table 5-2 Processing configurations for static short-baseline single-frequency static DD positioning (3 h × 56 sessions)

Settings	Exclusive	Inclusive	Traditional
Cut-off angle [deg]	20	5	10
SNR mask [dBHz]	35	25	30
Sampling interval [s]	60	30	30
Systems used	GPS	ALL	ALL
Ambiguities resolution	LAMBDA	Rounding	LAMBDA

Three processing strategies, namely positioning based on the traditional GPS-only method, the traditional multi-GNSS method, and the proposed two-step method are compared. Some outliers are artificially added to the pseudoranges to test the robustness of different methods: three 20 m gross errors (assuming the pseudorange noise is 3 m) are added every 10 min to the pseudoranges of satellites randomly selected, including one GPS satellite and two non-GPS satellites. The magnitude of gross errors is enlarged to 100 m from the third day to understand the positioning performance under large outliers. In addition, in the last three days the number of outliers for non-GPS systems is increased to five to investigate the effectiveness of different methods in the presence of outliers. Given that there are many low-quality carrier phases already due to the ambient interferences, no artificial outliers are added to the carrier phases.

Figure 5-5 to Figure 5-7 show the SPP errors of different positioning methods and the corresponding statistic results are summarized in Table 5-3. As shown in Figure 5-5 the traditional GPS-only SPP produces noisy positioning results, in which the influences of gross errors are noticeable. Using multi-GNSS data strengthens the positioning model and the results are clearly smoothened (Figure 5-6). In addition, the

multi-GNSS approach resists well three outliers simultaneously, even though the outlier magnitudes become larger from the third day. Compared with the GPS-only solution, the multi-GNSS method reduces the 3D RMS error from 7.9 m to 6.3 m (see Table 5-3). However, multi-GNSS positioning is complicated when the number of outliers is increased to six. Frequent jumps present in the results of traditional quad-GNSS SPP, obviously in the last three days where six outliers simultaneously exist. When the proposed two-step method is applied, as shown in Figure 5-7, nearly all the outliers are successfully removed. The positioning RMS is decreased by 4.8% to 6.0 m compared to that of traditional multi-GNSS approach. The improvement can be more obvious if the outliers become more frequent.

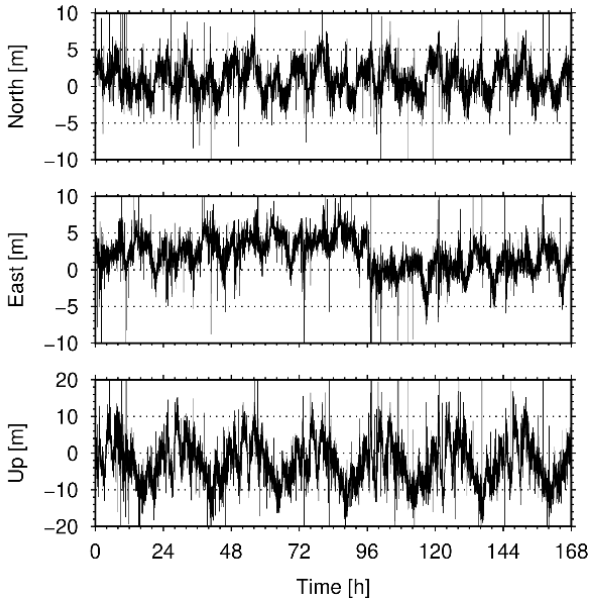

Figure 5-5 Standard SPP errors based on GPS data with artificial outliers

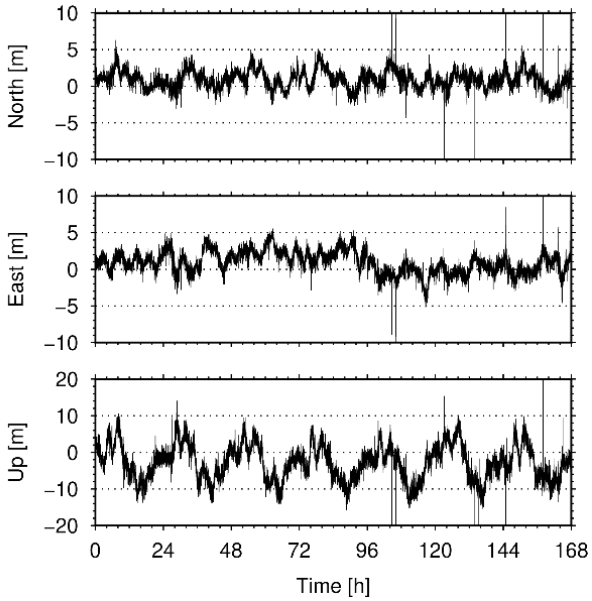

Figure 5-6 Standard SPP errors based on quad-GNSS data with artificial outliers

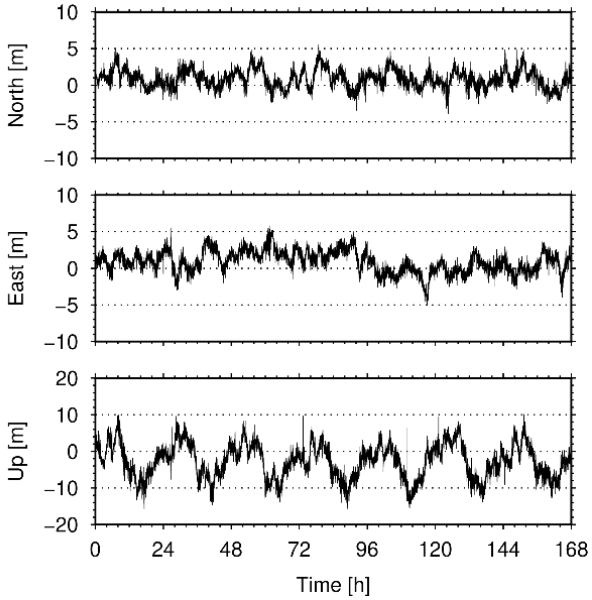

Figure 5-7 Two-step SPP errors based on quad-GNSS data with artificial outliers

Table 5-3 Statistics of position errors of different SPP approaches with artificial outliers (data interval: 30 s, length: 7 days)

SPP Method	Mean [m]			RMS [m]			3D RMS [m]
	North	East	Up	North	East	Up	
Trad. (GPS)	1.0	2.0	-2.6	2.5	3.1	6.8	7.9
Trad. (quad-GNSS)	0.9	1.0	-2.8	1.6	1.8	5.8	6.3
New (quad-GNSS)	0.9	0.9	-2.7	1.5	1.8	5.5	6.0

Table 5-4 summarizes the mean statistics when different SPP methods are used. The computer time is also recorded to assess the computation efficiency. The number of observations in multi-GNSS solutions is about three times more than that only based on GPS, resulting in 55% smaller PDOP values. The two-step SPP is advantageous, it has more observations, slightly lower PDOPs, and a significantly higher computation efficiency. The mean time consumed decreases 40.4% compared to that of the traditional multi-GNSS.

Table 5-4 Mean statistics of different SPP approaches (data interval: 30 s, length: 7 days)

Method	Obs.# used	PDOP	Time used [ms]
Trad. (GPS)	9	2.0	1.1
Trad. (quad-GNSS)	29	1.0	17.1
New (quad-GNSS)	31	0.9	10.2

The static baseline errors from different positioning methods are shown in Figure 5-8 to Figure 5-10. Table 5-5 provides the baseline repeatability (the definition is given in Eq. 3-27) and Table 5-6 presents the mean statistics. The traditional GPS-only solution produces evident noisy baseline errors especially in the up component (Figure 5-8). They are considered to be caused by the limited satellite geometry and systematic errors in observations from low elevation angles. When multi-GNSS data is used, the repeatability in the up component is considerably decreased. In contrast, the repeatability in the east direction is slightly deteriorated, which may be due to the inaccurate a priori stochastic model and the disturbances of outliers and systematic errors (Figure 5-4). Applying the two-step approach mitigates these impacts, and the repeatability in up component is further decreased. Compared to the traditional multi-GNSS solution, the new method reduces the 3D position repeatability by 21.4% from 5.6 mm to 4.4 mm. As summarized in Table 5-6, the improvement mainly partially lies in smaller PDOPs (obtained based on SPP at PUZA) since more observations are used in the proposed method. Compared with GPS-only solution, multi-GNSS approach lowers the R-ratios since there are more ambiguities to be fixed. The two-step method needs only to partially resolve the ambiguities (i.e. those of GPS) and

applying the new method improves the mean R-ratio, indicating a more reliable solution. Another advantage of the proposed method is the high computation efficiency, it consumed 27.7% less time than employed by the traditional multi-GNSS.

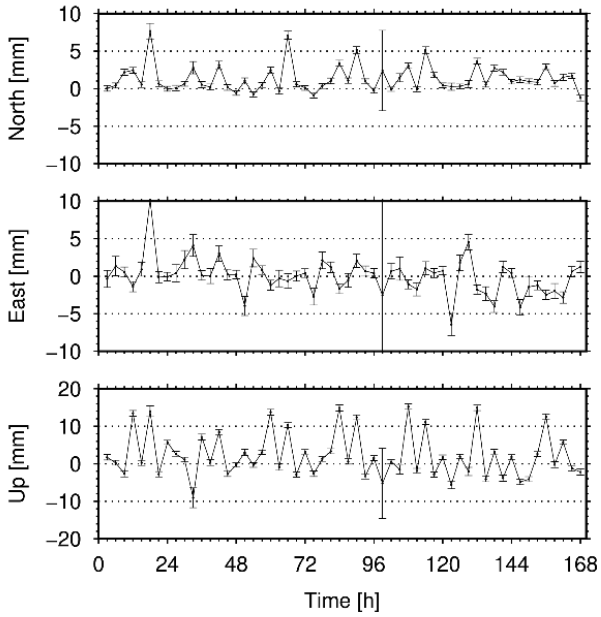

Figure 5-8 Static relative positioning errors based on GPS data

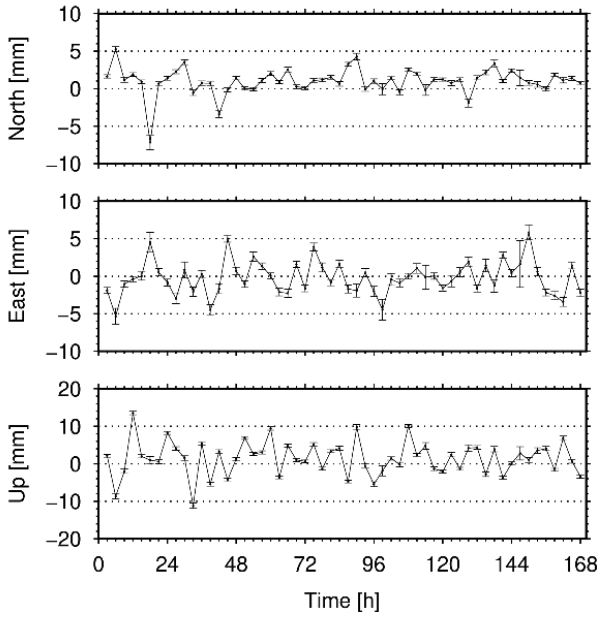

Figure 5-9 Static relative positioning errors based on quad-GNSS data

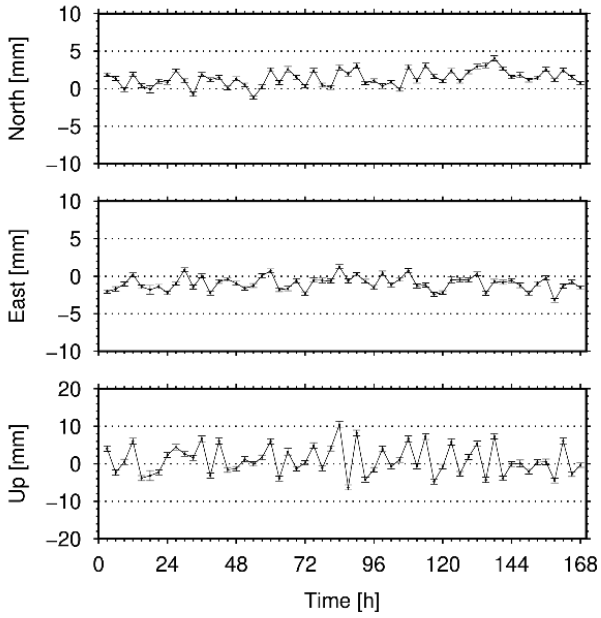

Figure 5-10 Two-step static relative positioning errors based on quad-GNSS data

Table 5-5 Baseline repeatability of different approaches (3 h×56 sessions)

Method	North [mm]	East [mm]	Up [mm]	3D Position [mm]
Trad. (GPS)	1.7	1.7	6.0	6.9
Trad. (quad-GNSS)	1.6	1.9	4.7	5.6
New (quad-GNSS)	1.7	1.3	3.8	4.4

Table 5-6 Mean statistics of different approaches in static relative positioning (3 h×56 sessions)

Method	Obs.# used	PDOP	R-ratio	Time used [s]
Trad. (GPS)	2079	2.4	155.2	1.7
Trad. (quad-GNSS)	4953	1.4	7.6	17.7
New (quad-GNSS)	6643	1.1	333.6	12.8

5.5 Summary

Using observations from multiple GNSSs can enhance the positioning accuracy compared with traditional GPS-only solutions. However, extra ambiguities and biases need to be accounted for and the situation of multiple outliers may become more

frequent. This inevitably complicates the positioning data processing, in particular for time-consuming processes including ambiguity resolution and outlier mitigation. To fully use the multi-GNSS observations with an acceptable computation complexity, a two-step positioning strategy has been developed. A subset estimation is firstly applied to generate an initial position. The known position thus obtained is then used to screen outliers and remove ambiguities in the observations. The second step performs a full-set estimation and includes all available observations to derive an improved solution. One-week multi-GNSS real data was used to validate the proposed method in both SPP and static relative positioning. Experimental results demonstrate that the proposed approach is more robust and efficient than the traditional positioning approach. Compared with the traditional GPS-only approach, the proposed method can improve the positioning accuracy in both SPP and static relative positioning with a higher computation efficiency.

Chapter 6 Conclusions and recommendations

6.1 Results and contributions

Positioning applications benefit from a higher observation redundancy provided by multiple GNSSs (including GPS, GLONASS, BeiDou, Galileo and other systems). However, integrating the growing amount of observations without complicating the positioning model is intrinsically challenging. A cumbersome cause of the increasing model complexity is that extra phase ambiguities, various biases and some unmodeled errors (such as residual systematic errors and frequent presence of multiple outliers) have to be considered. In response to the challenge, enhancing multi-GNSS positioning become imperative and the main efforts of this study have contributed to the following aspects:

(1) Evaluation of benefits of multi-GNSS positioning

This study has first investigated the benefits of using multi-GNSS datasets, with both current existing GNSSs and their future full constellations. Multipath errors and typical signal-shadowing environments were simulated to understand the performance of multi-GNSS positioning in GNSS-restricted areas. The results show that the satellite availability can increase globally by 280% compared to GPS alone when observations from the other existing GNSSs (i.e. GLONASS/BeiDou/Galileo) are used. With their future full constellations, the satellite availability can further increase to 340%. Accordingly, the quad-GNSS combination reduces the GPS PDOP by 52.4% at present and 57.1% when their full constellations are reached. Tests of static relative positioning with real and simulated datasets are conducted to understand the improvement in multi-GNSS positioning performance compared to GPS alone. The experimental results based on a 4-m short real baseline show that using quad-GNSS data, compared with the GPS-only approach, can reduce the position errors by up to 52.4%. The simulation also demonstrates the advantages of multi-GNSS integration, in which the position errors decrease by 48.6–63.8% with the current four

constellations. These indices will increase to 48.5–69.0% when their full constellations are reached.

(2) Mitigation of systematic error based on semiparametric estimation (SPE) in multi-GNSS positioning

To refine the multi-GNSS positioning model a new positioning method has been proposed to take residual systematic errors into account. Systematic errors can bias both traditional least-squares (LS) and variance component estimation (VCE). A SPE-based approach is proposed to mitigate such influences. Results from a zero-baseline (GPS/BeiDou/GLONASS) experiment with simulated systematic errors demonstrate significant improvements in baseline accuracy (over 80% when compared with VCE and over 90% regarding LS) and higher R-ratios in ambiguity resolution. Experiments using real datasets from a short GPS/BeiDou baseline in a multipath-dominant environment obtain 35.6% improvements in accuracy for the baseline when the SPE approach is applied. The SPE should be carried out before a VCE that can be seriously falsified when systematic errors are present. The determination of the smoothing parameters using L-curve and generalized cross-validation methods is computationally intensive, thereby hindering the application of SPE. An approximate procedure to estimate the smoothing parameters based on LS-derived residuals is adopted and proven to be practical. The experiments with simulated and real-data show that the proposed method can be about 100 times faster than the traditional generalized cross-validation-based methods.

(3) Kinematic multi-GNSS PPP based on a mixed differencing method

A mixed differencing method has been developed for the kinematic multi-GNSS PPP. The new concept is based on the mixed use of time-differenced and undifferenced observations. The distinctive characteristics of the proposed algorithm lie in three main aspects. First, the time-differencing operation eliminates constant parameters, including ambiguities and hardware biases. Second, quasi-constant systematic errors that can come from residual atmospheric refractions and multipath effects are mitigated. Third, a subset of observations can be retained undifferenced to suppress

the position divergence of the time-differencing technique. The effectiveness of the proposed approach is validated in some kinematic PPP tests. Up to 71% improvements in position accuracy with respect to the traditional PPP is achieved with the proposed approach. The time-differenced approach is efficient in computation, which is of critical concern regarding high-rate applications. A major drawback of time-differenced observations in positioning is the request for an accurate initial position, which is unnecessarily a major problem if the initial state can be supplied by RTK or converged PPP.

(4) Multi-GNSS positioning based on a two-step positioning procedure

A new two-step multi-GNSS positioning approach has been proposed. First, a subset of observations considered to be of "high quality" (from higher elevation angles or with larger signal strengths) is selected to robustly estimate an initial position. Second, the initial position derived is used to remove outliers and ambiguities. All available observations are finally processed together to strengthen and refine the positioning. The effectiveness and efficiency of the proposed method are validated in SPP and static relative positioning. The two-step procedure has achieved 4.8% and 21.4% improvements in SPP and static relative positioning accuracy respectively when compared to the traditional positioning approaches. A higher efficiency of the two-step method has also been confirmed in the experiment, with the computation time reduced by 40.4% and 27.7% respectively in standard point positioning and relative positioning.

6.2 Recommendations

Future research efforts are anticipated to be devoted to the following aspects:

(1) Enhancement and application of SPE

The proposed SPE approach has issues that deserve further study. For example, the proposed SPE approach may be applied to dynamic applications in which may have challenging issues such as changing observation environments. The regularizer is

application-dependent and therefore its adaptive selection, such as searching in a prebuilt regularizer database, requires exploration. A robust SPE may be desirable when real datasets contain gross errors. The SPE approach is suitable for deformation monitoring in which unmodeled errors from multipath effects and residual tropospheric delays are often present.

(2) Application of mixed-differencing positioning approach with moving platforms

Future studies of mixed-differencing positioning are expected to cover diverse applications, ranging from high-rate (e.g. 10–100 Hz), long-term (e.g. buoys), and long-range (e.g. unmanned aerial vehicles) PPP to standard positioning involving single-frequency receivers using broadcast ephemeris. Further research efforts are needed on the convenient acquisition of an accurate initial position, e.g., by using RTK or convergent PPP, to facilitate the practical use of the mixed-differencing method. Another interesting use of the time-differenced observations is the integration with INS. GNSS signals are prone to interruptions. This weakness in kinematic environments where signal outages often occur, can be prevented by incorporating INS. In addition, the inherent trending drifts of time-differenced PPP need further study, e.g., to refine the weighting schemes, and to develop flexible satellite selection algorithms and models that account for the residual systematic errors.

(3) Application of the two-step positioning approach in deformation monitoring

The two-step multi-GNSS positioning approach can be applicable to deformation monitoring where the positioning reliability is of primary concern. The site environments in deformation monitoring often have limited sky views with severe signal interferences. The two-step method is therefore useful in such situations. To attain reliable and accurate positioning results, more studies are required in selecting a high-quality subset of observations to generate the initial position, as well as in more rigorous hypothesis testing for eliminating ambiguities and outliers before a full-set

adjustment. The proposed two-step method can also be extended to post processing kinematic and PPP.

Appendix A Semiparametric estimation based on generalized least-squares

This section presents a generalized least-squares (GLS)-based approach for solving the semiparametric model. It is essentially accomplished by the parameterization of nonparametric components through using prior information (in the form of pseudo-observations). More thorough discussions of different estimators can be found in (Xu, 1992; Fischer and Hegland, 1999; Kusche and Klees, 2002; Kotsakis, 2005; Xu et al., 2006; Teunissen and Amiri-Simkooei, 2008; Ding et al., 2015), among others.

The GLS model that contains the semiparametric model can be expressed as

$$\begin{cases} \underbrace{\begin{bmatrix}\mathbf{L}\\ \mathbf{L}_c\end{bmatrix}}_{\mathbf{Z}} = \underbrace{\begin{bmatrix}\mathbf{A} & \mathbf{I}\\ \mathbf{0} & \mathbf{C}\end{bmatrix}}_{\mathbf{B}}{}_{u\times m} \underbrace{\begin{bmatrix}\mathbf{X}\\ \mathbf{S}\end{bmatrix}}_{\mathbf{Y}} + \underbrace{\begin{bmatrix}\boldsymbol{\epsilon}\\ \boldsymbol{\epsilon}_c\end{bmatrix}}_{\boldsymbol{\zeta}}, \quad (u > t, \quad m > t) \\ E(\boldsymbol{\zeta}) = \mathbf{0}, \quad D(\boldsymbol{\zeta}) = \sigma^2\mathbf{W}^{-1} = \sigma^2\begin{bmatrix}\mathbf{P}^{-1} & \mathbf{0}\\ \mathbf{0} & \mathbf{P}_c^{-1}\end{bmatrix} \end{cases} \tag{A-1}$$

where $\mathbf{L}_c$ is a vector of u pseudo-observations, with design matrix $\mathbf{C}$, error vector $\boldsymbol{\epsilon}_c$ and weight matrix $\mathbf{P}_c$; both the design matrix $\mathbf{A}$ and expanded design matrix $\mathbf{B}$ have full column rank; errors from observations and those from pseudo-observations are assumed being uncorrelated, resulting in a block-diagonal weight matrix $\mathbf{W}$. According to the GLS inversion principle (Menke, 2015)

$$\hat{\boldsymbol{\zeta}}^{\mathrm{T}}\mathbf{W}\hat{\boldsymbol{\zeta}} = \hat{\boldsymbol{\epsilon}}^{\mathrm{T}}\mathbf{P}\hat{\boldsymbol{\epsilon}} + \hat{\boldsymbol{\epsilon}}_c^{\mathrm{T}}\mathbf{P}_c\hat{\boldsymbol{\epsilon}}_c = \min \tag{A-2}$$

where $\hat{\boldsymbol{\zeta}} = \mathbf{B}\hat{\mathbf{Y}} - \mathbf{Z}$, we obtain,

$$\begin{cases} \hat{\mathbf{Y}} = \mathbf{M}^{-1}\mathbf{U}, \quad \mathbf{Q}_{\hat{\mathbf{Y}}\hat{\mathbf{Y}}} = \mathbf{M}^{-1} = \begin{bmatrix}\mathbf{Q}_{\hat{\mathbf{X}}\hat{\mathbf{X}}} & \mathbf{Q}_{\hat{\mathbf{X}}\hat{\mathbf{S}}}\\ \mathbf{Q}_{\hat{\mathbf{X}}\hat{\mathbf{S}}}^{\mathrm{T}} & \mathbf{Q}_{\hat{\mathbf{S}}\hat{\mathbf{S}}}\end{bmatrix} \\ \mathbf{M} = \mathbf{B}^{\mathrm{T}}\mathbf{W}\mathbf{B} = \begin{bmatrix}\mathbf{N} & \mathbf{A}^{\mathrm{T}}\mathbf{P}\\ \mathbf{P}\mathbf{A} & \mathbf{N}_s\end{bmatrix}, \quad \mathbf{N} = \mathbf{A}^{\mathrm{T}}\mathbf{P}\mathbf{A} \\ \mathbf{N}_s = \mathbf{P} + \mathbf{C}^{\mathrm{T}}\mathbf{P}_c\mathbf{C} \\ \mathbf{U} = \mathbf{B}^{\mathrm{T}}\mathbf{W}\mathbf{Z} = \begin{bmatrix}\mathbf{A}^{\mathrm{T}}\mathbf{P}\mathbf{L}\\ \mathbf{P}\mathbf{L} + \mathbf{C}^{\mathrm{T}}\mathbf{P}_c\mathbf{L}_c\end{bmatrix} \end{cases} \tag{A-3}$$

Thus, the GLS solution can be written as

$$\begin{aligned}\hat{\mathbf{X}} &= \mathbf{Q}_{\hat{\mathbf{X}}\hat{\mathbf{X}}}\mathbf{A}^{\mathrm{T}}\mathbf{P}\mathbf{L} + \mathbf{Q}_{\hat{\mathbf{X}}\hat{\mathbf{S}}}(\mathbf{P}\mathbf{L} + \mathbf{C}^{\mathrm{T}}\mathbf{P}_{\mathrm{c}}\mathbf{L}_{\mathrm{c}}) \\ \hat{\mathbf{S}} &= \mathbf{Q}_{\hat{\mathbf{X}}\hat{\mathbf{S}}}^{\mathrm{T}}\mathbf{A}^{\mathrm{T}}\mathbf{P}\mathbf{L} + \mathbf{Q}_{\hat{\mathbf{S}}\hat{\mathbf{S}}}(\mathbf{P}\mathbf{L} + \mathbf{C}^{\mathrm{T}}\mathbf{P}_{\mathrm{c}}\mathbf{L}_{\mathrm{c}})\end{aligned} \tag{A-4}$$

where the cofactor matrices $\mathbf{Q}_{\{\cdot\}}$ can be yielded via applying matrix calculus

$$\begin{cases} \mathbf{Q}_{\hat{\mathbf{X}}\hat{\mathbf{X}}} = (\mathbf{N} - \mathbf{A}^{\mathrm{T}}\mathbf{P}\mathbf{N}_{\mathrm{s}}^{-1}\mathbf{P}\mathbf{A})^{-1} = (\mathbf{A}^{\mathrm{T}}\mathbf{P}(\mathbf{I} - \mathbf{N}_{\mathrm{s}}^{-1}\mathbf{P})\mathbf{A})^{-1} \\ \mathbf{Q}_{\hat{\mathbf{S}}\hat{\mathbf{S}}} = \mathbf{N}_{\mathrm{s}}^{-1} + \mathbf{N}_{\mathrm{s}}^{-1}\mathbf{P}\mathbf{A}\mathbf{Q}_{\hat{\mathbf{X}}\hat{\mathbf{X}}}\mathbf{A}^{\mathrm{T}}\mathbf{P}\mathbf{N}_{\mathrm{s}}^{-1} \\ \mathbf{Q}_{\hat{\mathbf{X}}\hat{\mathbf{S}}} = -\mathbf{Q}_{\hat{\mathbf{X}}\hat{\mathbf{X}}}\mathbf{A}^{\mathrm{T}}\mathbf{P}\mathbf{N}_{\mathrm{s}}^{-1} \\ \text{or,} \\ \mathbf{Q}_{\hat{\mathbf{X}}\hat{\mathbf{X}}} = \mathbf{N}^{-1} + \mathbf{N}^{-1}\mathbf{A}^{\mathrm{T}}\mathbf{P}\mathbf{Q}_{\hat{\mathbf{S}}\hat{\mathbf{S}}}\mathbf{P}\mathbf{A}\mathbf{N}^{-1} \\ \mathbf{Q}_{\hat{\mathbf{S}}\hat{\mathbf{S}}} = (\mathbf{N}_{\mathrm{s}} - \mathbf{P}\mathbf{A}\mathbf{N}^{-1}\mathbf{A}^{\mathrm{T}}\mathbf{P})^{-1} \\ \mathbf{Q}_{\hat{\mathbf{X}}\hat{\mathbf{S}}} = -\mathbf{N}_{\mathrm{s}}^{-1}\mathbf{P}\mathbf{A}\mathbf{Q}_{\hat{\mathbf{S}}\hat{\mathbf{S}}} \end{cases} \tag{A-5}$$

Substituting (A-5) into (A-4) gives

$$\begin{aligned}\hat{\mathbf{X}} = &(\mathbf{A}^{\mathrm{T}}\mathbf{P}(\mathbf{I} - \mathbf{N}_{\mathrm{s}}^{-1}\mathbf{P})\mathbf{A})^{-1}\mathbf{A}^{\mathrm{T}}\mathbf{P}(\mathbf{I} - \mathbf{N}_{\mathrm{s}}^{-1}\mathbf{P})\mathbf{L} \\ &-(\mathbf{A}^{\mathrm{T}}\mathbf{P}(\mathbf{I} - \mathbf{N}_{\mathrm{s}}^{-1}\mathbf{P})\mathbf{A})^{-1}\mathbf{A}^{\mathrm{T}}\mathbf{P}\mathbf{N}_{\mathrm{s}}^{-1}\mathbf{C}^{\mathrm{T}}\mathbf{P}_{\mathrm{c}}\mathbf{L}_{\mathrm{c}}\end{aligned} \tag{A-6}$$

$$\hat{\mathbf{S}} = \mathbf{N}_{\mathrm{s}}^{-1}\mathbf{P}(\mathbf{L} - \mathbf{A}\hat{\mathbf{X}}) + \mathbf{N}_{\mathrm{s}}^{-1}\mathbf{C}^{\mathrm{T}}\mathbf{P}_{\mathrm{c}}\mathbf{L}_{\mathrm{c}} \tag{A-7}$$

Appendix B Estimation of the signal and variance of a data sequence

Considering an m data-points series $y(i) = s(i) + e(i)$, where $i \in \{1,2,\dots,m\}$ and s denotes signals vary slowly in time/space, e is white noise with variance σ^2. Applying a low-pass operation, typically, the following window averaging technique, one can extract the signal as (Evans and Jones, 2008)

$$\hat{s}\,(i) = \frac{1}{2w+1}\sum_{j=i-w}^{i+w} y(j) \tag{B-1}$$

where w denotes window size at ith data point. Thus, an $(m \times m)$ low-pass operation matrix can be written as (here w_0 is a pre-given window size),

$$\begin{cases} \mathbf{F}_{\mathrm{L}}(i,j) = (2\,w+1)^{-1}, \quad (i-w \le j \le i+w) \\ w = \begin{cases} i-1, & (1 \le i \le w_0) \\ m-i, & (m-w_0+1 \le i \le m) \\ w_0, & \text{otherwise} \end{cases} \end{cases} \tag{B-2}$$

Using a high-pass operation to remove the signal, e.g., the first difference,

$$\hat{e}\,(i) = \frac{y(i+1)-y(i)}{\sqrt{2}}, \quad i \in \{1,2,\cdots,m-1\} \tag{B-3}$$

then one can estimate the variance via the following mean square successive difference, which is insensitive to the signal,

$$\hat{\sigma}^2 = \frac{1}{(m-1)}\sum_{i=1}^{m-1} \hat{e}\,(i)^2 \tag{B-4}$$

Correspondingly, the $(m-1) \times m$ difference operation matrix is

$$\mathbf{F}_{\mathrm{H}} = \mathrm{bidiag}(-\frac{1}{\sqrt{2}}, \frac{1}{\sqrt{2}}) \tag{B-5}$$

Appendix C 3D multipath geometric models

(1) Reflection model

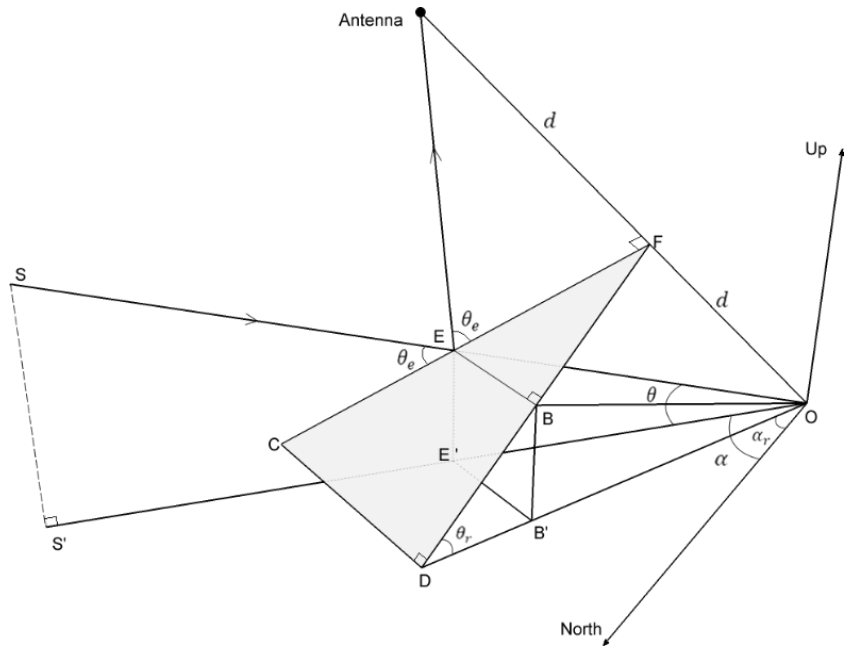

Figure 6-1 3D multipath reflection model

Consider a reflection surface CDF with slope angle θ_r and slope aspect α_r, the antenna simultaneously receives the direct and duplicate signals from a satellite S at elevation angle θ and azimuth angle α. O is the image of the antenna with respect to the reflector surface. According to the antenna-reflector geometry, the additional path delay Δs with respect to the direct signal can be deduced as follows:

denoting $\Delta\alpha = \angle \mathrm{S'OD} = \alpha - \alpha_r$, $\theta_e = \angle \mathrm{CES}$ and $\theta' = \angle \mathrm{BOB'}$, since

$$\begin{cases} \Delta s = 2d\sin(\theta_e) \\ \sin(\theta_e) = \sin(\angle \mathrm{FBO})\cos(\angle \mathrm{BOE}) \\ \angle \mathrm{FBO} = \theta' + \theta_r \\ \tan(\angle \mathrm{BOE}) = \tan(\Delta\alpha)\cos(\theta') \\ \tan(\theta) = \tan(\theta')\cos(\Delta\alpha) \end{cases} \tag{C-1}$$

the delay can be obtained as

$$\begin{cases} \Delta s = 2d\sin(\theta_e) \\ \theta_e = \text{asin}\{\sin(\theta' + \theta_r)\cos\{\text{atan}[\tan(\alpha - \alpha_r)\cos(\theta')]\}\} \\ \theta' = \text{atan}_2(\tan(\theta), \cos(\alpha - \alpha_r)) \end{cases} \quad \text{(C-2)}$$

Conditions when the reflection occurs relate to the reflector's dimensions and its geometry-relationship with the antenna. These parameters should be accurately measured before applying the model.

(2) Diffraction model

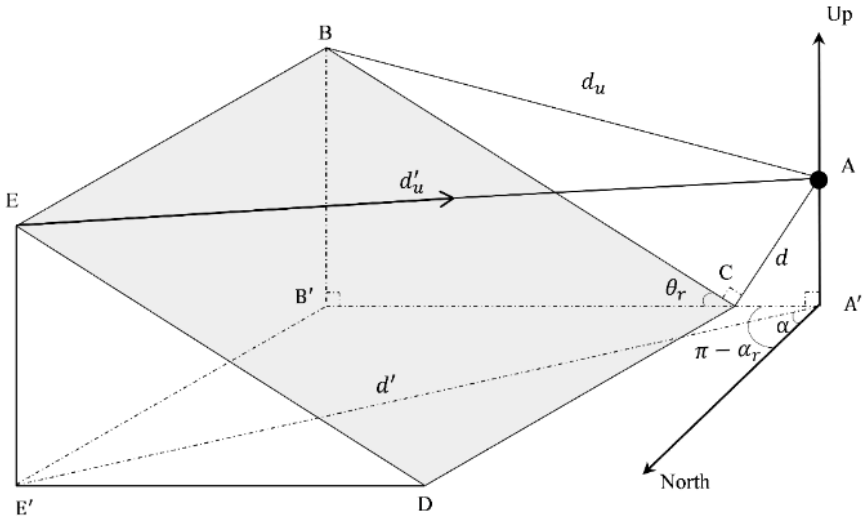

Figure 6-2 3D multipath diffraction model

Consider a blockage object surface BCDE, with slope angle θ_r and slope aspect α_r, since

$$\begin{cases} \text{CA}' = d/\sin(\theta_r) \\ \text{B}'\text{C} = \cos(\theta_r)\text{BC} = \cos(\theta_r)\sqrt{d_u^2 - d^2} \end{cases} \quad \text{(C-3)}$$

one can obtain

$$\text{B}'\text{A}' = \text{B}'\text{C} + \text{CA}' = \cos(\theta_r)\sqrt{d_u^2 - d^2} + \frac{d}{\sin(\theta_r)} \quad \text{(C-4)}$$

Denoting $\Delta\alpha = \angle\text{B}'\text{A}'\text{E}' = \pi - \alpha_r - \alpha$ and due to

$$\begin{cases} d' = \mathrm{E'A'} = \dfrac{\mathrm{B'A'}}{\cos(\Delta\alpha)} \\ d'_u = \mathrm{EA} = \sqrt{d_u^2 + (\mathrm{E'B'})^2}, \qquad \mathrm{E'B'} = \sin(\Delta\alpha) d' \end{cases} \tag{C-5}$$

we get

$$\begin{cases} d' = \dfrac{\cos(\theta_r)\sqrt{d_u^2 - d^2} + \dfrac{d}{\sin(\theta_r)}}{\cos(\Delta\alpha)} \\ d'_u = \sqrt{d_u^2 + (\sin(\Delta\alpha) d')^2} \end{cases} \tag{C-6}$$

Substituting d' and d'_u into Eq. (C-3) yields

$$\begin{cases} \Delta s_d = (1 - \cos(\theta'_d))\sqrt{d_u^2 + (\sin(\Delta\alpha) d')^2} \\ \theta'_d = \mathrm{atan}\left(\dfrac{\sqrt{d_u^2 - (\cos(\Delta\alpha) d')^2}}{d'}\right) - \theta \end{cases} \tag{C-7}$$

References

Al-Shaery A, Zhang S, Rizos C. (2013). An enhanced calibration method of GLONASS inter-channel bias for GNSS RTK. GPS Solutions, 17, 165-173. doi: 10.1007/s10291-012-0269-5.

Alves DBM. (2004). Using Cubic Splines to Mitigate Systematic Errors in GPS Relative Positioning. In: Proceedings of the 17th International Technical Meeting of the Satellite Division of The Institute of Navigation (ION GNSS 2004), Long Beach, CA, pp. 1374-1381.

Angus J. (2006). RAIM with multiple faults. Navigation, 53, 249-257. doi: 10.1002/j.2161-4296.2006.tb00387.x.

Banville S, Collins P, Lahaye F. (2018). Model comparison for GLONASS RTK with low-cost receivers. GPS Solutions, 22, 52. doi: 10.1007/s10291-018-0712-3.

Banville S, Langley R. (2013). Mitigating the impact of ionospheric cycle slips in GNSS observations. Journal of Geodesy, 87, 179-193. doi: 10.1007/s00190-012-0604-1.

Bartolomé J, Maufroid X, Hernández I, López Salcedo J, Granados G. (2015). Overview of Galileo System. In: Nurmi J, Lohan ES, Sand S, Hurskainen H (eds), GALILEO Positioning Technology. Springer Netherlands, pp. 9-33.

Berrocoso M, Prates G, Fernández-Ros A, García A. (2012). Normal vector analysis from GNSS—GPS data applied to Deception volcano surface deformation. Geophysical Journal International, 190, 1562-1570. doi: 10.1111/j.1365-246X.2012.05584.x.

Bisnath SB, Langley RB. (2002). High-precision platform positioning with a single GPS receiver. Navigation, 49, 161-169. doi: 10.1002/j.2161-4296.2002.tb00265.x.

Blewitt G. (1989). Carrier phase ambiguity resolution for the Global Positioning System applied to geodetic baselines up to 2000 km. Journal of Geophysical Research: Solid Earth, 94, 10187-10203. doi: 10.1029/JB094iB08p10187.

Blewitt G. (1990). An Automatic Editing Algorithm for GPS data. Geophysical Research Letters, 17, 199-202. doi: 10.1029/GL017i003p00199.

Bock Y, Agnew DC, Fang P, Genrich JF, Hager BH, Herring TA, Hudnut KW, King RW, Larsen S, Minster JB, Stark K, Wdowinski S, Wyatt FK. (1993). Detection of crustal deformation from the Landers earthquake sequence using continuous geodetic measurements. Nature, 361, 337. doi: 10.1038/361337a0.

Bock Y, Melgar D. (2016). Physical applications of GPS geodesy: a review. Reports on Progress in Physics, 79. doi: 10.1088/0034-4885/79/10/106801.

Brack A. (2017). Reliable GPS plus BDS RTK positioning with partial ambiguity resolution. GPS Solutions, 21, 1083-1092. doi: 10.1007/s10291-016-0594-1.

Cai C, Gao Y. (2013). Modeling and assessment of combined GPS/GLONASS precise point positioning. GPS Solutions, 17, 223-236. doi: 10.1007/s10291-012-0273-9.

Cai C, Pan L, Gao Y. (2014). A Precise Weighting Approach with Application to Combined L1/B1 GPS/BeiDou Positioning. The Journal of Navigation, 67, 911-925.

Chan WS, Xu YL, Ding XL, Dai WJ. (2006). An integrated GPS-accelerometer data processing technique for structural deformation monitoring. Journal of Geodesy, 80, 705-719. doi: 10.1007/s00190-006-0092-2.

Chen H, Jiang W, Ge M, Wickert J, Schuh H. (2014). An enhanced strategy for GNSS data processing of massive networks. Journal of Geodesy, 88, 857-867. doi: 10.1007/s00190-014-0727-7.

Chu FY, Yang M. (2014). GPS/Galileo long baseline computation: method and performance analyses. GPS Solutions, 18, 263-272. doi: 10.1007/s10291-013-0327-7.

Colosimo G, Crespi M, Mazzoni A. (2011). Real-time GPS seismology with a stand-alone receiver: A preliminary feasibility demonstration. Journal of Geophysical Research-Solid Earth, 116. doi: 10.1029/2010jb007941.

Crosta GB, di Prisco C, Frattini P, Frigerio G, Castellanza R, Agliardi F. (2014). Chasing a complete understanding of the triggering mechanisms of a large rapidly evolving rockslide. Landslides, 11, 747-764. doi: 10.1007/s10346-013-0433-1.

CSNO. (2019). BeiDou Navigation Satellite System Signal In Space Interface Control Document Open Service Signal B1I (Version 3.0).

Dach R, Lutz S, Walser P, Fridez P. (2015). Bernese GNSS Software Version 5.2. User manual. In. Astronomical Institute, Universtiy of Bern, Bern Open Publishing.

Dach R, Schaer S, Lutz S, Meindl M, Beutler G. (2010). Combining the observations from different GNSS. In: Proceedings of EUREF 2010 Symposium, Sweden.

Dai L, Wang J, Rizos C, Han S. (2002). Pseudo-Satellite Applications in Deformation Monitoring. GPS Solutions, 5, 80-87. doi: 10.1007/pl00012902.

Dai L, Wang J, Rizos C, Han S. (2003). Predicting atmospheric biases for real-time ambiguity resolution in GPS/GLONASS reference station networks. Journal of Geodesy, 76, 617-628. doi: 10.1007/s00190-002-0286-1.

Dai W, Shi Q, Cai C. (2017). Characteristics of the BDS Carrier Phase Multipath and Its Mitigation Methods in Relative Positioning. Sensors, 17, 796. doi: 10.3390/s17040796.

Dai WJ, Huang DW, Cai CS. (2014). Multipath mitigation via component analysis methods for GPS dynamic deformation monitoring. GPS Solutions, 18, 417-428. doi: 10.1007/s10291-013-0341-9.

Ding S, Shi J, Jiang W. (2015). Theory and method of hypothetical test for nonparameters in linear semiparametric model. Survey Review. doi: 10.1179/1752270614Y.0000000147.

Ding W. (2007). Integration of MEMS INS with GPS carrier phase derived velocity: A new approach. In: Proceedings of the 20th International Technical Meeting of the Satellite Division of The Institute of Navigation (ION GNSS 2007), Fort Worth, TX pp. 2085-2093.

Ding W, Wang J. (2011). Precise velocity estimation with a stand-alone GPS receiver. Journal of Navigation, 64, 311-325. doi: 10.1017/S0373463310000482.

Ding X, Coleman R. (1996). Multiple outlier detection by evaluating redundancy contributions of observations. Journal of Geodesy, 70, 489-498. doi: 10.1007/bf00863621.

Dolgansky A. (2010). Multi-GNSS Simulations for Satellite Point Positioning. YORK UNIVERSITY.

Dong D, Wang M, Chen W, Zeng Z, Song L, Zhang Q, Cai M, Cheng Y, Lv J. (2016). Mitigation of multipath effect in GNSS short baseline positioning by the multipath hemispherical map. Journal of Geodesy, 90, 255-262. doi: 10.1007/s00190-015-0870-9.

Dow J, Neilan RE, Rizos C. (2009). The International GNSS Service in a changing landscape of Global Navigation Satellite Systems. Journal of Geodesy, 83, 191-198. doi: 10.1007/s00190-008-0300-3.

Durmaz M, Karslioglu M. (2015). Regional vertical total electron content (VTEC) modeling together with satellite and receiver differential code biases (DCBs)

using semi-parametric multivariate adaptive regression B-splines (SP-BMARS). Journal of Geodesy, 89, 347-360. doi: 10.1007/s00190-014-0779-8.

El-Mowafy A. (2014). GNSS multi-frequency receiver single-satellite measurement validation method. GPS Solutions, 18, 553-561. doi: 10.1007/s10291-013-0352-6.

EU. (2016). Galileo open service, signal in space interface control document (OS SIS ICD). In: ICD-Galileo. European space agency/European GNSS supervisory authority.

Euler HJ, Schaffrin B. (1991). On a Measure for the Discernibility between Different Ambiguity Solutions in the Static-Kinematic Gps-Mode. Kinematic Systems in Geodesy, Surveying, and Remote Sensing, 107, 285-295.

Evans D, Jones AJ. (2008). Non-parametric estimation of residual moments and covariance. Proceedings of the Royal Society of London A: Mathematical, Physical and Engineering Sciences, 464, 2831-2846.

Fessler JA. (1991). Nonparametric fixed-interval smoothing with vector splines. IEEE Transactions on Signal Processing, 39, 852-859. doi: 10.1109/78.80907.

Fischer B, Hegland M. (1999). Collocation, filtering and nonparametric regression, Part I. ZfV, 124, 17-24.

Ford TJ, Hamilton J. (2003). A new positioning filter: Phase smoothing in the position domain. Navigation, 50, 65-78. doi: 10.1002/j.2161-4296.2003.tb00319.x.

Freda P, Angrisano A, Gaglione S, Troisi S. (2015). Time-differenced carrier phases technique for precise GNSS velocity estimation. GPS Solutions, 19, 335-341. doi: 10.1007/s10291-014-0425-1.

Ge M, Gendt G, Dick G, Zhang F, Rothacher M. (2006). A new data processing strategy for huge GNSS global networks. Journal of Geodesy, 80, 199-203. doi: 10.1007/s00190-006-0044-x.

Ge M, Gendt G, Rothacher M, Shi C, Liu J. (2008). Resolution of GPS carrier-phase ambiguities in Precise Point Positioning (PPP) with daily observations. Journal of Geodesy, 82, 389-399. doi: 10.1007/s00190-007-0187-4.

Geng T, Xie X, Fang RX, Su X, Zhao QL, Liu G, Li H, Shi C, Liu JN. (2016). Real-time capture of seismic waves using high-rate multi-GNSS observations: Application to the 2015 M(w)7.8 Nepal earthquake. Geophysical Research Letters, 43, 161-167. doi: 10.1002/2015gl067044.

Golub GH, Heath M, Wahba G. (1979). Generalized Cross-Validation as a method for choosing a good ridge parameter. Technometrics, 21, 215-223. doi: 10.1080/00401706.1979.10489751.

Gong X, Gu S, Lou Y, Zheng F, Ge M, Liu J. (2018). An efficient solution of real-time data processing for multi-GNSS network. Journal of Geodesy, 92, 797-809. doi: 10.1007/s00190-017-1095-x.

GPS Directorate. (2013). Navstar GPS Space Segment/Navigation User Interfaces. In: ICD-GPS, IS-GPS-200H edn.

Green PJ, Silverman BW. (1994). Nonparametric regression and generalized linear models: a roughness penalty approach. Chapman & Hall London.

Gurtner W, Estey L. (2013). RINEX: the receiver independent exchange format. 3.03 edn.

Håkansson M, Jensen ABO, Horemuz M, Hedling G. (2016). Review of code and phase biases in multi-GNSS positioning. GPS Solutions, 1-12. doi: 10.1007/s10291-016-0572-7.

Han S, Dai L, Rizos C. (1999). A new data processing strategy for combined GPS/GLONASS carrier phase-based positioning. In: Proceedings of the 12th International Technical Meeting of the Satellite Division of The Institute of Navigation (ION GPS 1999), pp. 1619-1627.

Han S, Rizos C. (2000). GPS multipath mitigation using fir filters. Survey Review, 35, 487-498.

Han SL, Wang JL. (2012). Integrated GPS/INS navigation system with dual-rate Kalman Filter. GPS Solutions, 16, 389-404. doi: 10.1007/s10291-011-0240-x.

Hannah BM. (2001). Modelling and simulation of GPS multipath propagation. Queensland University of Technology.

Hansen PC. (1992). Analysis of discrete ill-posed problems by means of the L-curve. SIAM Review, 34, 561-580. doi: 10.1137/1034115.

Hewitson S, Wang J. (2006). GNSS receiver autonomous integrity monitoring (RAIM) performance analysis. GPS Solutions, 10, 155-170. doi: 10.1007/s10291-005-0016-2.

Hilla S. (2010). The Extended Standard Product 3 Orbit Format (SP3-c). https://igscb.jpl.nasa.gov/igscb/data/format/sp3c.txt. Accessed Dec. 10, 2015.

Hofmann-Wellenhof B, Lichtenegger H, Wasle E. (2008). GNSS: Global Navigation Satellite Systems: GPS, GLONASS, Galileo, and More. Springer, Vienna.

Hoque MM, Jakowski N. (2007). Higher order ionospheric effects in precise GNSS positioning. Journal of Geodesy, 81, 259-268. doi: 10.1007/s00190-006-0106-0.

Hu H. (2005). Ridge estimation of a semiparametric regression model. Journal of Computational and Applied Mathematics, 176, 215-222. doi: 10.1016/j.cam.2004.07.032.

Hu X, Lu Z, Pierson TC, Kramer R, George DL. (2018). Combining InSAR and GPS to Determine Transient Movement and Thickness of a Seasonally Active Low-Gradient Translational Landslide. Geophysical Research Letters, 45, 1453-1462. doi: 10.1002/2017GL076623.

Im SB, Hurlebaus S, Kang YJ. (2013). Summary Review of GPS Technology for Structural Health Monitoring. Journal of Structural Engineering, 139, 1653-1664. doi: 10.1061/(ASCE)ST.1943-541X.0000475.

Jia M. (2000). Mitigation of systematic errors of GPS positioning using vector semiparametric models. In: Proceedings of the 13th International Technical Meeting of the Satellite Division of The Institute of Navigation (ION GPS 2000), Salt Lake City, USA, pp. 1938-1947.

Jia M, Stewart M, Tsakiri M, Australia PWA. (2001). Mitigation of ionospheric errors by penalised least squares technique for high precision medium distance GPS positioning. In: Proceedings of International Symposium on Kinematic Systems in Geodesy, Geomatics and Navigation, Banff, Alberta, Canada.

Jia MH, Stewart M, Tsakiri M. (2002). A statistical test procedure for the detection and identification of GPS systematic errors. Vistas for Geodesy in the New Millennium, 125, 404-409.

Kaplan ED, Hegarty CJ. (2017). Understanding GPS/GNSS: Principles and Applications. Artech House, USA.

Kelso T. (2015). CelesTrack. www.celestrak.com/NORAD/elements/. Accessed May 16, 2017.

Kjørsvik N, Gjevestad J, Øvstedal O. (2006). Handling of the tropospheric delay in kinematic Precise Point Positioning. In: Proceedings of the 19th International Technical Meeting of the Satellite Division of the Institute of Navigation (Ion Gnss 2006), Fort Worth, TX pp. 2279-2281

Knight NL, Wang J, Rizos C. (2010). Generalised measures of reliability for multiple outliers. Journal of Geodesy, 84, 625-635. doi: 10.1007/s00190-010-0392-4.

Koch K-R. (2015). Minimal detectable outliers as measures of reliability. Journal of Geodesy, 89, 483-490. doi: 10.1007/s00190-015-0793-5.

Koch KR, Kusche J. (2002). Regularization of geopotential determination from satellite data by variance components. Journal of Geodesy, 76, 259-268. doi: 10.1007/s00190-002-0245-x.

Komac M, Holley R, Mahapatra P, van der Marel H, Bavec M. (2015). Coupling of GPS/GNSS and radar interferometric data for a 3D surface displacement monitoring of landslides. Landslides, 12, 241-257. doi: 10.1007/s10346-014-0482-0.

Kotsakis C. (2005). On the trade-off between model expansion, model shrinking, and parameter estimation accuracy in least-squares data analysis. Journal of Geodesy, 79, 460-466. doi: 10.1007/s00190-005-0479-5.

Kouba J. (2015). A guide to using International GNSS Service (IGS) products. http://kb.igs.org/hc/en-us/article_attachments/203088448/UsingIGSProductsVer21_cor.pdf. Accessed Dec. 01, 2016.

Kubo N, Tokura H, Pullen S. (2017). Mixed GPS-BeiDou RTK with inter-systems bias estimation aided by CSAC. GPS Solutions, 22. doi: 10.1007/s10291-017-0670-1.

Kusche J, Klees R. (2002). Regularization of gravity field estimation from satellite gravity gradients. Journal of Geodesy, 76, 359-368. doi: 10.1007/s00190-002-0257-6.

Lau L, Cross P. (2007). Development and testing of a new ray-tracing approach to GNSS carrier-phase multipath modelling. Journal of Geodesy, 81, 713-732. doi: 10.1007/s00190-007-0139-z.

Leandro RF, Langley RB, Santos MC. (2008). UNB3m_pack: a neutral atmosphere delay package for radiometric space techniques. GPS Solutions, 12, 65-70. doi: 10.1007/s10291-007-0077-5.

Leick A, Rapoport L, Tatarnikov D. (2015). GPS satellite surveying. John Wiley & Sons, Inc, Hoboken, NJ, USA.

Li BF, Shen YZ, Feng YM. (2010). Fast GNSS ambiguity resolution as an ill-posed problem. Journal of Geodesy, 84, 683-698. doi: 10.1007/s00190-010-0403-5.

Li G, Wu J, Zhao C, Tian Y. (2017). Double differencing within GNSS constellations. GPS Solutions, 21, 1161-1177. doi: 10.1007/s10291-017-0599-4.

Li P, Zhang X. (2014). Integrating GPS and GLONASS to accelerate convergence and initialization times of precise point positioning. GPS Solutions, 18, 461-471. doi: 10.1007/s10291-013-0345-5.

Li X, Ge M, Dai X, Ren X, Fritsche M, Wickert J, Schuh H. (2015a). Accuracy and reliability of multi-GNSS real-time precise positioning: GPS, GLONASS, BeiDou, and Galileo. Journal of Geodesy, 89, 607-635. doi: 10.1007/s00190-015-0802-8.

Li X, Ge M, Guo B, Wickert J, Schuh H. (2013). Temporal point positioning approach for real-time GNSS seismology using a single receiver. Geophysical Research Letters, 40, 5677-5682. doi: 10.1002/2013GL057818, 2013.

Li X, Zhang X, Ren X, Fritsche M, Wickert J, Schuh H. (2015b). Precise positioning with current multi-constellation Global Navigation Satellite Systems: GPS, GLONASS, Galileo and BeiDou. Scientific reports, 5, 8328. doi: 10.1038/srep08328.

Lou Y, Liu Y, Shi C, Yao X, Zheng F. (2014). Precise orbit determination of BeiDou constellation based on BETS and MGEX network. Scientific reports, 4. doi: 10.1038/srep04692.

Lou Y, Zheng F, Gu S, Wang C, Guo H, Feng Y. (2015). Multi-GNSS precise point positioning with raw single-frequency and dual-frequency measurement models. GPS Solutions, 1-14. doi: 10.1007/s10291-015-0495-8.

Meng X. (2002). Real-time deformation monitoring of bridges using GPS/Accelerometers. PhD.

Meng X, Roberts GW, Dodson AH, Cosser E, Barnes J, Rizos C. (2004). Impact of GPS satellite and pseudolite geometry on structural deformation monitoring: analytical and empirical studies. Journal of Geodesy, 77, 809-822. doi: 10.1007/s00190-003-0357-y.

Menke W. (2015). Review of the Generalized Least Squares Method. Surveys in Geophysics, 36, 1-25. doi: 10.1007/s10712-014-9303-1.

Moafipoor S, Grejner-Brzezinska D, Toth C. (2004). Tightly coupled GPS/INS integration based on GPS carrier phase velocity update. In: Proceedings of the 17th International Technical Meeting of the Satellite Division of The Institute of Navigation (ION GNSS 2004), Long Beach, CA pp. 1094-1102

Montenbruck O, Steigenberger P, Khachikyan R, Weber G, Langley R, Mervart L, Hugentobler U. (2013). IGS-MGEX: preparing the ground for multi-constellation GNSS science. In: 4th international colloquium scientific and fundamental aspects of the Galileo programme, ESA.

Motagh M, Djamour Y, Walter TR, Wetzel H-U, Zschau J, Arabi S. (2007). Land subsidence in Mashhad Valley, northeast Iran: Results from InSAR, levelling and GPS. Geophysical Journal International, 168, 518-526. doi: 10.1111/j.1365-246X.2006.03246.x.

Nadarajah N, Teunissen PJG, Raziq N. (2013). BeiDou inter-satellite-type bias evaluation and calibration for mixed receiver attitude determination. Sensors (Basel, Switzerland), 13, 9435-9463. doi: 10.3390/s130709435.

Odolinski R, Teunissen PJG, Odijk D. (2015). Combined BDS, Galileo, QZSS and GPS single-frequency RTK. GPS Solutions, 19, 151-163. doi: 10.1007/s10291-014-0376-6.

Olynik M, Petovello MG, Cannon ME, Lachapelle G. (2002). Temporal Variability of GPS Error Sources and Their Effect on Relative Positioning Accuracy. In: Proceedings of the 2002 National Technical Meeting of The Institute of Navigation, San Diego, CA, pp. 877-888.

Parkinson BW, Spilker J. (1996). Global Positioning System: Theory and Applications (Volumn I). American Institute of Aeronautics, Inc., Washington, DC.

Paziewski J, Wielgosz P. (2015). Accounting for Galileo–GPS inter-system biases in precise satellite positioning. Journal of Geodesy, 89, 81-93. doi: 10.1007/s00190-014-0763-3.

Pozo-Pérez JA, Medina D, Herrera-Pinzón I, Heßelbarth A, Ziebold R. (2017). Robust Outlier Mitigation in Multi-Constellation GNSS Positioning for Waterborne Applications. In: Proceedings of the International Technical Meeting of The Institute of Navigation (ITM 2017). ION Publications, pp. 1330-1343.

Pratt M, Burke B, Misra P. (1998). Single-epoch integer ambiguity resolution with GPS-GLONASS L1-L2 Data. In: PROCEEDINGS OF ION GPS. INSTITUTE OF NAVIGATION, pp. 389-398.

Press WH, Teukolsky SA, Vetterling WT, Flannery BP. (2007). Numerical recipes 3rd edition: The art of scientific computing. Cambridge university press.

Revnivykh S. (2012). GLONASS status and modernization. In: International Committee on GNSS (ICG-7), Beijing, China.

RISDE. (2008). GLONASS Interface Control Document. In: ICD-GLONASS, 5.1 edn, Moscow.

Rizos C. (2008). Multi - constellation GNSS/RNSS from the perspective of high accuracy users in Australia. Journal of Spatial Science, 53, 29-63.

Satirapod C, Wang J, Rizos C. (2003). Comparing different GPS data processing techniques for modelling residual systematic errors. Journal of Surveying Engineering, 129, 129-135.

Schüler T. (2006). Impact of systematic errors on precise long-baseline kinematic GPS positioning. GPS Solutions, 10, 108-125. doi: 10.1007/s10291-005-0012-6.

Serrano L, Kim D, Langley RB. (2004a). A single GPS receiver as a real-time, accurate velocity and acceleration sensor. In: Proceedings of the 17th International Technical Meeting of the Satellite Division of The Institute of Navigation (ION GNSS 2004), Long Beach, CA pp. 2021-2034

Serrano L, Kim D, Langley RB, Itani K, Ueno M. (2004b). A GPS velocity sensor: how accurate can it be?–a first look. In: Proceedings of the 17th International Technical Meeting of the Satellite Division of The Institute of Navigation (ION GNSS 2004), Long Beach, CA pp. 875-885.

Shi C, Zhao Q, Hu Z, Liu J. (2013). Precise relative positioning using real tracking data from COMPASS GEO and IGSO satellites. GPS Solutions, 17, 103-119. doi: 10.1007/s10291-012-0264-x.

Shu Y, Shi Y, Xu P, Niu X, Liu J. (2017). Error analysis of high-rate GNSS precise point positioning for seismic wave measurement. Advances in Space Research, 59, 2691-2713. doi: 10.1016/j.asr.2017.02.006.

Soon BKH, Scheding S, Lee HK, Lee HK, Durrant-Whyte H. (2008). An approach to aid INS using time-differenced GPS carrier phase (TDCP) measurements. GPS Solutions, 12, 261-271. doi: 10.1007/s10291-007-0083-7.

Takasu T. (2012). RTKLIB: An Open Source Program Package for GNSS Positioning. http://www.rtklib.com/prog/rtklib_2.4.1.zip. Accessed Jun. 20, 2015.

Teng Y, Wang J. (2016). A closed-form formula to calculate geometric dilution of precision (GDOP) for multi-GNSS constellations. GPS Solutions, 20, 331-339. doi: 10.1007/s10291-015-0440-x.

Teunissen PJG. (1995). The least-squares ambiguity decorrelation adjustment: a method for fast GPS integer ambiguity estimation. Journal of Geodesy, 70, 65-82. doi: 10.1007/BF00863419.

Teunissen PJG. (1998). Quality Control and GPS. In: Teunissen PG, Kleusberg A (eds), GPS for Geodesy. Springer Berlin Heidelberg, pp. 271-318.

Teunissen PJG, Amiri-Simkooei AR. (2008). Least-squares variance component estimation. Journal of Geodesy, 82, 65-82. doi: 10.1007/s00190-007-0157-x.

Teunissen PJG, Joosten P, Tiberius C. (1999). Geometry-free ambiguity success rates in case of partial fixing. In: Proceedings of the 1999 National Technical Meeting of The Institute of Navigation, San Diego, CA, pp. 201-207

Teunissen PJG, Khodabandeh A. (2015). Review and principles of PPP-RTK methods. Journal of Geodesy, 89, 217-240. doi: 10.1007/s00190-014-0771-3.

Teunissen PJG, Odolinski R, Odijk D. (2014a). Instantaneous BeiDou plus GPS RTK positioning with high cut-off elevation angles. Journal of Geodesy, 88, 335-350. doi: 10.1007/s00190-013-0686-4.

Teunissen PJG, Odolinski R, Odijk D. (2014b). Instantaneous BeiDou+GPS RTK positioning with high cut-off elevation angles. Journal of Geodesy, 88, 335-350. doi: 10.1007/s00190-013-0686-4.

Tian Y, Ge M, Neitzel F. (2015). Particle filter-based estimation of inter-frequency phase bias for real-time GLONASS integer ambiguity resolution. Journal of Geodesy, 1-14. doi: 10.1007/s00190-015-0841-1.

Tian Y, Liu Z, Ge M, Neitzel F. (2019). Multi-dimensional particle filter-based estimation of inter-system phase biases for multi-GNSS real-time integer ambiguity resolution. Journal of Geodesy. doi: 10.1007/s00190-018-01226-6.

Traugott J, Odijk D, Montenbruck O, Sachs G, Tiberius C. (2008). Making a Difference with GPS. GPS world, 19, 48-57.

Tu R, Wang R, Ge M, Walter TR, Ramatschi M, Milkereit C, Bindi D, Dahm T. (2013). Cost-effective monitoring of ground motion related to earthquakes, landslides, or volcanic activity by joint use of a single-frequency GPS and a MEMS accelerometer. Geophysical Research Letters, 40, 3825-3829. doi: 10.1002/grl.50653.

Vallado D, Crawford P, Hujsak R, Kelso TS. (2006). Revisiting Spacetrack Report #3. In: AIAA/AAS Astrodynamics Specialist Conference and Exhibit. American Institute of Aeronautics and Astronautics.

Van Graas F, Soloviev A. (2004). Precise Velocity Estimation Using a Stand-Alone GPS Receiver. Navigation, 51, 283-292. doi: 10.1002/j.2161-4296.2004.tb00359.x.

Vieweg S, Lechner W. (1994). Realizing GNSS-results of combined GPS/GLONASS data processing. In: Position Location and Navigation Symposium. IEEE, Las Vegas, NV pp. 762-768.

Wang J. (2000). An approach to GLONASS ambiguity resolution. Journal of Geodesy, 74, 421-430. doi: 10.1007/s001900000096.

Wang J, Rizos C, Stewart MP, Leick A. (2001). GPS and GLONASS integration: Modeling and ambiguity resolution issues. GPS Solutions, 5, 55-64. doi: 10.1007/PL00012877.

Wang NB, Yuan YB, Li ZS, Montenbruck O, Tan BF. (2016). Determination of differential code biases with multi-GNSS observations. Journal of Geodesy, 90, 209-228. doi: 10.1007/s00190-015-0867-4.

Wanninger L. (2012). Carrier-phase inter-frequency biases of GLONASS receivers. Journal of Geodesy, 86, 139-148. doi: 10.1007/s00190-011-0502-y.

Weber R, Springer TA. (2001). The international GLONASS experiment: products, progress and prospects. Journal of Geodesy, 75, 559-568. doi: 10.1007/s001900100199.

Wendel J, Meister O, Monikes R, Trommer GF. (2006). Time-Differenced Carrier Phase Measurements for Tightly Coupled GPS/INS Integration. In: Proceedings of IEEE/ION PLANS 2006, San Diego, CA, pp. 54-60.

Xu P. (1991). Least squares collocation with incorrect prior information. ZfV, 116, 266-273.

Xu P. (1992). Determination of surface gravity anomalies using gradiometric observables. Geophysical Journal International, 110, 321-332. doi: 10.1111/j.1365-246X.1992.tb00877.x.

Xu P. (1998). Truncated SVD methods for discrete linear ill-posed problems. Geophysical Journal International, 135, 505-514. doi: 10.1046/j.1365-246X.1998.00652.x.

Xu P, Rummel R. (1994). Generalized ridge regression with applications in determination of potential fields. Manuscripta geodaetica, 20, 8-8.

Xu P, Shen Y, Fukuda Y, Liu Y. (2006). Variance Component Estimation in Linear Inverse Ill-posed Models. Journal of Geodesy, 80, 69-81. doi: 10.1007/s00190-006-0032-1.

Yang L, Li B, Li H, Rizos C, Shen Y. (2017). The influence of improper stochastic modeling of Beidou pseudoranges on system reliability. Advances in Space Research, 60, 2680-2690. doi: 10.1016/j.asr.2017.05.035.

Yang L, Wang J, Knight NL, Shen Y. (2013). Outlier separability analysis with a multiple alternative hypotheses test. Journal of Geodesy, 87, 591-604. doi: 10.1007/s00190-013-0629-0.

Yang Y, Li J, Xu J, Tang J, Guo H, He H. (2011). Contribution of the Compass satellite navigation system to global PNT users. Chinese Science Bulletin, 56, 2813-2819. doi: 10.1007/s11434-011-4627-4.

Yang Y, Song L, Xu T. (2002). Robust estimator for correlated observations based on bifactor equivalent weights. Journal of Geodesy, 76, 353-358. doi: 10.1007/s00190-002-0256-7.

Ye S, Chen D, Liu Y, Jiang P, Tang W, Xia P. (2015). Carrier phase multipath mitigation for BeiDou navigation satellite system. GPS Solutions, 19, 545-557. doi: 10.1007/s10291-014-0409-1.

Yi T-H, Li H-N, Gu M. (2013). Recent research and applications of GPS-based monitoring technology for high-rise structures. Structural Control and Health Monitoring, 20, 649-670. doi: 10.1002/stc.1501.

Yin Y, Zheng W, Liu Y, Zhang J, Li X. (2010). Integration of GPS with InSAR to monitoring of the Jiaju landslide in Sichuan, China. Landslides, 7, 359-365. doi: 10.1007/s10346-010-0225-9.

Yu W, Ding X, Dai W, Chen W. (2017). Systematic error mitigation in multi-GNSS positioning based on semiparametric estimation. Journal of Geodesy, 91, 1491-1502. doi: 10.1007/s00190-017-1038-6.

Zar JH. (2010). Biostatistical Analysis. Pearson Prentice-Hall, Upper Saddle River, NJ.

Zarraoa N, Mai W, Sardon E, Jungstand A. (1998). Preliminary evaluation of the Russian GLONASS system as a potential geodetic tool. Journal of Geodesy, 72, 356-363. doi: 10.1007/s001900050175.

Zhao Y. (2016). Applying Time-Differenced Carrier Phase in Non-Differential GPS/IMU Tightly-Coupled Navigation Systems to Improve the Positioning Performance. Ieee Transactions on Vehicular Technology, 66, 992-1003. doi: 10.1109/TVT.2016.2558206.

Zheng DW, Zhong P, Ding XL, Chen W. (2005). Filtering GPS time-series using a Vondrak filter and cross-validation. Journal of Geodesy, 79, 363-369. doi: 10.1007/s00190-005-0474-x.

Zhong P, Ding XL, Yuan LG, Xu YL, Kwok K, Chen YQ. (2010). Sidereal filtering based on single differences for mitigating GPS multipath effects on short baselines. Journal of Geodesy, 84, 145-158. doi: 10.1007/s00190-009-0352-z.

Zumberge JF, Heflin MB, Jefferson DC, Watkins MM, Webb FH. (1997). Precise point positioning for the efficient and robust analysis of GPS data from large networks. Journal of Geophysical Research-Solid Earth, 102, 5005-5017. doi: 10.1029/96jb03860.